Absorption of Ammonia–Water and CO_2–NH_3–H_2O Mixture in Mini-Channel Heat Exchangers

Liang Shi

Technische Universiteit Delft

TU Delft Delft University of Technology

Challenge the future

Absorption of Ammonia–Water and CO_2–NH_3–H_2O Mixture in Mini-Channel Heat Exchangers

by

Liang Shi

in partial fulfillment of the requirements for the degree of

Master of Science
in Mechanical Engineering

at the Delft University of Technology,
to be defended publicly on Friday January 27, 2017 at 09:30 AM.

Supervisor:	Dr. ir. C.A. Infante Ferreira
	Ir. V. Gudjonsdottir
Thesis committee:	Prof. Dr. ir. T.J.H. Vlugt
	Dr. ir. R. Pecnik
	Dr. W. Haije

TU Delft Delft University of Technology

SUMMARY

The energy consumption in the industry field is considerable. Saving energy has great potential in many industrial processes. For example, heat recovery from the spent cooling water can be achieved by applying heat pump technology, and the recovered heat can be used for district heating. Previous study indicates that the compression-resorption cycle has higher efficiency than traditional vapor-compression heat pumps due to the fact that it can take advantage of the temperature glide of the multi-component working fluid. The absorption process within the resorber and its performance should be further investigated. Ammonia–water mixture is commonly used as the working fluid in the compression-resorption heat pump. Recently the CO_2–NH_3–H_2O mixture has been identified as a promising working fluid theoretically, relevant experiment should be conducted to verify it.

For the theoretical background, previous studies about kinetics of CO_2 absorption in ammonia–water have been reviewed. Currently most of the theoretical and experimental studies are performed for post combustion capture usage. The working conditions deviate much from that for the compression-resorption heat pump cycle; therefore existent kinetic models are not suitable for predicting the absorption rate of the CO_2 in ammonia–water within a compression-resorption heat pump cycle. Previous studies from TU Delft indicate that a more accurate model should be developed to predict the absorption process of the ammonia–water mixture in a multi-tube mini-channel heat exchanger.

In this study a steady-state theoretical model has been developed to predict the absorption process of ammonia–water mixture in a multi-tube mini-channel heat exchanger by assuming Nusselt falling film theory and annular flow pattern. The model is extended to cover all three different phases (superheated vapor, 2-phase, and sub-cooled liquid) of the ammonia–water mixture.

Experiments with two different working fluids (ammonia–water mixture and CO_2–NH_3–H_2O mixture) on the tube side and cooling water on the shell side have been performed respectively. Results indicate that adding a small amount of CO_2 (2.1 wt%) directly will lead to slightly better heat exchange on the water side when operated in optimum condition. But the operating status becomes much less stable than the experiment with ammonia–water as a working fluid. The pump becomes difficult to operate with constant mass flow. While when the flow directions on both sides are changed, more stable operating conditions can be achieved. This indicates the configuration of the heat exchanger and the flow direction influence the operating stability. Also it is possible to have CO_2 desorbed at the pump even in low temperature. Therefore to put into practical use, more tests should be done to comprehensively investigate the feasibility of applying CO_2–NH_3–H_2O mixture as working fluid in a compression-resorption heat pump.

The theoretical model has been validated by the experimental data. For the 2-phase flow condition on the tube side, the simulation results indicate that the assumption of annular flow pattern is reasonable for most of the heat exchange area. But when the vapor quality is low, the film thickness prediction based on the Nusselt falling film theory is not reasonable any longer, this indicates a transition of a flow pattern. A new flow pattern occurs in order to enhance the transport phenomena. The validation results show that the extended model can accurately predict the heat load and the temperature profile along the absorption process. However the pressure drop cannot be rea-

sonably predicted. This can be caused by inaccurate friction factor estimation or ignorance of other effects which can cause extra pressure drop. The heat transfer performance at the superheated region is studied in detail. Results show an obscure relation between the weakened heat transfer phenomenon and the hydrodynamic instabilities on the tube side. Experimental data are also applied to validate the thermodynamic equilibrium models for the CO_2–NH_3–H_2O mixture.

The model developed in this project can be used to predict the heat transfer performance for certain type of heat exchangers conducting ammonia–water absorption process, or be modified to apply for other conditions. The experimental data are useful for ammonia–water and CO_2–NH_3–H_2O mixture absorption related studies. As a follow-up for this research it is of interest to further investigate and identify the flow pattern transition when the vapor quality is low, and develop a more comprehensive model to predict the absorption process. Visual observations will help to understand the flow pattern transitions. A complete compression-resorption heat pump setup will contribute to more useful experimental result to estimate the performance using CO_2–NH_3–H_2O mixture as a working fluid.

ACKNOWLEDGEMENTS

First of all I would like to thank my supervisors Dr. ir. C.A. Infante Ferreira and Ir. V. Gudjonsdottir for their excellent supervision and kind help. Carlos, thank you so much for always being warmhearted and patient. It's been great pleasure to be under your supervision since internship. The schedules were always well organized and I can always get illuminated from your explanations and suggestions. Vilborg, thank you for your help and attention. You were always willing to help me when I came across difficulties no matter in modeling or experiments, and your enthusiastic personality really inspired me a lot.

Furthermore I would like to thank Prof. Dr. ir. T.J.H. Vlugt, Dr. ir. R. Pecnik, and Dr. W. Haije for joining the exam committee and putting effort to evaluate my thesis project.

I would also like to show my gratitude to my parents, who always respect my decisions and support me unconditionally, and my girlfriend Di who always gives me comfort and strength. Many thanks to my friends, it's great to have your accompanies and I really appreciated it.

Liang Shi
Delft, January 2017

NOMENCLATURE

A	area	[m^2]
B	base	[–]
c	molar concentration	[mol m^{-3}]
c_p	heat capacity	[J kg^{-1} K^{-1}]
D	diffusivity	[m^2 s^{-1}]
d	diameter	[m]
E	overall heat transfer coefficient	[W m^{-2} K^{-1}]
E_a	activation energy	[J mol^{-1}]
F	mass transfer coefficient	[mol m^{-2} s^{-1}]
F_{Nu}	Nusselt number factor	[–]
f	friction factor	[–]
G	mass flux	[kg m^{-2} s^{-1}]
g	gravity constant	[m s^{-2}]
h	enthalpy	[J kg^{-1}]
h_c	convective heat transfer coefficient	[W m^{-2} K^{-1}]
$\hat{h}$	partial enthalpy	[J kg^{-1}]
J	molar flux	[mol m^{-2} s^{-1}]
k	reaction rate constant	[–]
k_c	convective mass transfer coefficient	[m s^{-1}]
L	characteristic length	[m]
l	length	[m]
M	molar mass	[kg mol^{-1}]
$\dot{m}$	mass flow	[kg s^{-1}]
P	pressure	[Pa]
$\dot{Q}$	heat flow	[W]
q	quality	[–]
R	universal gas constant	[J K^{-1} mol^{-1}]
r	reaction rate	[mol L^{-1} s^{-1}]
r	span ratio	[–]
T	temperature	[K]
U	uncertainty	[–]
u	velocity	[m s^{-1}]
w	mass concentration	[–]
x	molar concentration	[–]
y	local position	[m]
z	ratio of ammonia to the total molar flux	[–]

GREEK SYMBOL

α	thermal diffusivity	[m^2 s^{-1}]
γ	proportion factor	[–]
δ	film thickness	[m]
ζ	drag coefficient	[–]
λ	thermal conductivity	[W m^{-1} K^{-1}]

μ	dynamic viscosity	[Pa s]
ν	kinematic viscosity	[$m^2\ s^{-1}$]
ξ	friction factor	[–]
ρ	density	[$kg\ m^{-3}$]
Φ	heat flow	[W]
ϕ	heat flux	[$W\ m^{-2}$]

SUBSCRIPT

app	apparent property
B	base
$cali$	calibrated
cw	cooling water
h	hydraulic
i	interface, internal
in	inlet
l	liquid phase
lam	laminar
lm	logarithm mean
$meas$	measured
obs	observed property
opt	optimum condition
out	outlet
s	shell side
sat	saturation property
t	tube side
ti	inner tube
to	outer tube
tp	two-phase
$turb$	turbulent
v	vapor phase
w	tube wall

SUPERSCRIPT

T	termolecular mechanism
Z	zwitter-ion mechanism

ABBREVIATION

COP	coefficient of performance
CRHP	compression resorption heat pump
e-NRTL	electrolyte non-random two-liquid
LMTD	logarithm mean temperature difference
PCC	post combustion capture
SCR	stirred cell reactor
SDC	string of discs contactor
TS	temperature sensor
UNIQUAC	universal quasi-chemical
VCHP	vapor compression heat pump
WWC	wetted-wall column

DIMENSIONLESS NUMBER	
Nu	Nusselt number
Pr	Prandtl number
Re	Reynolds number
Sc	Schmidt number
Sh	Sherwood number

CONTENTS

1

INTRODUCTION

1.1. ENERGY USAGE IN THE INDUSTRY FIELD

Due to industrial development and population growth, there is a huge increase in global demand of energy. During 1971 to 2013, the world total final energy consumption rose from 4667 to 9301 Mtoe [1]. Among all kinds of energy resources, conventional fossil energy (coal, oil and natural gas) took up more than 65 percent. Over reliance of these non-renewable energy resources will eventually cause an energy crisis. One way to prevent this problem from happening is to develop new technologies to utilize energy with higher efficiency.

Industry contributes to a great part of the total energy consumption. In 2013, the final energy consumption of the industry was 2702.44 Mtoe worldwide, which was 29% of the total final consumption [1]. This ratio is similar to that of the Netherlands. In 2014, 30% of the total final energy consumption originated from the industry field in the Netherlands [2]. This large share of energy consumption by industry indicates that developing technologies to increase the total efficiency of industrial processes has a great potential to save energy.

1.2. INCORPORATION OF HEAT PUMPS IN INDUSTRIAL PROCESSES

As a common heat conductor, water is frequently used in industrial processes to remove the redundant heat and to cool down the facilities. Considerable amount of low grade waste heat conveyed by cooling water at levels of 45–60°C is rejected to the environment through main industrial facilities such as electric power plants, petroleum refineries, and chemical plants [3]. One way to recover this amount of thermal energy is to incorporate heat pump systems within these processes.

Heat pumps are a promising technology that can use thermal energy in high efficiency and thus achieve energy savings. It is the only heat recovery system that can raise temperature of waste heat to more useful levels [4]. The heat pump technology has great potential to recover thermal energy in many industrial processes. Take spent cooling water as an example, the low grade waste heat can be upgraded to higher grade heat as hot water or water vapor at high temperature for heating utility (such as district heating for buildings). While at the same time, a low temperature stream can be obtained from the heat pump cycle for cooling utility. This process is illustrated in Fig. 1.1. If the heat pump system can be operated with a high coefficient of performance (COP), a large amount of thermal energy can be saved, therefore it improves the overall efficiency of the industrial process.

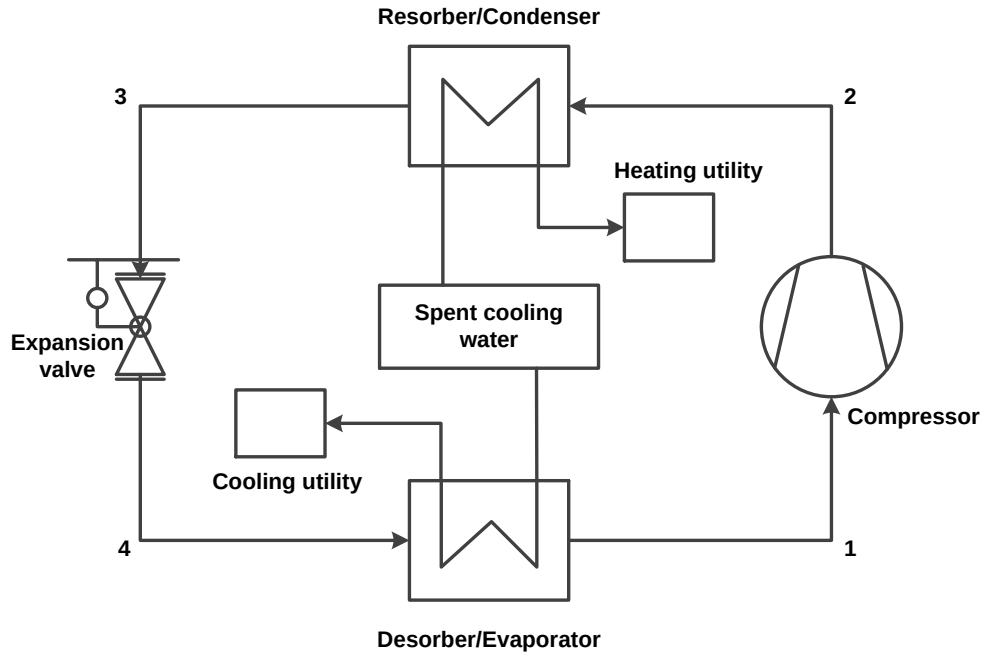

Figure 1.1: *Upgrading thermal energy from spent cooling water using a heat pump cycle. Modified from ref. [3]*

1.3. COMPRESSION RESORPTION HEAT PUMPS

A previous study by van de Bor [3] indicated that compression resorption heat pumps (CRHP) can be integrated with industrial processes to recover thermal energy and provide a higher COP compared to conventional vapor compression heat pumps (VCHP).

CRHP cycle with wet or dry compression has similar configuration as VCHP, as is shown in Fig. 1.1. The resorber and desorber are heat exchangers which correspond to the condenser and evaporator of VCHP. Condensation takes place in both the resorber and condenser. The difference is that the working fluid in VCHP is single-component, so that the condensation process is isothermal, while for CRHP the working fluid is multi-component, which has temperature change during condensation (or absorption) process in the resorber. This difference also applies between the evaporator and the desorber. The temperature change in the two-phase region during resorption and desorption processes is called the 'temperature glide', which can be matched with the temperature profile of the process flow to obtain the desired temperature level. This is one of the reasons that CRHP cycle can have higher COP than VCHP cycle, and the improvement is due to the smaller temperature difference compared to that of the VCHP cycle, this small temperature difference reduces the irreversibility of the system [5]. Fig. 1.2 qualitatively explains this improvement. The disadvantage of the temperature glide is that it decreases the mean temperature driving force of the heat exchanger, therefore a larger contact area is required and it will increase the investment cost of the heat exchanger [6]. Highly compact mini-channel heat exchangers can be applied to solve this problem. This will be discussed in the following section.

The working fluid for CRHP used in van de Bor's study is an ammonia–water binary mixture with approximately 35% ammonia concentration by mass. The advantage of the ammonia–water binary mixture is that it can achieve high temperature operation at relatively low operating pressures, also

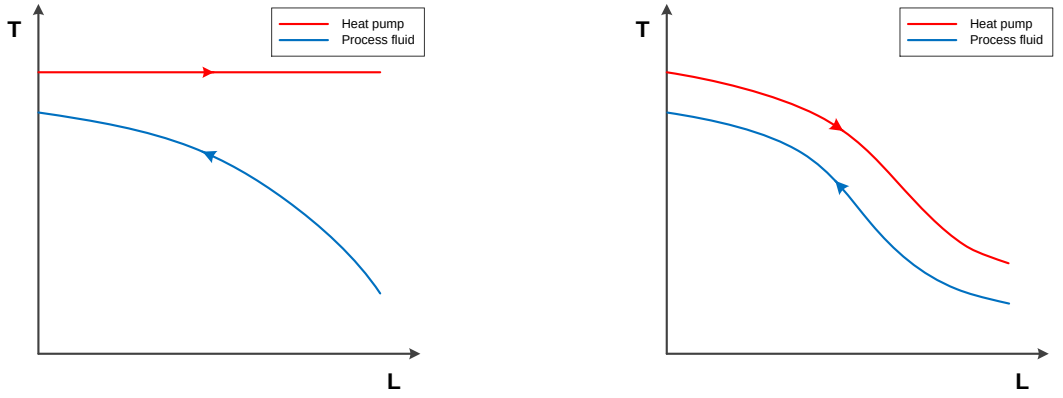

(a) Condenser (b) Resorber

Figure 1.2: *Temperature profile along the heat exchanger for condenser and resorber*

the cycle can be designed to show a temperature glide in the resorber that corresponds to the temperature glide of the industrial flow that has to be heated [3]. Recently the CO_2–NH_3–H_2O ternary mixture has been identified as a possible working fluid for CRHP, and a preliminary study suggests that it has better performance than ammonia–water [7]. Since the absorption of CO_2 in aqueous ammonia is an exothermic chemical reaction process, more latent heat is supposed to be discharged during the absorption process than in the conventional ammonia–water absorption process. If the compressor can operate with similar efficiency, CRHP using CO_2–NH_3–H_2O mixture are expected to perform with higher efficiency than when using simply ammonia–water.

1.4. MINI-CHANNEL HEAT EXCHANGER

As previously mentioned, highly compact heat exchangers should be applied in CRHP systems in order to compensate the low temperature driving force due to the temperature glide of the mixture. Here 'highly compact' denotes a larger heat transfer area than normal heat exchangers, therefore the volume area ratio (the quotient of the volume of the heat exchanger divided by its heat transfer area) of the heat exchanger should be lower. For a shell and tube heat exchanger, this can be realized by decreasing the diameter of the tubes and increasing the compactness of the tube distribution.

A multi-tube mini-channel heat exchanger is applied in this study. The configuration of the heat exchanger will be illustrated in chapter 4. Besides the larger heat exchange area, it also can perform with a higher overall heat transfer coefficient than normal size heat exchangers [8]. To simulate the heat transfer phenomenon within the mini-channel, the challenge is that whether the methods for normal size heat exchangers are applicable.

1.5. OBJECTIVES

As an important component in CRHP cycle, resorber performance is theoretically and experimentally investigated in this study. The current work performs experiments in a mini-channel heat exchanger using both ammonia–water binary mixture and CO_2–NH_3–H_2O ternary mixture to study the absorption (condensation) process of a CRHP cycle. A corresponding mathematical model is developed to simulate the absorption process of an ammonia–water mixture, while experimental

data are used to validate the proposed model. Specific objectives of this thesis are listed below:

- To develop a theoretical model that predicts the absorption process inside a specific mini-channel heat exchanger with ammonia–water binary mixture.
- To perform ammonia–water absorption experiments within the mini-channel heat exchanger and validate the theoretical model with the experimental data.
- To perform CO_2–NH_3–H_2O absorption experiments within the mini-channel heat exchanger and validate different thermodynamic models with the experimental data.
- To analyze the experimental data and compare the performance between two different working fluids.

1.6. REPORT OUTLINE

Chapter 2 reviews previous studies about absorption process in mini-channel heat exchangers. Relevant background knowledge such as CO_2 absorption kinetic models and CO_2–NH_3–H_2O thermodynamic models are introduced.

Chapter 3 explains the development of the theoretical model for ammonia–water absorption simulation.

Chapter 4 shows the experimental implementation. Experimental results and data analysis are also explained in this chapter.

Chapter 5 covers the validation of the models with the experimental data. Further investigations and discussions are also included.

Chapter 6 finally presents the conclusions of the study and gives recommendations for future work.

2

THEORETICAL BACKGROUND

2.1. PREVIOUS STUDIES FOR AMMONIA–WATER ABSORPTION IN A MINI-CHANNEL HEAT EXCHANGER AT THE TU DELFT

Van Leeuwen [8] experimentally investigated absorption and desorption of ammonia–water mixtures in a tube-in-tube mini-channel heat exchanger and built a theoretical model to simulate these processes. The absorption of ammonia–water mixture for two-phase flow is conducted in the annular side and flows from top to bottom, while the desorption is conducted in the tubular side and flows in the opposite direction. The study focused on the overall heat transfer coefficient of the heat exchanger. It is concluded that mini-channel heat exchangers provide a considerably higher overall heat transfer coefficient than conventional heat exchangers. The research also showed that the dominant flow pattern on both sides is slug flow. The theoretical model can predict the overall heat transfer coefficient within ±50% accuracy, but failed to predict the pressure drop.

Rijpkema [6] further developed a model following the approach by van Leeuwen [8] to predict the performance of the ammonia–water mixture in a tube-in-tube mini-channel heat exchanger, and the influence of the surface tension was investigated. The results show that modeling of surface tension has little effect on the absorption side, while on the desorption side it has significant effect. The model takes into account both annular and slug flow patterns, and the result indicates that the choice of a flow pattern hardly affects the overall results for the absorption process in the annular side. Compared to the experimental results, the simulation results of temperature glide, pressure drop and heat load from the model show reasonable agreement within ±30–40% accuracy, while the overall heat transfer coefficient is significantly over predicted. This maybe due to the over prediction of heat transfer coefficient on the absorption side.

Nefs [9] performed experiments using a multi-tube mini-channel heat exchanger to study the absorption and desorption processes of an ammonia–water mixture. The experiments were conducted with absorption on the shell side and desorption on the tube side. The experimental results showed that hydrodynamic instabilities occur in the heat exchanger. Nefs also tried to extend Rijpkema's model [6] to fit to the new multi-tube mini-channel heat exchanger prototype. The distributors of the heat exchanger are investigated in detail and possible heat transfer correlations are proposed. Unfortunately the theoretical model was not completed for both the absorption and desorption process. Also the numerical results for the absorption process showed large deviations from the experimental data.

2.2. THERMODYNAMIC MODELS FOR CO_2–NH_3–H_2O MIXTURE

Thermodynamic models have been developed in the past several decades to fit the experimental data with the CO_2–NH_3–H_2O mixture. Among different models, the extended UNIQUAC model and the e-NRTL model are frequently mentioned in previous studies.

The extended UNIQUAC (short for UNIversal QUAsiChemical) model was first proposed by Thomsen and Rasmussen [10] in 1999. It is a local composition model derived from the original UNIQUAC model. The model uses the extended UNIQUAC model to calculate activity coefficients for the liquid phase and the Soave-Redlich-Kwong equation of state for vapor phase calculations [7] and allows for calculating the activity coefficients of electrolyte solutions [11]. The model is further modified by Darde et al. [12]. This upgraded extended UNIQUAC model was compared to one modified version (released in ASPEN Plus version 7.2) of the e-NRTL model by Darde et al. [11] and the results show that the extended UNIQUAC model generally performed better than the e-NRTL model especially for the partial pressure of ammonia and the solubility of ammonium bicarbonate.

The e-NRTL (short for electrolyte non-random two-liquid) model introduced by Chen et al. [13] in 1982 is a widely accepted model used to describe CO_2–NH_3–H_2O equilibrium. It is a comprehensive excess Gibbs energy expression to represent the liquid phase nonideality for aqueous and mixed-solvent electrolyte systems over the entire concentration range from pure solvents to saturated solutions or fused salts. After the study from Darde et al. [11], to make it more competitive with the extended UNIQUAC model, the e-NRTL model has been further modified by for example Que and Chen [14] and Niu et al. [15]. The modified model by Que and Chen [14] is included in the current commercial ASPEN Plus package and has been used by various researchers.

Recently Gudjonsdottir and Infante Ferreira [7] have reviewed the models stated above and compared the extended UNIQUAC model with various modified e-NRTL models, also a new fit of the e-NRTL model was included to extend the ammonia concentration range of the model by Que and Chen [14], whose highest limit for ammonia concentration is reported as 30 wt%. The results show that the model modified by Que and Chen [14] and the new fit are especially competitive with the extended UNIQUAC model. The solid liquid equilibrium problem in the model modified by Que and Chen [14] can be partly solved by the new fit.

2.3. KINETICS OF CO_2 ABSORPTION IN AMMONIA–WATER

Carbon dioxide absorption in aqueous ammonia (ammonia–water mixture) has been studied during the last decades especially for post combustion capture (PCC) usage. Different researchers have investigated kinetic theory of the absorption of CO_2 in aqueous ammonia, numerous experiments and models have been conducted and developed. Due to different utilization purposes, the operating conditions (e.g. temperature range, pressure level, ammonia concentration, etc.) for PCC differs from those for CRHP. Nevertheless the methods used to explain the kinetics of the absorption process are worth studying.

The absorption of CO_2 in aqueous ammonia is a chemical absorption process which involves complex mechanisms both of thermodynamic and chemical nature [16]. It is necessary to determine reaction kinetics within the liquid bulk. Two approaches on the mechanism of CO_2 reactions with aqueous ammonia are widely used in previous studies, they are the zwitter-ion mechanism and the termolecular mechanism.

2.3.1. ZWITTER-ION MECHANISM

The zwitter-ion mechanism was first introduced by Caplow [17] and further discussed by Danckwerts [18]. The carbamate formation in this mechanism is explained to be formed in two steps. The reaction between CO_2 and ammonia first proceeds through the formation of a zwitter-ion as an intermediate:

$$CO_2 + NH_3 \overset{k_2/k_{-1}}{\longleftrightarrow} NH_3^+COO^- \tag{2.1}$$

where k_2 is the forward reaction rate constant, and k_{-1} is the backward reaction rate constant. Reaction rate constant is temperature dependent and can be expressed using the Arrhenius equation:

$$k = Ae^{-\frac{E_a}{RT}} \tag{2.2}$$

where A is the pre-exponential factor, E_a is the activation energy, R is the universal gas constant, and T is the temperature in Kelvin. The reaction rate of the chemical reaction in equation 2.2 can be expressed as:

$$r^Z_{step1} = k_2[CO_2][NH_3] - k_{-1}[NH_3^+COO^-] \tag{2.3}$$

where the square brackets denote the concentrations of the corresponding chemicals, the superscript Z corresponds to zwitter-ion mechanism.
The formed zwitter-ion is very unstable and will be further deprotonated by a base to form carbamate immediately. The process can be elaborated by the following equation:

$$NH_3^+COO^- + B \overset{k_B}{\longleftrightarrow} NH_2COO^- + BH^+ \tag{2.4}$$

where B represents 'base', in aqueous ammonia, H_2O and NH_3 are dominant bases; k_B is the forward reaction rate constant. The reaction rate of this chemical reaction can be expressed as:

$$r^Z_{step2} = k_B[NH_3^+COO^-][B] \tag{2.5}$$

Applying the steady-state principle to the intermediate zwitter-ion [19], the reaction rate between CO_2 and NH_3 is:

$$r^Z_{CO_2-NH_3} = r^Z_{step1} = r^Z_{step2} \tag{2.6}$$

By solving equations 2.3, 2.5, and 2.6 simultaneously, the reaction rate between CO_2 and NH_3 can be expressed as:

$$r^Z_{CO_2-NH_3} = \frac{[CO_2][NH_3]}{\frac{1}{k_2} + \frac{k_{-1}}{k_2}\frac{1}{\sum k_B[B]}} \tag{2.7}$$

Assuming that ammonia and water are the dominant bases in aqueous ammonia [20], the reaction rate between CO_2 and NH_3 will eventually be expressed as:

$$r^Z_{CO_2-NH_3} = \frac{[CO_2][NH_3]}{\frac{1}{k_2} + \frac{1}{k^Z_{NH_3}[NH_3] + k^Z_{H_2O}[H_2O]}} \tag{2.8}$$

where $k^Z_{NH_3} = k_2 k_{NH_3}/k_{-1}$, $k^Z_{H_2O} = k_2 k_{H_2O}/k_{-1}$.
The following reactions may also take place simultaneously in an aqueous solution:

$$NH_3 + H_2O \leftrightarrow NH_4^+ + OH^- \tag{2.9}$$

$$H_2O \leftrightarrow H^+ + OH^- \tag{2.10}$$

$$CO_2 + OH^- \overset{k_{OH^-}}{\longleftrightarrow} HCO_3^- \tag{2.11}$$

$$CO_2 + H_2O \overset{k_{H_2O}}{\longleftrightarrow} HCO_3^- + H^+ \tag{2.12}$$

The reaction rates of the chemical reactions 2.11 and 2.12 can be expressed as:

$$r_{CO_2-OH^-} = k_{OH^-}[CO_2][OH^-] \tag{2.13}$$

$$r_{CO_2-H_2O} = k_{H_2O}[CO_2][H_2O] \tag{2.14}$$

The total rate of all CO_2 reactions in the aqueous ammonia solution is then given by the sum of the reaction rates in equations 2.8, 2.13, and 2.14:

$$r^Z_{overall} = \frac{[CO_2][NH_3]}{\frac{1}{k_2} + \frac{1}{k^Z_{NH_3}[NH_3]+k^Z_{H_2O}[H_2O]}} + k_{OH^-}[CO_2][OH^-] + k_{H_2O}[CO_2][H_2O] \tag{2.15}$$

The overall reaction rate can also be expressed as:

$$r^Z_{overall} = k^Z_{obs}[CO_2] \tag{2.16}$$

where k_{obs} denotes the observed reaction rate constant which is given by:

$$k_{obs} = \frac{[NH_3]}{\frac{1}{k_2} + \frac{1}{k^Z_{NH_3}[NH_3]+k^Z_{H_2O}[H_2O]}} + k_{OH^-}[OH^-] + k_{H_2O}[H_2O] \tag{2.17}$$

The observed reaction rate constant can be measured during experiments, the first term is called the apparent reaction rate constant (k_{app}), it is used to analyze the experimental data.

2.3.2. TERMOLECULAR MECHANISM

The termolecular mechanism was proposed by Crooks and Donnellan [21], and reintroduced by da Silva and Sendsen [22]. This mechanism suggests that a single-step third-order reaction mechanism is most likely for the formation of carbamate from CO_2 and alkanolamines in solutions. It means that the formation of the zwitter-ion and the deprotonization occur simultaneously. The reaction can be expressed as [23]:

$$CO_2 + NH_3 + B \overset{k_B}{\longleftrightarrow} NH_2COO^- + BH^+ \tag{2.18}$$

Assuming that ammonia and water are the dominant bases, the reaction rate can be expressed as:

$$r^T_{CO_2-NH_3} = (k^T_{NH_3}[NH_3] + k^T_{H_2O}[H_2O])[CO_2][NH_3] \tag{2.19}$$

where the superscript T corresponds to termolecular mechanism.
Similar to the discussion in the last subsection, the total rate of the all CO_2 reactions can be expressed as:

$$r^T_{overall} = (k^T_{NH_3}[NH_3] + k^T_{H_2O}[H_2O])[CO_2][NH_3] + k_{OH^-}[CO_2][OH^-] + k_{H_2O}[CO_2][H_2O] \tag{2.20}$$

and the observed reaction rate constant is given by:

$$k^T_{obs} = (k^T_{NH_3}[NH_3] + k^T_{H_2O}[H_2O])[NH_3] + k_{OH^-}[OH^-] + k_{H_2O}[H_2O] \tag{2.21}$$

The first term in the equation 2.21 is the apparent rate constant.

Table 2.1: *Summary of previous studies on chemical absorption of CO_2 using aqueous ammonia*

Researcher	Year	Ammonia concentration [wt%]	CO_2 loading [molCO_2/molNH_3]	Temperature range [K]	Kinetic model[1]	Experiment equipment[2]
Derks et al. [24]	2009	1–7.7	0	278–298	Z	SCR
Puxty et al. [25]	2009	1–10	0–0.8	278–293	–	WWC
Qin et al. [23]	2010	1.5–9.2	0	298–322	Z/T	SDC
Liu et al. [26]	2011	1–7.5	0	283–313	T	WWC
Darde et al. [20]	2011	1–10	0–0.8	279–304	Z	WWC

[1] for kinetic model, 'Z' stands for zwitter-ion; 'T' stands for termolecular.
[2] for experiment equipment, 'SCR' stands for stirred cell reactor; 'WWC' stands for wetted-wall column; 'SDC' stands for string of discs contactor.

2.3.3. SUMMARY OF PREVIOUS STUDIES

From the previous subsections, it can be concluded that the main difference between the zwitter-ion and the termolecular mechanisms is the way they analyze the formation of carbamate. This led to different apparent reaction rate constant expressions. For the zwitter-ion mechanism three constants (k_2, $k^Z_{NH_3}$, $k^Z_{H_2O}$) should be fitted based on experimental data, while for termolecular mechanism only two constants ($k^T_{NH_3}$, $k^T_{H_2O}$) should be fitted.

For PCC purpose, many researchers have used the two before mentioned mechanisms to process their experimental data and to develop models to predict the absorption rate of CO_2 in aqueous ammonia. Table 2.1 gives specifications for some typical experiments and models.

It can be observed from Table 2.1 that all the experiments were conducted at relatively low temperatures and ammonia concentrations. This was to prevent ammonia from changing phase due to vaporization during PCC processes. However this is not the case for a CRHP cycle. For example, to upgrade heat from waste cooling water, the temperature of the working fluid in the absorber should be over 100°C. Also the commonly used ammonia concentration for CRHP cycle is around 30–35 wt% at relatively low pressure levels [27]. A recent study from Aarts [28] predicts that if the wet compressor of the CRHP cycle can have as high isentropic efficiency as a dry compressor for VCHP cycle, to get minimum entropy production through the cycle, the optimum molar concentration of the ammonia is between 60 to 70%, which is much higher than those from the previous studies in Table 2.1.

2.4. CONCLUSIONS

Previous studies from TU Delft investigated NH_3–H_2O absorption process in tube-in-tube mini-channel heat exchangers. Absorption process in multi-tube mini-channel needs further study and a practical theoretical model needs to be developed. Numerous researchers did experiments and developed models to study the kinetics of CO_2 absorption in NH_3–H_2O for PCC use. The working conditions (composition, temperature, pressure levels, etc.) deviate much from that of a CRHP. It is difficult to verify its applicability for the operating condition of CRHP without relevant experimental data. Therefore it is not quite possible to develop a detailed theoretical model based on kinetics to simulate the absorption process of the CO_2–NH_3–H_2O mixture for CRHP use. Gudjonsdottir and Infante Ferreira [7] recently developed a new fit of the e-NRTL model to predict the thermodynamic properties for CO_2–NH_3–H_2O mixture. Relevant experiments need to be conducted to test the accuracy of the model.

3

THEORETICAL MODEL

A steady-state mathematical model has been developed using the computer software Matlab based on momentum, heat and mass transfer phenomena for ammonia–water mixture. The model considers heat and mass transfer between the vapor and liquid phase on the tube side, and heat transfer from the liquid phase to the water on shell side through the tube wall. After applying the finite control volume method, the absorption process is analyzed by simultaneously solving the equations for heat and mass transfer, and conservation equations for momentum, mass and energy balances. The model is developed based on the geometry of a real multi-tube mini-channel heat exchanger.

3.1. NH_3–H_2O ABSORPTION PROCESS

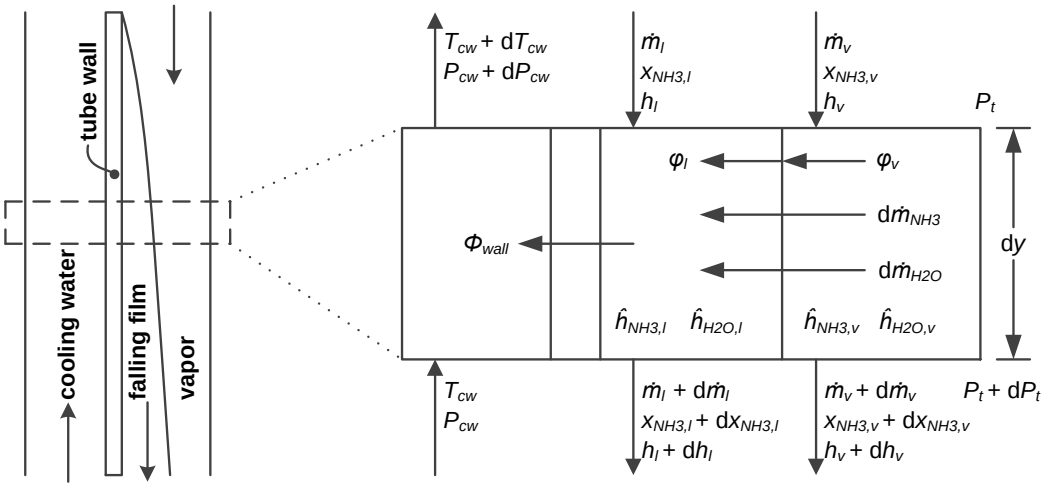

Figure 3.1: *Falling film profile and finite control volume profile*

The ammonia–water mixture condensates from vapor to liquid phase within the tube side of the mini-channel heat exchanger. This process can also be defined as vapor being absorbed into liquid. Within this study, the multi-tube mini-channel heat exchanger is positioned vertically, counter current flow is fulfilled by letting ammonia–water mixture flow downward on the tube side and cooling water flow upward on the shell side. The ammonia–water mixture vapor entering at the top releases heat to the cooling water side and condensates into liquid which attaches on the inner surfaces of

the vertical tube bundle. The thin film flows downward under inertia, pressure driving force and gravity, and becomes thicker along the tube, this phenomenon is defined as 'falling film flow'. Fig. 3.1 left shows the profile of the falling film formation along the tube. Within the control volume of the falling-film absorption (condensation) process, momentum, heat and mass transfer take place simultaneously: ammonia–water vapor releases mass and heat through the interface to the liquid side; ammonia–water liquid film receives heat and mass from the vapor phase, and releases heat through the tube wall to the cooling water side; cooling water is heated up caused by heat reception from the ammonia–water film. These phenomena are shown in Fig. 3.1 right.

The absorption process within the resorber has been qualitatively illustrated in a temperature-concentration diagram (Fig. 3.2). Saturated vapor mixture with certain ammonia concentration enters the absorber (point 1), and right after that it separates into two phases which is caused by the heat transfer to the cooling water side. The temperatures of both the liquid and vapor phases decrease during the absorption process. The vapor and liquid flows follow the solid curves from 1 to 2' and 1' to 2 respectively, while the total mixture flow follows the dashed line from 1 to 2. When the temperature reaches T_2, all the vapor has been absorbed (condensed) into liquid phase. Fig. 3.3 shows a local temperature profile transversal to the heat exchanger axis when the tube side is in 2-phase condition.

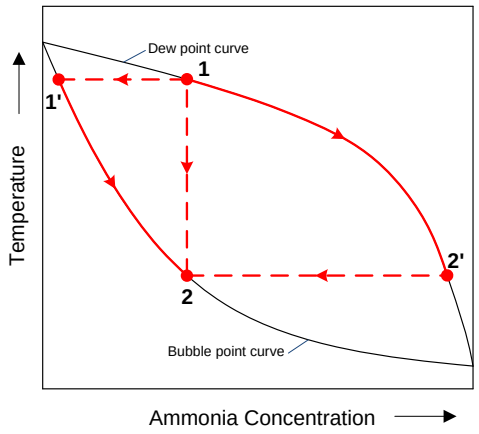

Figure 3.2: *Absorption process in a temperature-concentration diagram*

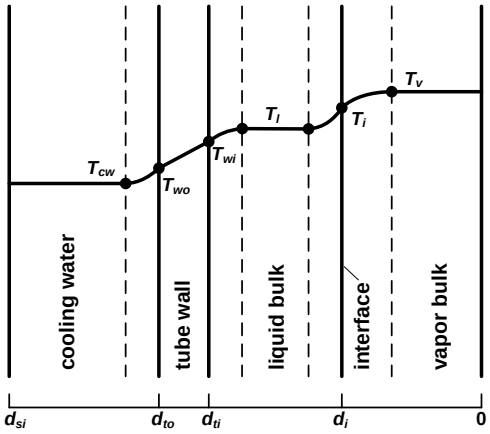

Figure 3.3: *Local temperature profile when the tube side is in 2-phase condition*

3.2. AMMONIA–WATER PROPERTIES

To develop the mathematical model, thermodynamic and transport properties of ammonia–water mixture are needed. Three independent parameters should be provided to determine the state of a binary mixture. For example, temperature, pressure and ammonia concentration are used to determine the state of the ammonia–water mixture within this model in most conditions.

The RefProp database [29] which uses the model from Tillner-Roth and Friend [30] is commonly used to determine the thermodynamic properties of the ammonia–water mixture. RefProp is based on the most accurate pure fluid and mixture models currently available, while the drawback is its slow calculation speed when compared to other simplified models or correlations. To reduce the processing time, a model from Rattner and Garimella [31] is used. This model can predict the key

thermodynamic properties of the ammonia–water mixture with satisfactory accuracy, and what is more important, it calculates much faster than RefProp. For transport properties, a document from the company M. Conde Engineering [32] is used. Table 3.1 summarizes the properties for ammonia–water mixture used within the theoretical model, and shows the corresponding model/software they are implemented with.

Table 3.1: *Important ammonia–water mixture properties and their corresponding model/software*

Property	Symbol	Unit	Model
Density	ρ	[kg m^{-3}]	Rattner & Garimella
Enthalpy	h	[J kg^{-1}]	Rattner & Garimella
Molar concentration	x	[mol mol^{-1}]	Rattner & Garimella
Dynamic viscosity	μ	[Pa s]	M. Conde
Thermal conductivity	λ	[W m^{-1} K^{-1}]	M. Conde
Diffusivity	D	[m^2 s^{-1}]	M. Conde
Heat capacity	c_p	[J kg^{-1} K^{-1}]	RefProp

3.3. FINITE CONTROL VOLUME

The whole mini-channel heat exchanger is subdivided into numerous small control volumes along the axial direction. This subdivision leads to simpler calculation procedure for each control volume with reasonable assumptions. Another advantage is that local properties and effects can be easily simulated, which gives better understanding about the whole absorption process within the heat exchanger. The smaller each control volume is subdivided, the more accurate result can be obtained, while the longer time it takes to run the simulation. For the current theoretical model, the 2-phase heat exchange area is subdivided into 4000 to 8000 control volumes based on different operating conditions. This is explained in detail in chapter 5.

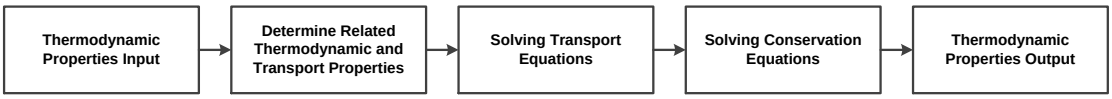

Figure 3.4: *Calculation procedure for one control volume*

When the control volume is small enough, it is reasonable to assume that the thermodynamic and transport properties along the axial direction are constant (homogenized), and the values are identical to the input thermodynamic properties at the boundary. One complete calculation procedure for a control volume is illustrated in Fig. 3.4. The whole calculation starts from one end of the heat exchanger. To begin with, sufficient thermodynamic properties should be given at this boundary, these properties are called the 'inputs'. Further on, all related thermodynamic and transport properties within this control volume can be determined. With these properties known, transport equations can be solved based on corresponding theories. Finally, conservation equations are applied and the thermodynamic properties at the other boundary can be determined, these properties are called the 'outputs', and they are sufficient for the calculations for the next cell.

3.4. MODEL ASSUMPTIONS

To simplify the model, the following assumptions are applied:

1. The whole process simulated by the mathematical model is assumed to be in steady state.
2. All tubes are well distributed and straight, no tube has bending.
3. Along the transversal direction, all tubes are identical, thermodynamic states within all tubes are identical. The cooling water is homogenized.
4. Falling-film phenomenon in the tube side is assumed. Annular flow is assumed to be dominant along the inner tube when in 2-phase condition. Other flow patterns are not taken into account.
5. The interface between the vapor and liquid phases in the tube side is considered to be in thermodynamic equilibrium.
6. Heat and mass transfer only occurs in the transversal direction of the flow.
7. The flow is assumed to be 1-D and it is in the axial direction.
8. The shell of the heat exchanger is assumed to be adiabatic, heat losses to the environment are neglected.
9. Radiative heat transfer is neglected through the whole process.
10. Fouling is neglected on both sides.
11. Entrance effects are neglected. Pressure drop at the distributors are not simulated.

3.5. TRANSPORT EQUATIONS

Transport equations are applied to calculate quantitatively the momentum, heat and mass transfer according to their driving force, respectively.

3.5.1. MASS TRANSFER

Mass transfer takes place between the ammonia–water vapor and liquid phases, it is caused by molecular diffusion combined with convection between the bulk flows and the interface.

The mass transfer direction from the vapor bulk to the liquid bulk is defined as positive. Based on Fick's first law of mass transfer, the molar flux of ammonia from the bulk vapor to the interface can be determined by equation 3.1, as proposed by Sieres and Fernández-Seara [33]:

$$J_{NH_3,v} = F_v \cdot z \cdot \ln\left(\frac{z - x_{NH_3,v,i}}{z - x_{NH_3,v}}\right) \tag{3.1}$$

where F_v is the mass transfer coefficient for the vapor bulk; $x_{NH_3,v,i}$ is the vapor phase ammonia molar concentration at the interface, it is the saturated vapor condition based on the local temperature and pressure at the interface; $x_{NH_3,v}$ is the ammonia molar concentration for the vapor bulk; z is defined as the ratio of ammonia molar flux to the total molar flux across the interface:

$$z = \frac{J_{NH_3}}{J} \tag{3.2}$$

Similarly, the molar flux of ammonia from the interface to the bulk liquid can be determined using equation 3.3.

$$J_{NH_3,l} = F_l \cdot z \cdot \ln\left(\frac{z - x_{NH_3,l}}{z - x_{NH_3,l,i}}\right) \tag{3.3}$$

The corresponding mass fluxes can be obtained when the molar fluxes are known:

$$G_{NH_3} = J_{NH_3} \cdot M_{NH_3} \tag{3.4}$$

$$G_{H_2O} = J_{NH_3} \cdot \frac{1-z}{z} \cdot M_{H_2O} \tag{3.5}$$

where M is the molar mass of the fluid.

Determine z

The mass flux ratio z can be determined by applying an iteration loop based on the mass balance at the interface. When in steady state, the mass fluxes coming into and exiting the interface should be equal, since no mass should be accumulated at the interface. This indicates:

$$J_{NH_3,v} = J_{NH_3,l} \tag{3.6}$$

z is first guessed and iterated until Equation 3.6 is fulfilled. Then z and the molar fluxes through the interface are determined.

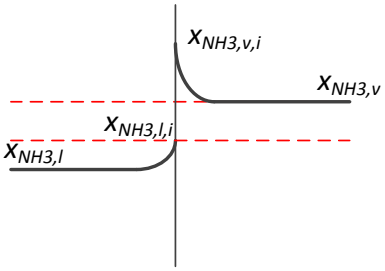

Figure 3.5: *Concentration profile across the interface. z should be between the red dashed lines. Modified from ref. [33]*

Sieres and Fernández-Seara [33] have investigated different thermodynamic processes according to various solutions of z. It is concluded that for a condenser or an absorber, the concentration profile at the interface should be analogous to that as shown in Fig. 3.5. In this case $x_{NH_3,v,i} > x_{NH_3,v}$, $x_{NH_3,l,i} > x_{NH_3,l}$ and $x_{NH_3,l,i} < x_{NH_3,v}$ occur with the condition that the interface temperature lower than either vapor or liquid phase saturation temperature. This in return gives an indication about how to estimate the interface temperature. For this case, a solution for z exists in the interval $x_{NH_3,l,i} < z < x_{NH_3,v}$.

Determine mass transfer coefficient

Mass transfer coefficients are determined using heat and mass transfer analogy. For laminar boundary layer flow, the conventional relationship is given by the following expression:

$$\frac{\mathrm{Nu}}{\mathrm{Sh}} = \left(\frac{\mathrm{Pr}}{\mathrm{Sc}}\right)^{\frac{1}{3}} \tag{3.7}$$

where Nu, Sh, Pr, Sc are dimensionless numbers known as: Nusselt number, Sherwood number, Prandtl number, and Schmidt number. They are defined as:

$$\mathrm{Nu} = \frac{h_c \cdot L}{\lambda} \tag{3.8}$$

$$\mathrm{Sh} = \frac{k_c \cdot L}{D} \tag{3.9}$$

$$\mathrm{Pr} = \frac{\nu}{\alpha} \tag{3.10}$$

$$\mathrm{Sc} = \frac{\nu}{D} \tag{3.11}$$

Combining equations 3.7, 3.8, and 3.9, the convective diffusion rate constant can be defined as:

$$k_c = \frac{h_c \cdot D}{\lambda} \cdot \left(\frac{\mathrm{Sc}}{\mathrm{Pr}}\right)^{\frac{1}{3}} \tag{3.12}$$

For turbulent flow, Chilton-Colburn analogy [34] can be applied to determine mass transfer coefficient. From the analogy between heat and mass transfer, following expression can be achieved:

$$k_c = \frac{h_c}{\rho \cdot c_p} \cdot \left(\frac{\mathrm{Pr}}{\mathrm{Sc}}\right)^{2/3} \tag{3.13}$$

With the convective diffusion rate constant known, the mass transfer coefficient can be calculated by:

$$F = c \cdot k_c \tag{3.14}$$

where c is the molar concentration and it can be expressed as:

$$c = \frac{\rho}{x_{NH_3} \cdot M_{NH_3} + (1 - x_{NH_3}) \cdot M_{H_2O}} \tag{3.15}$$

3.5.2. MOMENTUM TRANSFER

Reynolds number and average velocities of the fluids are important parameters to determine the friction factor, pressure drop, and heat transfer coefficients. Two methods can be applied to solve this problem: one is to solve the Navier-Stokes equations, therefore the velocity profile is determined; the other way is to apply existing relations to calculate film thickness thus the average velocities are determined. The advantage of solving the Navier-Stokes equations is that detailed velocity profile can be obtained, and the pressure drop along the tube can be determined at the same time. But for the current situation, to solve the Navier-Stokes equations, 5 non-linear differential equations with 5 unknowns should be solved simultaneously. This needs complicated and efficient solvers. Although film thickness relations have their limitations, for the current simulation problem it is an efficient method.

Film thickness

Rijpkema [6] studied the effect of surface tension on absorption process in the mini-channel heat exchanger, and concluded that the surface tension has negligible effect on the absorption process. Therefore for the falling film inside the tube, it can be assumed that the inertia, viscous force and gravity are dominant forces. VDI heat atlas [35] gives a correlation to determine the film thickness based on Nusselt falling film theory:

$$\delta = \left(\frac{3\nu^2}{g}\right)^{1/3} \mathrm{Re}^{1/3}; \quad \mathrm{Re} < 400 \tag{3.16}$$

$$\delta = 0.302 \left(\frac{3\nu^2}{g}\right)^{1/3} \mathrm{Re}^{8/15}; \quad \mathrm{Re} > 400 \tag{3.17}$$

where Re is the Reynolds number. It is defined as:

$$\mathrm{Re} = \frac{u \cdot L}{\nu} \tag{3.18}$$

Similar to z, the film thickness is also determined by an iteration loop. Film thickness is first guessed, the cross sectional area of the liquid phase can then be calculated, thus the average velocity and Reynolds number for the liquid phase can be determined, then another film thickness can be calculated using equations 3.16 or 3.17. The estimated value of the film thickness is iterated until the estimated one and the calculated one become identical within some small error boundary, then the film thickness is determined.

Pressure drop for 2-phase flow

Different models have been developed by researchers to predict the frictional pressure drop for 2-phase flow, for example: Friedel [36], Lockhart and Martinelli [37], Grönnerud [38], Müller Steinhagen and Heck [39], etc. Ould Didi et al. [40] compared the two-phase frictional pressure drop correlations and concluded that Müller Steinhagen and Heck model predicts the pressure drop best for annular flow. Therefore the model from Müller Steinhagen and Heck is used to predict the frictional pressure drop within this theoretical model.

The pressure drop of the two-phase flow caused by friction can be expressed as:

$$\left(\frac{\mathrm{d}P}{\mathrm{d}L}\right)_{tp} = C \cdot (1-q)^{1/3} + B \tag{3.19}$$

where

$$C = A + 2(B-A) \cdot q \tag{3.20}$$

The factors A and B are the frictional pressure gradients for the liquid and the vapor phase, respectively:

$$A = f_l \cdot \frac{G^2}{2\rho_l \cdot d} \tag{3.21}$$

$$B = f_v \cdot \frac{G^2}{2\rho_v \cdot d} \tag{3.22}$$

with

$$f_l = \frac{64}{\mathrm{Re}_l}, \quad f_v = \frac{64}{\mathrm{Re}_v} \quad \text{for } \mathrm{Re}_l,\ \mathrm{Re}_v \le 1187 \tag{3.23}$$

$$f_l = \frac{0.3164}{\mathrm{Re}_l^{1/4}}, \quad f_v = \frac{0.3164}{\mathrm{Re}_v^{1/4}} \quad \text{for } \mathrm{Re}_l,\ \mathrm{Re}_v > 1187 \tag{3.24}$$

Pressure drop for cooling water

The pressure drop caused by friction in the shell side for the single-phase cooling water can be calculated by:

$$\left(\frac{\mathrm{d}P}{\mathrm{d}L}\right)_{cw} = f_{cw} \cdot \frac{\rho_{cw} \cdot u_{cw}^2}{2d_h} \tag{3.25}$$

The tube bundle in the mini-channel heat exchanger does not have a common configuration: neither square nor triangular tube arrangement. According to Nefs [9], an estimation of the effective friction factor is given based on Reynolds analogy from the study of Mahulikar and Herwig [41]:

$$f_{cw} = 22 \tag{3.26}$$

3.5.3. HEAT TRANSFER

Heat transfer takes place in two main sections in the mini-channel heat exchanger: one is between the vapor and the liquid bulk through the interface; the other is between the liquid film and the cooling water through the tube wall.

Heat transfer through the interface

The heat passing through the interface from the vapor to the liquid phase consists of two parts: one part is caused by explicit heat transfer which is driven by the temperature difference; the other part is the energy passing through the interface due to mass transfer. This is shown in Fig. 3.6. When in steady state, there is no heat accumulated at the interface, therefore the heat flux coming from the vapor phase to the interface equals to the heat flux coming from the interface to the liquid film, this can be expressed as:

$$\phi_v + G_{NH_3} \cdot \hat{h}_{NH_3,v} + G_{H_2O} \cdot \hat{h}_{H_2O,v} = \phi_l + G_{NH_3} \cdot \hat{h}_{NH_3,l} + G_{H_2O} \cdot \hat{h}_{H_2O,l} \tag{3.27}$$

where ϕ_v and ϕ_l are the heat fluxes caused by temperature driving force, G is the mass flux through the interface, and $\hat{h}$ is the partial enthalpy.

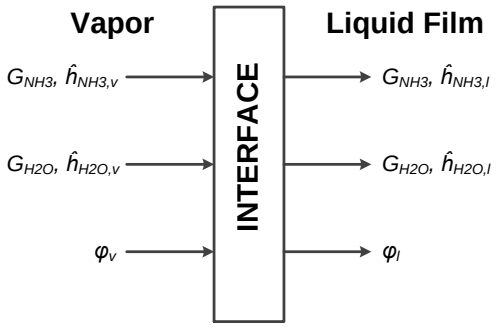

Figure 3.6: *Heat fluxes across the interface*

Explicit heat transfer and heat transfer coefficients

The explicit heat fluxes in equation 3.27 can be expressed as:

$$\phi_v = h_{c,v} \cdot (T_v - T_i) \tag{3.28}$$

$$\phi_l = h_{c,l} \cdot (T_i - T_l) \tag{3.29}$$

where h_c is the convective heat transfer coefficient, and it can be determined with the Nusselt number:

$$h_c = \frac{\mathrm{Nu} \cdot \lambda}{d_h} \tag{3.30}$$

The Nusselt numbers for both vapor and liquid film can be determined using the correlation from the VDI Heat Atlas [35] for forced convection in a circular tube (constant wall temperature condition):

$$\mathrm{Nu} = 2 \qquad \text{for } \mathrm{Re} < 30 \tag{3.31}$$

$$\mathrm{Nu} = 3.66 \qquad \text{for } \mathrm{Re} \leq 2300 \tag{3.32}$$

$$\mathrm{Nu} = \frac{(\xi/8)\mathrm{Re}\,\mathrm{Pr}}{1 + 12.7\sqrt{\xi/8}(\mathrm{Pr}^{2/3} - 1)} \qquad \text{for } \mathrm{Re} \geq 1 \cdot 10^4 \tag{3.33}$$

where friction factor ξ can be expressed by:

$$\xi = (1.8 \log_{10} \mathrm{Re} - 1.5)^2 \tag{3.34}$$

When the flow is in the transition region between laminar and fully developed turbulent flow ($2300 < \mathrm{Re} < 1 \cdot 10^4$), the Nusselt number can be determined using the following equation:

$$\mathrm{Nu} = (1-\gamma) \cdot \mathrm{Nu}_{lam,2300} + \gamma \cdot \mathrm{Nu}_{turb,10^4} \tag{3.35}$$

where $\mathrm{Nu}_{lam,2300}$ is the Nusselt number at $\mathrm{Re} = 2300$ calculated from equation 3.32, $\mathrm{Nu}_{turb,10^4}$ is the Nusselt number at $\mathrm{Re} = 1 \cdot 10^4$ calculated from equations 3.33 and 3.34, and the proportion factor γ is given by:

$$\gamma = \frac{\mathrm{Re} - 2300}{10^4 - 2300} \tag{3.36}$$

Partial enthalpy

The partial enthalpy is the enthalpy of one certain component within a multi-component mixture. For ammonia–water binary mixture, the partial enthalpies can be calculated using equations derived from Gibbs-Duhem equation suggested by Smith et al. [42]:

$$\hat{h}_{NH_3} = h(T,P,x_{NH_3}) + (1 - x_{NH_3}) \left[\frac{\partial h(T,P,x_{NH_3})}{\partial x_{NH_3}} \right]_{T,P} \tag{3.37}$$

$$\hat{h}_{H_2O} = h(T,P,x_{NH_3}) - x_{NH_3} \left[\frac{\partial h(T,P,x_{NH_3})}{\partial x_{NH_3}} \right]_{T,P} \tag{3.38}$$

Note that equations 3.37 and 3.38 can be applied to either vapor or liquid phase.

Heat transfer through the tube wall

According to Holman [43], heat transfer from the liquid film to the cooling water on the shell side through the tube wall can be calculated as:

$$\Phi_{wall} = \frac{T_l - T_{cw}}{\frac{1}{h_{c,cw} \cdot \pi \cdot d_{to} \cdot \mathrm{d}y} + \frac{\ln(d_{to}/d_{ti})}{2 \cdot \pi \cdot \lambda_w \cdot \mathrm{d}y} + \frac{1}{h_{c,l} \cdot \pi \cdot d_{ti} \cdot \mathrm{d}y}} \tag{3.39}$$

where d_{to} and d_{ti} are outer and inner diameters of the tube respectively, $\mathrm{d}y$ is the length of the control volume.

Heat transfer coefficient for the cooling water

As mentioned in section 3.5.2, the tube bundle in the mini-channel heat exchanger does not have a common configuration, also it does not have baffles as normal shell and tube heat exchangers do. Thus traditional relations to calculate the Nusselt number in the shell side are not available. Actually since there is no baffle within the heat exchanger, shell side flow phenomena are more like forced convection in a tube. Therefore the correlation from the VDI Heat Atlas [35] is applied, equations 3.31–3.36 are used to calculate the Nusselt number and the heat transfer coefficient for the cooling water on the shell side.

3.6. CONSERVATION EQUATIONS

Conservation equations are finally applied to close the calculation of one control volume. Output thermodynamic properties for the different fluids are calculated based on momentum, mass, and energy balances.

Conservation equations for the vapor

Flows at the boundaries of a vapor control volume are illustrated in Fig. 3.7. Heat and mass transfer to the liquid film through the interface.

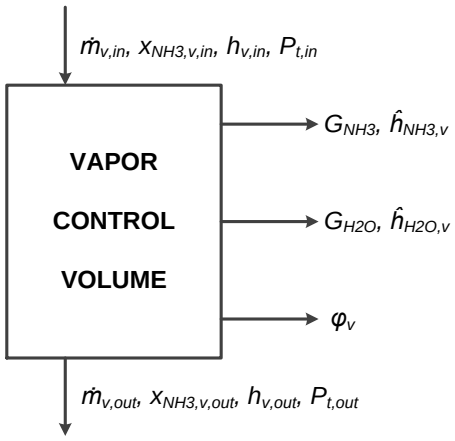

Figure 3.7: *Control volume of vapor on the tube side*

Mass balance:

$$\dot{m}_{v,in} = \dot{m}_{v,out} + (G_{NH_3} + G_{H_2O}) \cdot \mathrm{d}A_i \tag{3.40}$$

$$\dot{m}_{v,in} \cdot w_{NH_3,v,in} = \dot{m}_{v,out} \cdot w_{NH_3,v,out} + G_{NH_3} \cdot \mathrm{d}A_i \tag{3.41}$$

where w is the mass concentration, $\mathrm{d}A_i$ is the interface area of the control volume, it can be expressed as:

$$\mathrm{d}A_i = \pi(d_{ti} - 2\delta) \cdot \mathrm{d}y \tag{3.42}$$

Notice that equation 3.40 is the mass balance for the vapor bulk, output vapor mass flow can be determined by this equation. While equation 3.41 is the mass balance for ammonia, it is used to determine the output ammonia concentration.

Energy balance:

$$\dot{m}_{v,in} \cdot h_{v,in} = \dot{m}_{v,out} \cdot h_{v,out} + (G_{NH_3} \cdot \hat{h}_{NH_3,v} + G_{H_2O} \cdot \hat{h}_{H_2O,v} + \phi_v) \cdot \mathrm{d}A_i \tag{3.43}$$

Equation 3.43 is applied to determine the output vapor enthalpy.

Momentum balance:

$$P_{t,in} = P_{t,out} + \mathrm{d}P_t \tag{3.44}$$

where $\mathrm{d}P_t$ denotes the pressure drop within the control volume. Subscript 't' for 'tube side' is used because it is assumed that there is no momentum transfer between the vapor and the liquid film in the transversal direction, then the pressures of both the vapor bulk and the liquid film along transversal direction are identical.

Three independent thermodynamic properties (concentration, enthalpy, and pressure) are determined for the output boundary of the control volume based on the conservation equations stated above, they are sufficient to define the thermodynamic state of the vapor for the next cell.

Notice that the vapor is possible to enter the 2-phase region at the outlet. This will influence the calculation for the following control volumes, therefore further treatment should be processed to solve this problem. The 2-phase fluid at the outlet of the vapor bulk is separated into saturated vapor and liquid. The saturated vapor is remained as the vapor output of the control volume, while the saturated liquid is added to the liquid bulk control volume based on the mass and energy balances.

Conservation equations for the liquid film

Flows at the boundaries of a liquid film control volume are illustrated in Fig. 3.8. Heat and mass fluxes are transferred from the vapor through the interface, and another heat flow goes to the cooling water side through the tube wall.

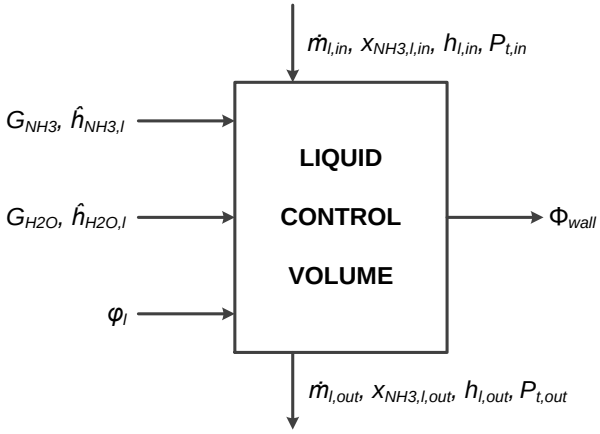

Figure 3.8: *Control volume of liquid film on the tube side*

Mass balance:

$$\dot{m}_{l,in} + (G_{NH_3} + G_{H_2O}) \cdot \mathrm{d}A_i = \dot{m}_{l,out} \tag{3.45}$$

$$\dot{m}_{l,in} \cdot w_{NH_3,l,in} + G_{NH_3} \cdot \mathrm{d}A_i = \dot{m}_{l,out} \cdot w_{NH_3,l,out} \tag{3.46}$$

Equation 3.45 and 3.46 are applied to determine the liquid mass flow and the ammonia concentration at the output boundary.

Energy balance:

$$\dot{m}_{l,in} \cdot h_{l,in} + (G_{NH_3} \cdot \hat{h}_{NH_3,l} + G_{H_2O} \cdot \hat{h}_{H_2O,l} + \phi_l) \cdot \mathrm{d}A_i = \dot{m}_{l,out} \cdot h_{l,out} + \Phi_{wall} \tag{3.47}$$

Equation 3.47 is applied to determine the output liquid enthalpy.

The momentum balance equation is identical to equation 3.44. Thus three independent thermodynamic properties (concentration, enthalpy, and pressure) are determined for the output boundary of the control volume, they are sufficient to define the thermodynamic state of the liquid for the next cell.

Conservation equations for the cooling water

Flows at the boundaries of a cooling water control volume are illustrated in Fig. 3.9. Heat fluxes are transferred from the liquid film through the tube wall. On the shell side it is a single phase flow with a pure fluid, thus mass balance is reduced to equality of mass flow at the inlet and the outlet.

Energy balance:

$$\dot{m}_{cw,in} \cdot h_{cw,in} + \Phi_{wall} = \dot{m}_{cw,out} \cdot h_{cw,out} \tag{3.48}$$

Equation 3.48 is applied to determine the output cooling water enthalpy.

Momentum balance:

$$P_{cw,in} = P_{cw,out} + \mathrm{d}P_{cw} \tag{3.49}$$

Therefore two independent thermodynamic properties (enthalpy and pressure) are determined for the output boundary of the control volume, they are sufficient to define the thermodynamic state of the cooling water for the next cell.

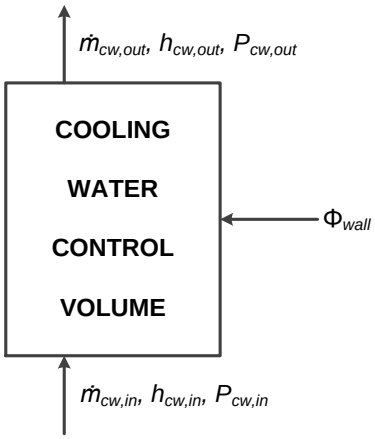

Figure 3.9: *Control volume of cooling water on the shell side*

3.7. MODEL IMPLEMENTATION

A steady-state model is implemented in Matlab with thermodynamic models/softwares mentioned in section 3.2. The flow sheet of the model implementation is illustrated in Fig. 3.10.

3.7.1. INITIALIZATION OF THE MODEL

Sufficient thermodynamic properties of one boundary of the mini-channel heat exchanger should be given to initialize the model. The calculation starts from the high temperature side, which corresponds to the inlet of the tube and the outlet of the shell at the top of the heat exchanger. Thus the properties at the inlet of the tube and the outlet of the shell are identified as the initial inputs of the model.

The pressure and the ammonia concentration of the binary mixture are two independent thermodynamic properties which can be easily measured or defined at the inlet of the tube. One more property is needed to determine the state at this local position. Two conditions may apply. One is to assume saturated vapor at the inlet, thus the vapor quality (1 for saturated vapor) is the third property given and the state is defined. The other condition is to assume 2-phase condition at the inlet. From the view of the experiments, the inlet vapor temperature can be easily measured, thus the vapor state is defined. If the inlet liquid temperature is assumed to be identical to the vapor temperature, there is no heat or mass transfer driving forces between the vapor and liquid phases, and it causes error to further process the simulation. Therefore a small temperature difference between the liquid and vapor should be roughly guessed to define the liquid state, and different trials showed that the guessed value barely influences the simulation results.

3.7.2. LOOPS AND ITERATIONS

The application of the finite control volume method has been illustrated in section 3.3, the general calculation procedure for one control volume has also been explained. Besides the loop for the cell grid arrangement, three other iterations have been applied and they can be observed in Fig. 3.10: the first one is the iteration for the film thickness, this is explained in section 3.5.2; the second one is the iteration to determine molar flux ratio z, and it is explained in section 3.5.1; the third one is to determine the interface temperature, the procedure is explained here. The interface temperature is guessed after tube side heat and mass transfer coefficients have been calculated. With this guessed temperature, thermodynamic properties like saturated vapor/liquid ammonia concentra-

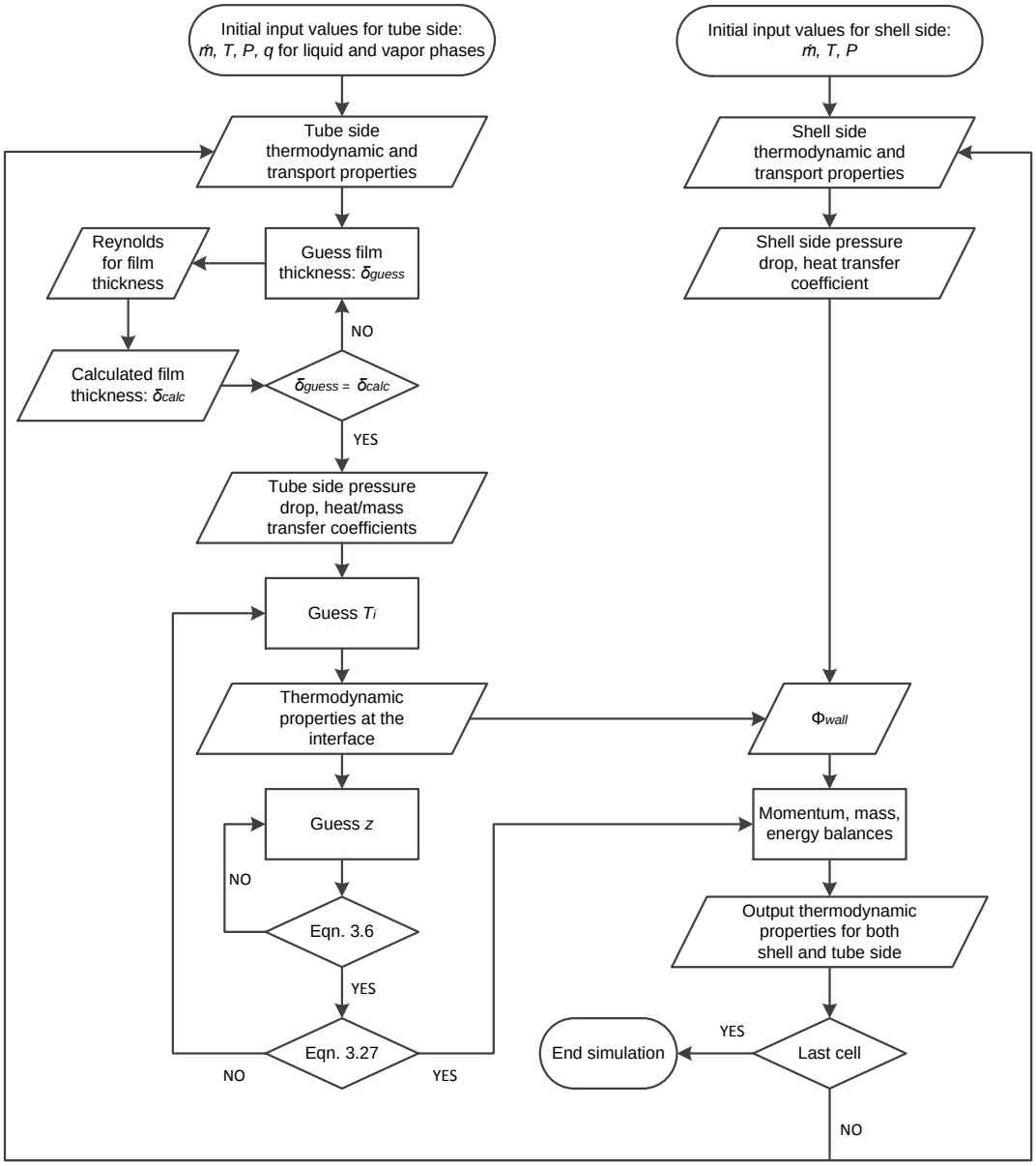

Figure 3.10: *Flow sheet of the computational model of the absorption process within a resorber*

tion and partial enthalpies for ammonia and water can be determined. Therefore the z iteration can be applied and the mass fluxes through the interface can be calculated. After that the energy balance at the interface (equation 3.27) is evaluated: if it fulfills, the calculation continues; otherwise a new interface temperature is guessed and the above stated procedures are repeated until the energy balance at the interface is fulfilled.

The first guesses of the film thickness δ, the molar flux ratio z and the interface temperature T_i should not be random but within some ranges, which are shown in table 3.2.

Table 3.2: *Reasonable ranges for guessing values of some parameters*

Property	Unit	Upper boundary	Lower boundary
Film thickness δ	[m]	$\leq d_{ti}/2$	≥ 0
Molar flux ratio z	[–]	$< x_N H_3, v$	$> x_{NH_3,l,i}$
Interface temperature T_i	[K]	$< T_{v,sat}, T_{l,sat}$ [1]	$> T_l$

[1] $T_{v,sat}, T_{l,sat}$ are vapor and liquid saturation temperatures corresponding to bulk ammonia concentrations, respectively. Derived from ref. [33].

The iterations are conducted in Matlab by applying the bisection method. The bisection method is a root-finding method that bisects an interval and selects a subinterval in which a root must lie for further processing. The method is simple and robust, but processes relatively slowly, also a known interval within which the root lies must be given to initialize the calculation.

The model is implemented following the flow sheet in Fig. 3.10. The thermodynamic properties at the bottom side of the mini-channel heat exchanger can be achieved, and they can be validated with the experimental data. Also all relative properties at any local place inside the heat exchanger are available to be checked and validated with experimental results.

4

Experiments and Results

4.1. Experimental Setup

Fig. 4.1 shows the scheme of the experimental setup. The multi-tube mini-channel heat exchanger is vertically positioned in an individual fume hood. The ammonia–water binary mixture or CO_2–NH_3–H_2O ternary mixture is fed from top to bottom on the tube side of the mini-channel heat exchanger, while the water flows on the shell side counter-currently from bottom to top and is heated up by the mixture. The mini-channel heat exchanger acts as a resorber in CRHP cycle and it is the main test section of the experimental setup. The two cycles connected to the mini-channel are installed in another cabinet to ensure the inlet conditions of the mini-channel are as expected. The mini-channel is well insulated with rock wool material.

The reason to have the mixture flowing on the tube side is that no matter how well the heat exchanger is insulated, there will be heat loss to the environment from the shell side, and the amount of heat loss is hard to predict. Therefore to minimize the influence of the heat loss to the absorption side and to increase the accuracy of the model simulation, the mixture is set to flow on the tube side. Another reason is that Nefs [9] concluded in his study that the configuration of the shell side causes notable hydrodynamic instability which will lead to unstable flow pattern, thus lower the accuracy of the model prediction. To get rid of this problem, the mixture is set to flow on the tube side.

The mixture cycle is shown to the right of the mini-channel heat exchanger in Fig. 4.1. The pump compensates the pressure drop along the cycle and prompts the flow of the mixture in a certain direction through the system. A flow meter is installed after the pump to measure the flow rate. After that the fluid mixture is heated up by a tube-in-tube coil heat exchanger of which the hot side is filled with silicon oil flowing through a thermostatic bath. Extra heating is provided by an electric tracing coil to stabilize the temperature at the inlet of the heat exchanger. The mixture working fluid changes its phase from vapor to liquid on the tube side of the mini-channel by releasing heat to the water on the shell side. A plate heat exchanger is installed after the mini-channel to further cool down the mixture and make sure it is sub-cooled in order to prevent the pump from breaking down by the unabsorbed vapor. The cooling water flows counter-currently on the other side of the plate heat exchanger, its mass flow is always set to reach maximum to ensure the fluid mixture is sufficiently sub-cooled before entering the pump. The water cycle to the left of the mini-channel is identical to the mixture cycle stated above. The dimensions of the multi-tube mini-channel heat exchanger are listed in table 4.1.

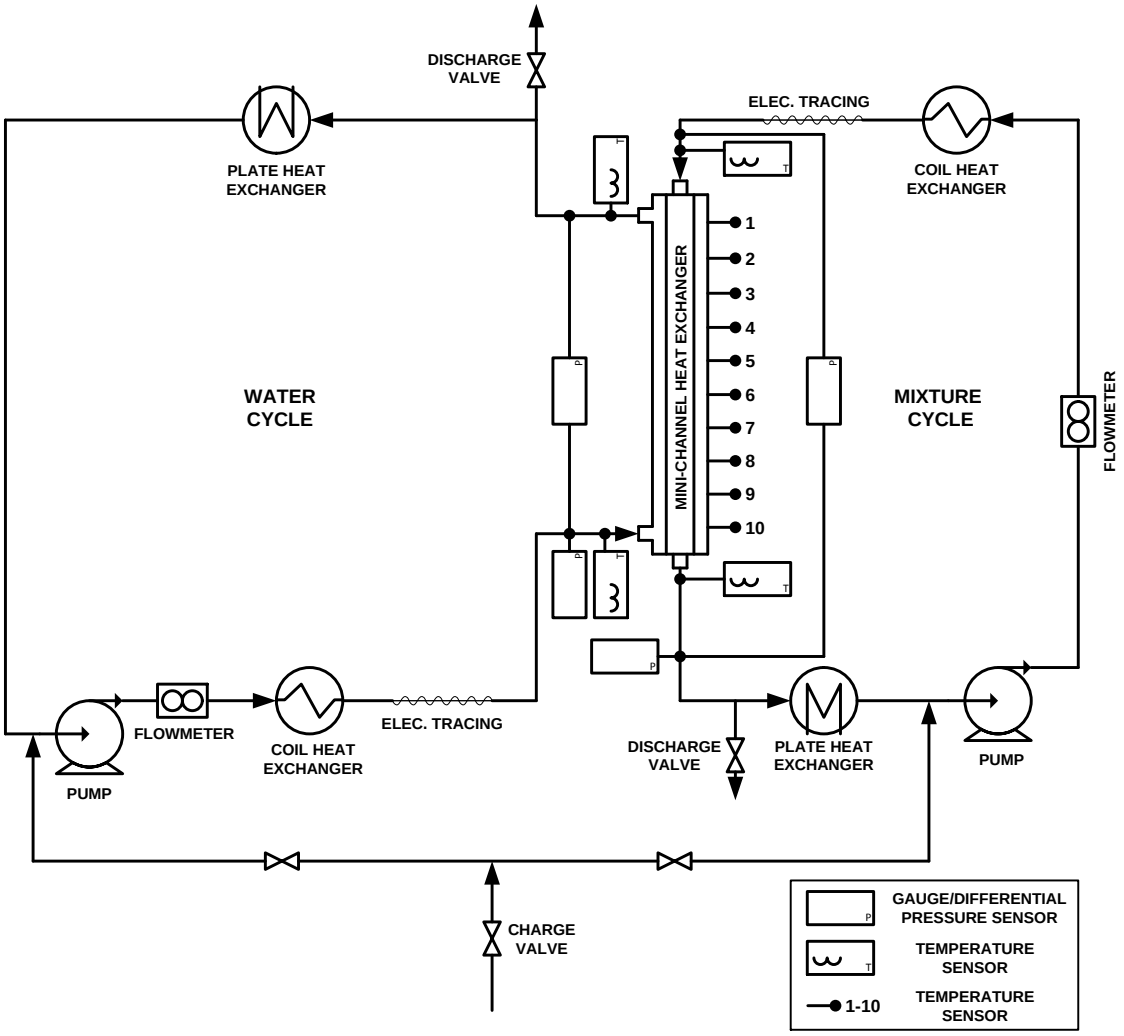

Figure 4.1: *Schematic diagram of the experimental setup*

Table 4.1: *Main dimensions of the multi-tube mini-channel heat exchanger*

Parameter	Unit	Value
Number of tubes	[–]	116
Total length of heat exchange section	[mm]	800
Inner diameter of the tube	[mm]	0.5
Outer diameter of the tube	[mm]	1.0
Inner diameter of the shell	[mm]	21.0
Outer diameter of the shell	[mm]	25.0

Two parameters can be controlled on each side of the setup: the mass flow and the temperature at the inlet of the test section (mini-channel heat exchanger). The fluids are heated up by the coil heat exchangers to the required temperature levels. There is a long pipeline connection between the outlet of the coil heat exchanger and the mini-channel inlet. The heat loss along the pipeline is notable but difficult to estimate, and it will cause instability of the heat exchanger inlet temperature. For this reason, electric tracing coils are installed at the inlets of the mini-channel to stabilize the

temperatures. Therefore the coil heat exchangers together with electric tracing coils make sure that the inlet temperatures of the mini-channel are as required. Four temperature sensors located at the in- and outlets of the mini-channel give back the measured local temperature simultaneously. The flow meters after the pumps are able to control the mass flow on both sides, they can also give back the values of the temperature and the density of the fluid at the local place where the flow meter is located. Two gauge pressure transmitters are installed to measure the pressures at the bottom side of the mini-channel on both sides, and two differential pressure transmitters are settled to measure the pressure difference on both sides of the mini-channel as shown in Fig. 4.1. Additionally 10 temperature sensors are averagely located along the shell of the mini-channel to investigate the temperature profile along the heat exchanger. This gives a temperature profile for the water side along the heat exchanger.

4.2. UNCERTAINTY ANALYSIS

Statistical analysis is applied to estimate the uncertainty of the measurements. Experimental data without uncertainty analysis are meaningless. In this section, instrument uncertainty for directly measured parameters is first introduced, error propagation is further introduced and applied to determine uncertainties for indirectly measured parameters.

4.2.1. INSTRUMENT UNCERTAINTY

Each instrument has an inherent amount of uncertainty in its measurement, even the most precise device cannot give the actual value. In this section instrument uncertainties for different sensors and transmitters are illustrated according to the specifications from the manufacturers.

Temperature sensors

Four cable sensors (name as 'normal sensors') for temperature measurement are installed at the in- and outlets of the mini-channel heat exchanger. A platinum resistor is built into the temperature sensor, changes in temperature are reflected by changes in the electrical resistance so that the measured value of the resistance gives an analogue expression for the actual temperature. The specifications are listed in table 4.2.

Table 4.2: *Specifications of the temperature sensors*

Sensor	PT–100
Type	1/1 DIN B
Range	-50$\cdots$ 205°C
Uncertainty	$\pm(0.3+0.005\cdot T)$°C[1]

[1] Temperature T here is in °C.

Before starting the experiments, the normal temperature sensors have been calibrated using a high-precision temperature sensor (the uncertainty of this sensor is relatively small thus is neglected, name this sensor as 'standard sensor' from now on) and a thermostatic bath with water. The range of the calibration is between 20 to 80°C with an interval of 10 K. The results are shown in Fig. 4.2. The temperature difference shown on y-axis is determined as:

$$\mathrm{d}T = T_{meas} - T_{cali} \tag{4.1}$$

where T_{meas} denotes the temperature measured by the normal sensors, and T_{cali} denotes the temperature measured by the standard sensor.

From the result, it can be observed that all four sensors showed a linear increase of the temperature difference with the increasing temperature level. The correlations between the measured value and

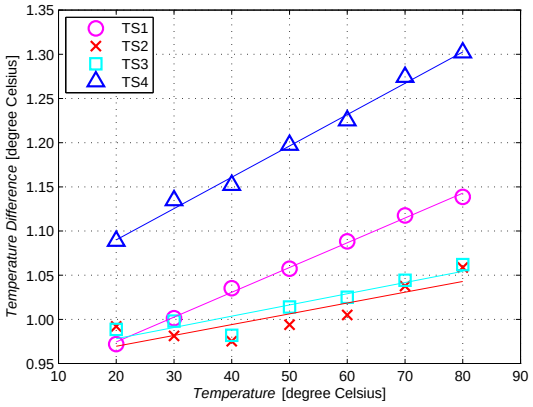

Figure 4.2: *Temperature sensors calibration result*

the calibrated value are adopted from Matlab:

$$TS1_{cali} = TS1_{meas} - (0.0028 \cdot TS1_{meas} + 0.9159) \tag{4.2}$$

$$TS2_{cali} = TS2_{meas} - (0.0012 \cdot TS2_{meas} + 0.9440) \tag{4.3}$$

$$TS3_{cali} = TS3_{meas} - (0.0013 \cdot TS3_{meas} + 0.9516) \tag{4.4}$$

$$TS4_{cali} = TS4_{meas} - (0.0035 \cdot TS4_{meas} + 1.0157) \tag{4.5}$$

After calibration, the uncertainties for $TS1$ to $TS4$ are 0.004 K, 0.022 K, 0.022 K, and 0.009 K respectively. Therefore for the following experiments, the temperatures measured by the four normal temperature sensors should be modified using equations 4.2 to 4.5 with their corresponding uncertainties.
The ten temperature sensors installed along the shell of the mini-channel are difficult to remove so they are not calibrated. The experimental results indicate that the accuracy of these sensors is quite low, but at least they can qualitatively show the temperature profile along the shell side.

Pressure sensors
Two types of pressure sensors: gauge pressure sensors and differential pressure sensors are installed in the setup. The gauge pressure sensors are located at the bottom side of the mini-channel on both shell and tube sides. They measure the local pressure of the fluid inside the tube. The specifications of the gauge pressure transmitter are listed in table 4.3. The differential pressure sensors are installed between the in- and outlets of both shell and tube sides to measure the pressure difference through the mini-channel. The corresponding specification can be found in table 4.4. Notice that r denotes the span ratio and it is defined as:

$$r = \frac{\text{maximum measuring span}}{\text{set measuring span}} \tag{4.6}$$

For the current experiments, the span ratio is 4 for the gauge pressure sensor, and 1 for the differential pressure sensor.

Flow meters
Flow meters are installed right after the pumps to measure the mass flow in the pipe based on Coriolis effect. Density and temperature of the fluid at the local position can be measured as well. The specifications for the flow meters are listed in table 4.5.

Table 4.3: *Specifications of the gauge pressure transmitters*

Sensor	Sitrans P, DS III
Type	7MF4033–1EA00–1AB6
Range	-1···+15 bar
Span ratio	4
Uncertainty	
linear	$\pm(0.0029 \cdot r + 0.071)\%$
long-term drift	$\pm(0.125 \cdot r)\%$ per 5 years[1]
ambient temperature influence	$\pm(0.08 \cdot r + 0.1)\%$
TOTAL	±1.0026%

[1] The transmitters have been running for 2 years by rough estimation.

Table 4.4: *Specifications of the differential pressure transmitters*

Sensor	Sitrans P, DS III
Type	7MF4433–1FA22–1AB6
Range	+0···+1600 mbar
Span ratio	1
Uncertainty	
linear	$\pm(0.0029 \cdot r + 0.071)\%$
long-term drift	$\pm(0.125 \cdot r)\%$ per years[1]
ambient temperature influence	$\pm(0.08 \cdot r + 0.1)\%$
TOTAL	±0.5039%

[1] The transmitters have been running for 2 years by rough estimation.

Table 4.5: *Specifications of the flow meters*

Sensor	mini Cori–Flow
Type	M14
Range	+0···+30 kg/h
Uncertainty	
liquid mass flow	±0.2%
gas mass flow	±0.5%
density	±5 kg/m^3
temperature	±0.5°C

4.2.2. ERROR PROPAGATION

Some of the parameters cannot be measured directly using a single measurement, they should be calculated combining several other parameters. The calculation of the errors of the variables derived from the measured data is called error propagation. Taylor [44] explained the method to determine the uncertainty of an indirectly measured parameter. The general rule is stated here.

Suppose that $x, \cdots, z$ are measured with uncertainties $U_x, \cdots, U_z$ and the measured values are used to compute the uncertainty of a parameter $p(x, \cdots, z)$. If the uncertainties in $x, \cdots, z$ are independent and random, then the uncertainty of the parameter p can be calculated as:

$$U_p = \sqrt{\left(\frac{\partial p}{\partial x} U_x\right)^2 + \cdots + \left(\frac{\partial p}{\partial z} U_z\right)^2} \tag{4.7}$$

For the indirectly measured parameters $q(x, \cdots, z)$ whose explicit functional relationship are un-

known, the following method can be applied to estimate its uncertainty:

$$U_q = \sqrt{\left(q(x+U_x,\cdots,z)-q(x,\cdots,z)\right)^2+\cdots+\left(q(x,\cdots,z+U_z)-q(x,\cdots,z)\right)^2} \tag{4.8}$$

Uncertainty of the heat flow $\dot{Q}$

The heat released or absorbed by a fluid with a constant mass flow can be calculated using the following equation:

$$\dot{Q} = \dot{m}\cdot(h_{out}-h_{in}) \tag{4.9}$$

where h is the specific enthalpy of the fluid. If the fluid is a binary mixture, three independent thermodynamic parameters are needed to determine its status, for example:

$$h = h(T,P,w_{NH_3}) \tag{4.10}$$

Based on equation 4.7, the uncertainty of the heat flow can be expressed as:

$$U_{\dot{Q}} = \sqrt{\left(\frac{\partial\dot{Q}}{\partial\dot{m}}U_{\dot{m}}\right)^2+\left(\frac{\partial\dot{Q}}{\partial h_{out}}U_{h_{out}}\right)^2+\left(\frac{\partial\dot{Q}}{\partial h_{in}}U_{h_{in}}\right)^2} \tag{4.11}$$

The uncertainty of the mass flow is illustrated in table 4.5. For the enthalpy which is determined by equation 4.10, its uncertainty can be determined based on equation 4.8:

$$U_h = \sqrt{(h(T+U_T,P,w)-h(T,P,w))^2+(h(T,P+U_P,w)-h(T,P,w))^2+(h(T,P,w+U_w)-h(T,P,w))^2} \tag{4.12}$$

Uncertainty of the logarithm mean temperature difference

For a counter-current flow in a shell and tube heat exchanger, the logarithm mean temperature difference is defined as:

$$\Delta T_{lm} = \frac{(T_{t,in}-T_{s,out})-(T_{t,out}-T_{s,in})}{\ln\left(\frac{T_{t,in}-T_{s,out}}{T_{t,out}-T_{s,in}}\right)} \tag{4.13}$$

Therefore the uncertainty of the logarithm mean temperature difference can be expressed as:

$$U_{\Delta T_{lm}} = \sqrt{\left(\frac{\partial\Delta T_{lm}}{\partial T_{t,in}}U_{T_{t,in}}\right)^2+\left(\frac{\partial\Delta T_{lm}}{\partial T_{s,out}}U_{T_{s,out}}\right)^2+\left(\frac{\partial\Delta T_{lm}}{\partial T_{t,out}}U_{T_{t,out}}\right)^2+\left(\frac{\partial\Delta T_{lm}}{\partial T_{s,in}}U_{T_{s,in}}\right)^2} \tag{4.14}$$

where,

$$\frac{\partial\Delta T_{lm}}{\partial T_{t,in}} = \frac{1}{\ln\left(\frac{T_{t,in}-T_{s,out}}{T_{t,out}-T_{s,in}}\right)}-\frac{(T_{t,in}-T_{s,out})-(T_{t,out}-T_{s,in})}{\left[\ln\left(\frac{T_{t,in}-T_{s,out}}{T_{t,out}-T_{s,in}}\right)\right]^2\cdot(T_{t,in}-T_{s,out})} \tag{4.15}$$

$$\frac{\partial\Delta T_{lm}}{\partial T_{s,out}} = -\frac{1}{\ln\left(\frac{T_{t,in}-T_{s,out}}{T_{t,out}-T_{s,in}}\right)}+\frac{(T_{t,in}-T_{s,out})-(T_{t,out}-T_{s,in})}{\left[\ln\left(\frac{T_{t,in}-T_{s,out}}{T_{t,out}-T_{s,in}}\right)\right]^2\cdot(T_{t,in}-T_{s,out})} \tag{4.16}$$

$$\frac{\partial\Delta T_{lm}}{\partial T_{t,out}} = -\frac{1}{\ln\left(\frac{T_{t,in}-T_{s,out}}{T_{t,out}-T_{s,in}}\right)}+\frac{(T_{t,in}-T_{s,out})-(T_{t,out}-T_{s,in})}{\left[\ln\left(\frac{T_{t,in}-T_{s,out}}{T_{t,out}-T_{s,in}}\right)\right]^2\cdot(T_{t,out}-T_{s,in})} \tag{4.17}$$

$$\frac{\partial\Delta T_{lm}}{\partial T_{s,in}} = \frac{1}{\ln\left(\frac{T_{t,in}-T_{s,out}}{T_{t,out}-T_{s,in}}\right)}-\frac{(T_{t,in}-T_{s,out})-(T_{t,out}-T_{s,in})}{\left[\ln\left(\frac{T_{t,in}-T_{s,out}}{T_{t,out}-T_{s,in}}\right)\right]^2\cdot(T_{t,out}-T_{s,in})} \tag{4.18}$$

Uncertainty of the overall heat transfer coefficient

The overall heat transfer coefficient E can be determined when the transferred heat through the heat exchanger is known:

$$E = \frac{\dot{Q}}{A \cdot \Delta T_{lm}} \tag{4.19}$$

where A is the heat transfer area. If its uncertainty is neglected, the uncertainty of the overall heat transfer coefficient can be expressed as:

$$U_E = \sqrt{\left(\frac{\partial E}{\partial \dot{Q}} U_{\dot{Q}}\right)^2 + \left(\frac{\partial E}{\partial \Delta T_{lm}} U_{\Delta T_{lm}}\right)^2} \tag{4.20}$$

where,

$$\frac{\partial E}{\partial \dot{Q}} = \frac{1}{A \cdot \Delta T_{lm}} \tag{4.21}$$

$$\frac{\partial E}{\partial \Delta T_{lm}} = -\frac{\dot{Q}}{A \cdot (\Delta T_{lm})^2} \tag{4.22}$$

The uncertainty of the heat flow and the logarithm mean temperature difference can be calculated using equations 4.11 and 4.14.

4.3. EXPERIMENTAL PROCEDURE

Most of the sensors are connected to a remote computer. The readings from the sensors and transmitters are instantaneously displayed in LabView, a system-design platform for a visual programming language. With LabView it is also possible to set the mass flow of the pump with the control of the flow meter.

The experimental setup is designed to be capable of changing the flow directions on both shell and tube sides by altering three-way valves. Before start up, the valves should be adjusted to confirm the flow direction. Then the system should be turned on and the pump mass flow is set as required. The inlet temperatures of the mini-channel are determined by adjusting the thermostatic bath temperature of the coil heat exchanger and the temperature of the electric tracing until the inlet temperatures are as required. The in- and outlet temperatures and the pressures are plotted as a function of time instantaneously in LabView, this helps to determine whether the system is operated in steady state (when steady, values are constant with a horizontal line shown in the diagram). Experimental data is logged for 15–20 minutes when the setup is running in steady state. To prevent extreme values caused by fluctuation, the average values are calculated from the logged data and are summarized as the experimental results.

Example data logging

Fig. 4.3 to 4.6 show a set of experimental data directly logged from LabView for one operating condition during the ammonia–water/water experiment. The x-axis in the diagrams denotes the logging time. LabView logs data in an interval of 0.1 second, while for the current setup it records measured data from the sensors every three seconds. The mass flows are 17.5 kg/h and 2.7 kg/h on the shell and tube side, respectively, this is shown in Fig. 4.3. It can be observed that both mass flows are stable although on the tube side there are tiny fluctuations, they can be caused by density change due to temperature variation or unabsorbed ammonia–water vapor. For CO_2–NH_3–H_2O/water experiment this fluctuation became worse, and steady state could not be reached for all desired operating conditions. This will be explained in more detail in the following sections. Fig. 4.6 shows the pressures measured directly from the gauge pressure sensors. The pressure on the shell side is steady

while on tube side it fluctuates within a range, this is caused by hydrodynamic instabilities due to the unstable 2-phase flow within the heat exchanger.

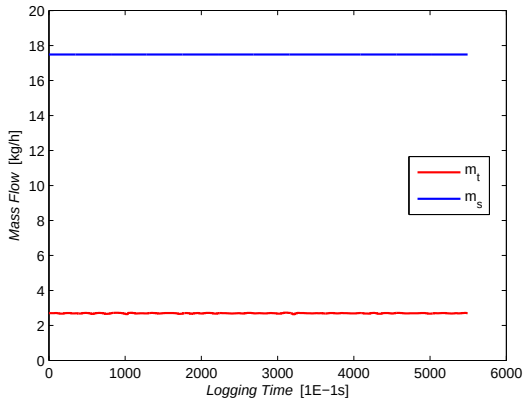

Figure 4.3: *Example data logging: mass flows*

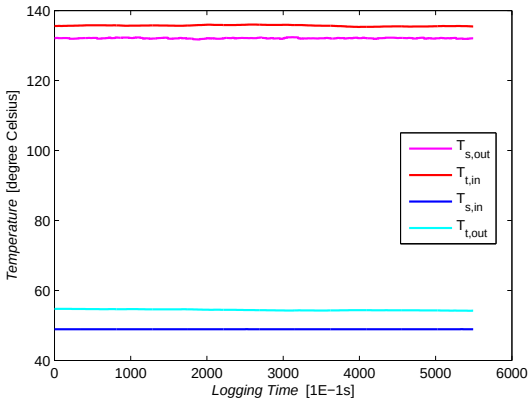

Figure 4.4: *Example data logging: in- and outlet temperatures of the heat exchanger*

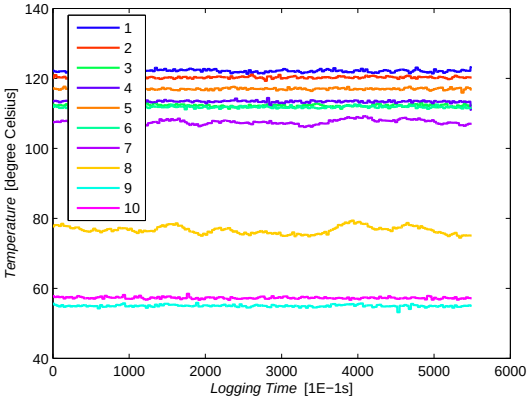

Figure 4.5: *Example data logging: temperatures along the shell*

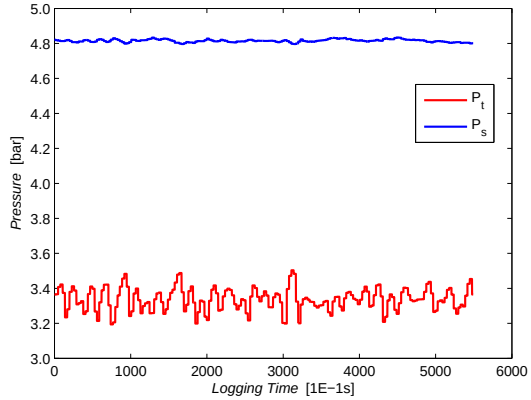

Figure 4.6: *Example data logging: pressure levels*

4.4. EXPERIMENTAL RESULTS

Three different sets of experiments are conducted. First both sides are filled with water, after that the water in the tube side is substituted by an ammonia–water mixture. Finally small amount of CO_2 is added to the tube side mixture.

4.4.1. WATER/WATER EXPERIMENTS

De-mineralized water (also known as 'demi water') is first fed into both sides of the system. In the previous study from Nefs [9], performance of the mini-channel with water has been investigated with identical mass flows on both shell and tube sides, the overall heat transfer coefficient is around 800 W/(m^2 K). For the current study, mass flow on the tube side is fixed at 10 kg/h, shell side mass flow is varied from 2.5 to 20 kg/h with an interval of 2.5 kg/h to figure out how the overall transfer coefficient is changing and the principles behind this change.

For the water/water experiment, the shell side inlet temperature is operated at around 60°C, which

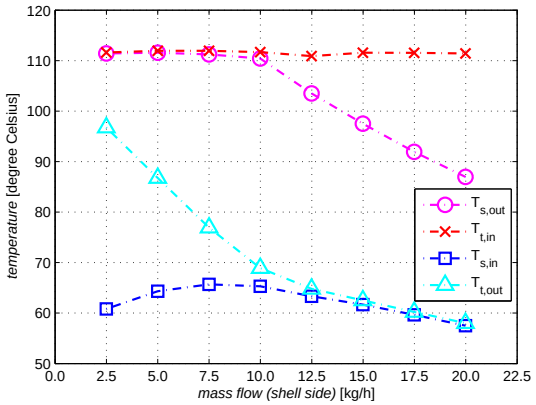

Figure 4.7: *Temperature profile for different shell side mass flows*

is the normal temperature of the spent cooling water in industrial processes [3], and the tube side inlet temperature is fixed at around 110°C, which is a commonly used high pressure hot water for district heating purposes. The temperature profile with different shell side mass flow conditions is demonstrated in Fig. 4.7. It can be observed that when the mass flows on both sides are identical (both are 10 kg/h), the heat exchanger performs the best, and this shell side mass flow is defined as the optimum mass flow when tube side mass flow is 10 kg/h. This is because the temperature differences on both top and bottom sides are small, thus it has the minimum logarithm mean temperature difference among all conditions, as shown in Fig. 4.8. Also this leads to the highest overall heat transfer coefficient, which can be seen from Fig. 4.9. The optimum overall heat transfer coefficient is around 800 W/m^2 K, the result is similar to Nefs' study [9].

From Fig. 4.7, it can be observed that when shell side mass flow is lower than the optimum mass flow, the hotter side temperatures are almost identical, while the colder side temperatures deviate from each other. This is due to the lack of mass flow on the shell side, therefore shell side is sufficiently heated, while part of the fluid on the tube side is not fully cooled. Opposite results are observed when shell side mass flow is larger than the optimum mass flow. This phenomenon indicates a method to determine the optimum condition: when the inlet temperatures and one side mass flow are fixed, the mass flow on the other side should be adjusted to achieve the optimum temperature profile. The method will be applied to the following experiments.

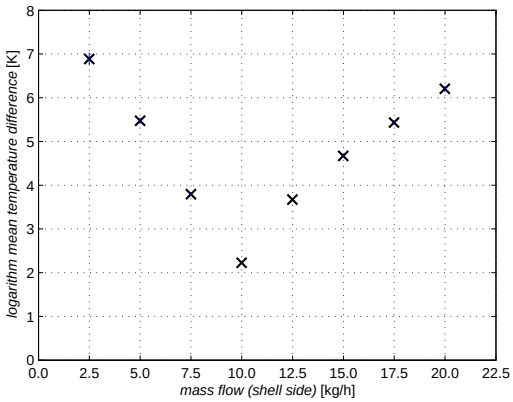

Figure 4.8: *Logarithm mean temperature difference for different shell side mass flows*

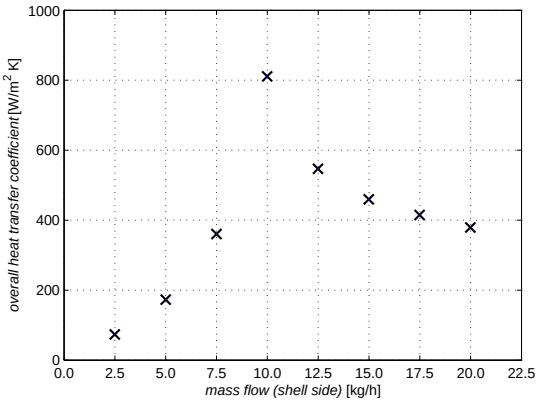

Figure 4.9: *Overall heat transfer coefficient for different shell side mass flows*

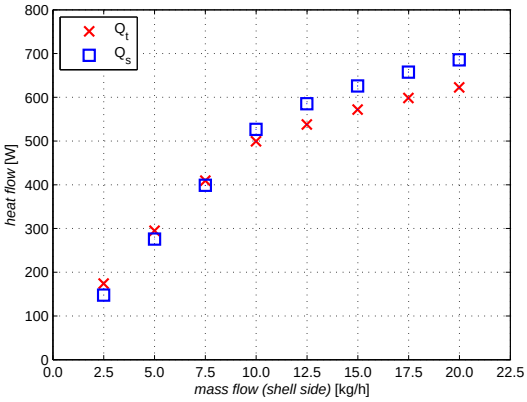

Figure 4.10: *Heat flow on both sides as a function of shell side mass flow*

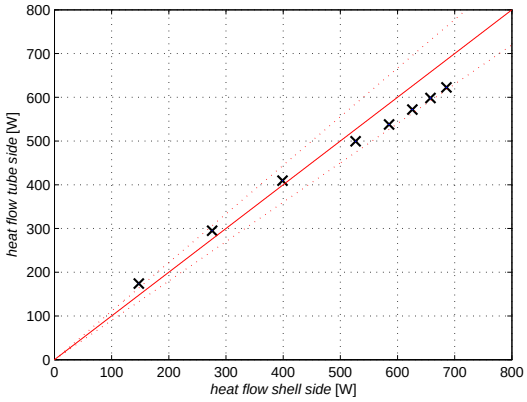

Figure 4.11: *Comparison of heat flows between shell side and tube side (error boundaries: ±10%)*

Fig. 4.10 shows the heat flow on both sides with the changing shell side mass flow. The heat flow is calculated by multiplying mass flow to its corresponding enthalpy difference between the in- and outlet. Ideally, if the mini-channel heat exchanger is perfectly insulated, there is no heat loss to the environment, thus Q_s and Q_t should be identical. While for the real case, there will be a small amount of heat flow released from the shell side to the environment due to temperature difference although it is insulated. Therefore Q_s should be a little lower than Q_t. The results shown in Fig. 4.10 and 4.11 indicate that when the shell side mass flow is higher than 10 kg/h, Q_s is higher than Q_t, which seems unreasonable. One possible explanation is that when the shell side mass flow is relatively high, vortex or disturbance may occur especially at the place near the shell outlet, where the distributor locates and the configuration is off regularity. The vortex causes backward flow for part of the fluid, instead of exiting the heat exchanger immediately, this amount of fluid stays at the shell side outlet for a while and gets over heated by the hot fluid on the tube side. This possible phenomenon leads to a higher enthalpy difference on the shell side. Fig. 4.11 indicates that the difference between the heat flows is quite small, which is within 10%.

4.4.2. AMMONIA–WATER/WATER EXPERIMENTS

Demi-water is replaced by ammonia–water binary mixture on the tube side after the water/water experiments. The total mass of ammonia–water mixture adding to the tube side cycle is crucial for the experiment, because it will determine the operating pressure, and it is not possible to predict this pressure level before heating up the system. Also inappropriate amount of total mass will cause unwanted inlet conditions on the tube side. After trial and error, van de Bor [27] summarized the experience from the previous experiments, and it is applied to the current experiments.

Approximately 1.300 kg demi-water and 0.655 kg ammonia are injected to the tube side cycle. Therefore the ammonia concentration is around 33.5% by mass. The ammonia–water mixture is completely mixed after several days pilot run, and the ammonia concentration can be validated with the experimental data. When in operation, the temperature and density values can be read from the flow meter, together with the pressure, the thermodynamic state at the local place where the flow meter is located can be determined, thus the ammonia concentration can be calculated. The calculated ammonia concentration is always around 33.5 wt%. Since it is difficult to determine the uncertainty of the ammonia concentration, therefore it is assumed to be constant for all the ammonia–water/water experiments.

The ideal operating condition is that the ammonia–water mixture enters the mini-channel in satu-

rated vapor condition, and leaves as saturated liquid. However it is not easy to accomplish in reality. The reason is that the hydrodynamic instabilities will cause unstable tube side operating pressure (as shown in Fig. 4.6), and it is impossible to adjust the temperatures with the changing pressure to achieve saturated vapor condition simultaneously. To make it operable, the tube side inlet temperature is fixed at a temperature higher than the corresponding local saturated vapor temperature. After some tests, this temperature is set at around 130°C. The advantage of setting the tube inlet at superheated condition is that the inlets of all tubes can have better homogeneity. Imagine the mixture entering the heat exchanger is in 2-phase condition, after the distributor, it is very possible that the tubes have very different inlet conditions and flow patterns. For the lower temperature side of the mini-channel, pilot running results show that when the outlet of the tube is in 2-phase state, the pressure measurement is quite unstable. It might be caused by the contraction and expansion of the unabsorbed vapor in the collector. Therefore it is better to cool down the ammonia–water mixture to a sub-cooled condition, and the shell side inlet temperature should be lower than ammonia–water saturated liquid temperature. After some tests, this temperature is set at around 50°C.

Experiments are performed with different mass flows. Shell side mass flow is investigated between 5 to 17.5 kg/h with an interval of 2.5 kg/h. The method mentioned in section 4.4.1 is applied to determine the corresponding optimum mass flow on the tube side. The temperature profile along the shell can also give an idea about when the optimum conditions are achieved. For example, when the shell side mass flow is 15 kg/h, the experimental results are shown in Fig. 4.12 and 4.13. From Fig. 4.13 it can be observed that when the tube side mass flow is around 2.2 kg/h, the whole condensation process is definitely within the mini-channel because the trend of the temperature near the in- and outlet is flat, which indicates that heat transfer at the two ends is weak and the tube side condition changes from superheated to sub-cooled. Compared to 2.2 kg/h, 2.1 is not sufficient and 2.3 is too high. Therefore the optimum tube side mass flow is around 2.2 kg/h when the shell side mass flow is 15 kg/h.

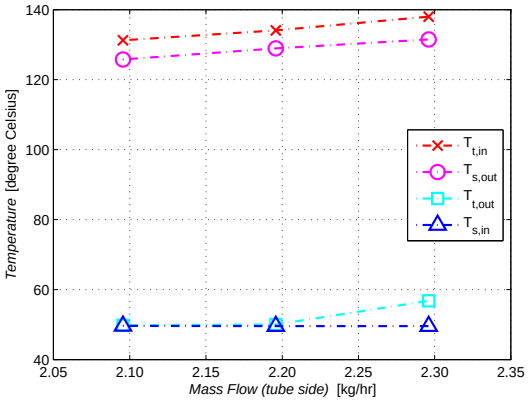

Figure 4.12: *In- and outlet temperature profiles when shell side mass flow is 15 kg/h*

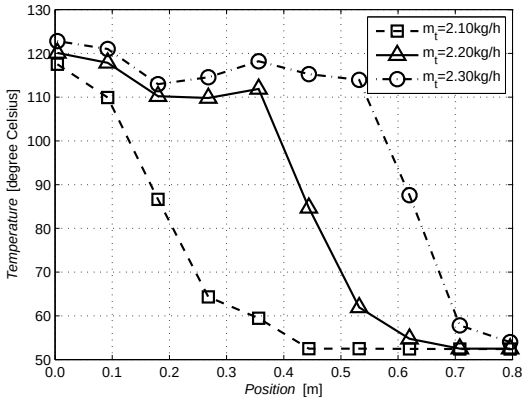

Figure 4.13: *Shell side temperature profiles when the shell side mass flow is 15 kg/h*

Corresponding optimum tube side mass flows can be determined for different shell side mass flows by applying the above mentioned rules. The results are illustrated in Fig. 4.14, they give a linear profile, the fitting curve can be expressed as:

$$\dot{m}_t = 0.1521 \cdot \dot{m}_s - 0.0708 \tag{4.23}$$

The heat load on both sides of the heat exchanger can be calculated by multiplying the mass flows to their corresponding enthalpy differences between the in- and outlet. The results from different

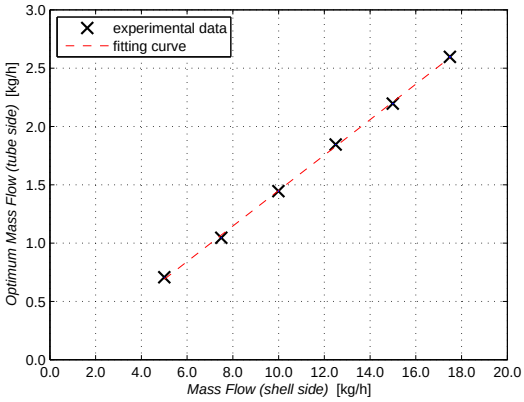

Figure 4.14: *Optimum tube side mass flow as a function of the shell side mass flow*

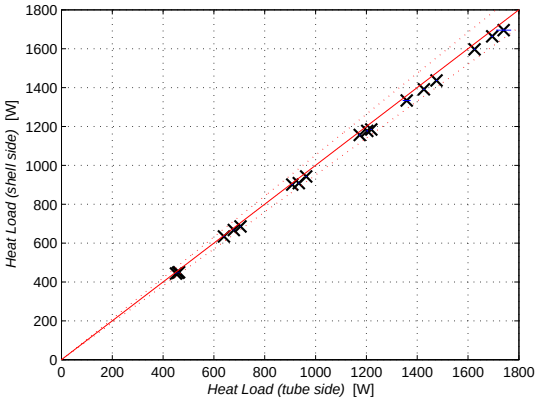

Figure 4.15: *Comparison of the heat loads between the shell and tube sides (error boundaries: ±5%)*

operating conditions are shown in Fig. 4.15. It is indicated that the tube side heat load is always slightly higher than that of the shell side. The results are reasonable since there is heat loss from the shell side to the environment. The difference between the heat load on two sides is within 5%, therefore it can be concluded that the shell side is well insulated.

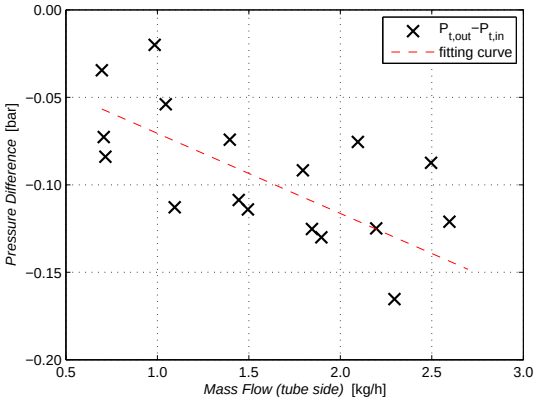

Figure 4.16: *Pressure drop as a function of mass flow on the tube side*

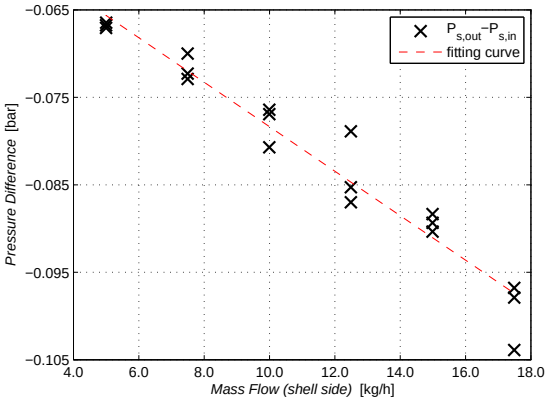

Figure 4.17: *Pressure drop as a function of mass flow on the shell side*

Pressures at the in- and outlets of the mini-channel can be determined based on the values obtained from the gauge and differential pressure sensors. The pressure differences on both the shell and tube sides are shown in Fig. 4.16 and 4.17. It can be observed that the pressure difference is higher when mass flow increases, this is reasonable because higher mass flow leads to higher friction loss, therefore the pressure difference is increased. The results in this section will be used to validate the theoretical model elaborated in chapter 3.

4.4.3. CO_2–NH_3–H_2O/WATER EXPERIMENTS

A small amount of CO_2 has been added to the tube side directly after the ammonia–water/water experiment to investigate its influence on the absorption process. The components on the tube side are listed in table 4.6.
In order to make the experimental data comparable, the inlet temperatures of those experiments are set to be identical to the ammonia–water/water experiment. The inlet temperature of the tube

Table 4.6: *Component detail in CO_2–NH_3–H_2O mixture*

Component	Mass	Mass Concentration
H_2O	1.300 kg	65.1%
NH_3	0.655 kg	32.8%
CO_2	0.042 kg	2.1%

side is set at around 130°C and that of the shell side is set at around 50°C. The tube side mass flow is adjusted until it reaches the optimum condition. One testing result for the optimum condition determination has been illustrated in Fig. 4.18 and 4.19. Shell side mass flow was fixed at 5 kg/h and tube side mass flow increased from 1.5 to 2.7 kg/h with an interval of 0.2 kg/h. It can be observed that when the tube side mass flow is at around 2.1 kg/h, the operating condition becomes the optimum, since the temperatures at the two ends are close to each other and the heat load on the shell side almost reaches its high limit.

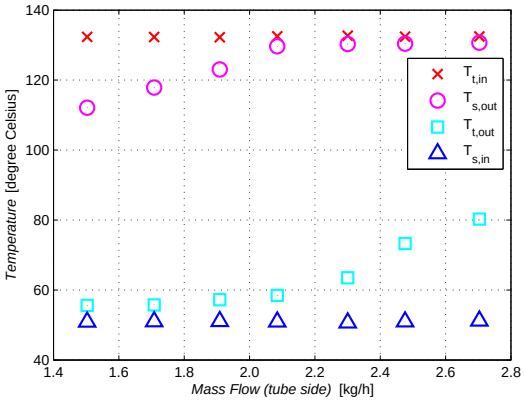

Figure 4.18: *In- and outlet temperature profiles with various tube side mass flow*

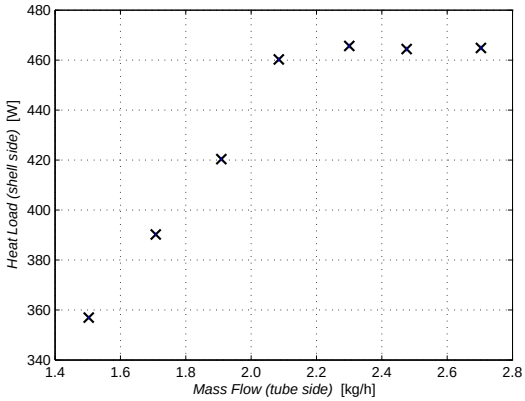

Figure 4.19: *Shell side heat load profile as a function of tube side mass flow*

The method which determines the optimum operating conditions stated in the ammonia–water/water experiments section has been applied to the current experiments. The experiments were supposed to investigate the shell side mass flow between 5 to 17.5 kg/h with an interval of 2.5 kg/h, while the results show that when the tube side mass flow is higher than 4.5 kg/h, temperatures and pressures cannot reach stable conditions, thus practical experimental data for the shell side mass flow higher than 10 kg/h are unavailable. The experiments show that after the carbon dioxide is added to the system, the mass flow on the tube side becomes less stable. The tube side mass flow has notable fluctuations with large amplitude. The large fluctuations show up with a random time interval, and the higher the tube side mass flow, the more frequent the fluctuations occur. This phenomena has not been observed in ammonia–water/water experiments. The instability might be caused by the unabsorbed CO_2 gas passing through the pump, or the CO_2 is desorbed at the pump. If this is the case it indicates that the carbon dioxide is easy to be desorbed from the mixture and that might be a problem in practical systems. Stable experimental results are only obtained with low mass flows. The results are compared with the ammonia–water experiment results, and they are shown in table 4.7, Fig. 4.20 and 4.21.

Table 4.7 compares the in- and outlet temperatures of the mini-channel between the ammonia–water/water and CO_2–NH_3–H_2O/water experiments in various optimum operating conditions. It can be observed that when the CO_2 is added, the temperature distributions at the two ends become worse since the logarithm mean temperature difference becomes larger. But it should also be

Table 4.7: *Temperature profile comparison*

Parameter	Unit	without CO_2/with CO_2	without CO_2/with CO_2	without CO_2/with CO_2
$\dot{m}_s$	[kg/h]	5.0/5.0	7.5/7.5	10.0/10.0
$T_{t,in}$	[°C]	132.00/132.46	130.99/131.36	135.35/134.30
$T_{s,out}$	[°C]	127.11/131.31	125.92/130.08	127.24/133.42
$T_{t,out}$	[°C]	50.69/58.51	49.91/58.43	50.24/54.75
$T_{s,in}$	[°C]	50.63/50.82	49.72/50.10	50.11/50.21
LMTD[1]	[K]	1.12/3.45	1.49/3.77	1.93/2.24

[1] LMTD is short for logarithm mean temperature difference

noticed that the CO_2–NH_3–H_2O/water experiment increases the shell side temperature to a higher level. Therefore the performance of the heat exchange on the shell side is enhanced by directly adding CO_2 on the tube side.

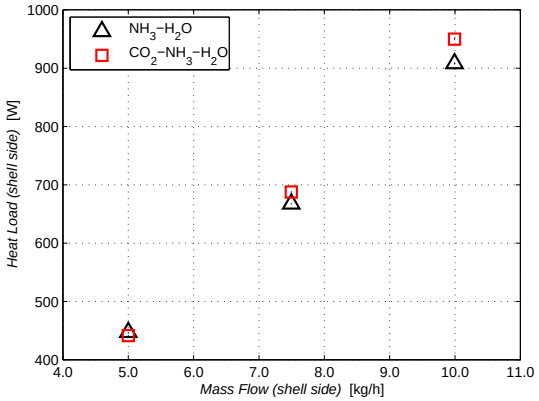

Figure 4.20: *Shell side heat load comparison*

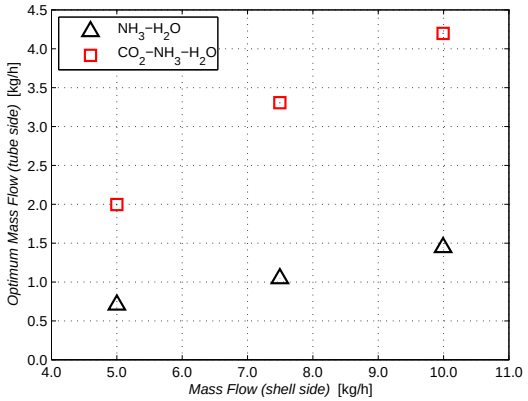

Figure 4.21: *Optimum tube side mass flow comparison*

Fig. 4.20 shows the comparison of the shell side heat load between ammonia–water/water and CO_2–NH_3–H_2O–water/water experiments. When in optimum operating conditions, the heat loads on the shell side are similar (adding CO_2 improves a little bit as stated in the last paragraph but not phenomenal), while the corresponding optimum tube side mass flows for the CO_2–NH_3–H_2O/water experiment are much higher than those of the ammonia–water/water experiment, as can be observed from Fig. 4.21. This is not a promising result since it indicates that to achieve the same amount of exchanged heat, higher CO_2–NH_3–H_2O mass flow is needed, therefore more external work is needed for the compressor and lower COP will be achieved. Further investigation indicates that the higher optimum tube side mass flow is due to the higher operating pressure compared to that of the ammonia–water/water experiments.

The operating pressure can influence the vapor quality of the CO_2–NH_3–H_2O mixture. As can be seen in Fig. 4.22 (data are collected using the new fit model from Gudjonsdottir and Infante Ferreira [7]), for a CO_2–NH_3–H_2O mixture with the compositions as shown in table 4.6, at the temperature 132.5°C (typical tube side inlet temperature for the current experiment), the increasing pressure will dramatically lower down the vapor quality at certain pressure range. This is the fundamental cause of the higher optimum tube side mass flow as stated in the previous paragraph. The higher pressure causes lower vapor quality and specific enthalpy, thus reduces the enthalpy difference between the in- and outlet of the tube and leads to a higher tube side mass flow. The comparison of tube side pressure levels between ammonia–water/water and CO_2–NH_3–H_2O/water experiments is shown in

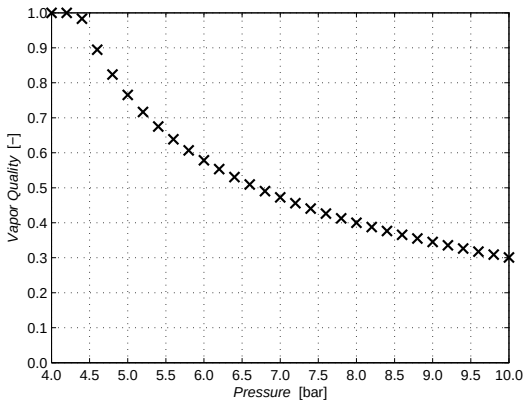

Figure 4.22: *Quality-pressure diagram for a CO_2–NH_3–H_2O mixture*

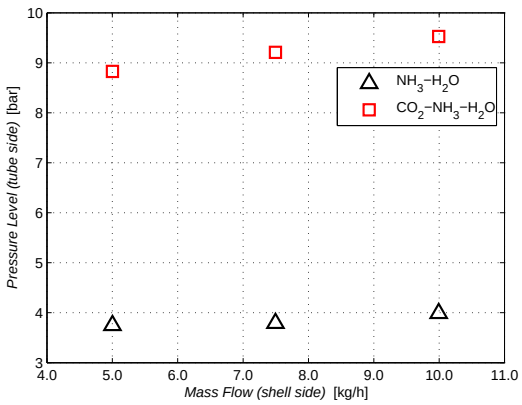

Figure 4.23: *Tube side pressure level comparison between two sets of experiments*

Fig. 4.23. The pressure level for the CO_2–NH_3–H_2O/water experiment is much higher, and it is not adjustable due to the setup configuration. Technically the setup cycle on the tube side (as shown in Fig. 4.1) is a thermal cycle without pressure control (the pumps can only compensate the pressure drop through the cycle). The operating pressure on the tube side can vary a lot among different operating conditions and it is not predictable. For the CO_2–NH_3–H_2O/water experiment, the mixture at the tube inlet is in 2-phase condition with a vapor quality of 30 to 40 percent (calculated using the new fit thermodynamic model for CO_2–NH_3–H_2O [7] conducted in Aspen Plus). To increase the quality with the current temperature profile, lower pressure level should be achieved.

The criterion to compare the performance of the two working fluids in the resorber of a CRHP cycle is reaffirmed here: in order to make the two sets (with and without CO_2 added) of the experiments comparable, the inlet temperatures of the heat exchanger, the shell side heat load, the shell side mass flow, and the operating pressure level should be identical. Therefore compare the optimum mass flow on the tube side, the lower it is, the less external power is needed (assume similar isentropic efficiency and pressure ratio for the compressors), and the higher COP of the heat pump can be obtained.

One feasible method to decrease the pressure level on the tube side is to drain some amount of the working fluid from the cycle. This is done when the whole setup was off and cooled down to the environment temperature, then pumped around for a couple of hours to get homogeneous mixture throughout the cycle. The reason is that if the fluid in the tube cycle is not isothermal, the ammonia concentration is not necessary to be homogeneously distributed. Therefore after draining some fluid at a certain vent, the composition of the working fluid will change and it is difficult to estimate the new composition in the system. The drawback of draining under the environmental temperature is that it is hard to estimate if the draining is sufficient enough so that when in operation the pressure level of the CO_2–NH_3–H_2O is identical to that of the ammonia–water/water experiment. Therefore it needs trial and error to achieve this goal. For the current experiment it was drained three times in total and the results for the first two times are shown in table 4.8, Fig. 4.24 and 4.25.

It can be observed from table 4.8 that the tube side inlet temperatures are set almost identical, the results show an increasing trend of vapor quality after two times draining, as expected. Fig. 4.24 is the tube side pressure level plotted based on the data in table 4.8. It is obvious that after some fluid is drained on the tube side, the pressure is decreasing. Corresponding shell side heat load profile is illustrated in Fig. 4.25. When operated in optimum condition, the shell side heat load is around 450

Table 4.8: *Experimental data comparison among different draining conditions*

$\dot{m}_s$ [kg/h]	$\dot{m}_t$ [kg/h]	$T_{t,in}$ [°C] O/F/S[2]	$P_{t,in}$ [bar] O/F/S	$q_{t,in}$[1] [–] O/F/S
5.0	0.7	132.46/132.57/132.83	7.42/6.96/5.72	0.44/0.48/0.63
5.0	1.5	132.36/132.91/132.72	8.58/7.65/6.55	0.37/0.43/0.52
5.0	1.7	132.31/132.77/–	8.75/7.66/–	0.36/0.43/–

[1] The vapor quality is determined using the new fit model from Gudjonsdottir and Infante Ferreira [7];
[2] 'O' denotes the original experiments with no draining; 'F' denotes the experiments after the first draining; 'S' denotes the experiments after the second draining.

W, and for the ammonia–water/water experiments the optimum tube mass flow is around 0.7 kg/h. It can be observed that for the CO_2–NH_3–H_2O/water experiment without draining, the optimum tube mass flow is higher than 1.7 kg/h; after the first time extraction, the optimum tube mass flow was lowered down to 1.7 kg/h; after the second time extraction, the optimum tube mass flow further decreased to lower than 1.4 kg/h. This result indicates that lowering tube side pressure level will decrease the optimum tube side mass flow as predicted. Tube side working fluid should be further drained to reach the same pressure level as that of the ammonia–water experiment, and therefore by comparison of the optimum tube side mass flow, better working fluid can be determined. Unfortunately after the third time extraction, the operation became very unstable. The temperatures and pressures have fluctuations with large amplitudes and low frequencies, therefore the logged data are difficult to be properly analyzed. The cause of this instability might be the poor distribution of the tube side flow due to the structure of the heat exchanger.

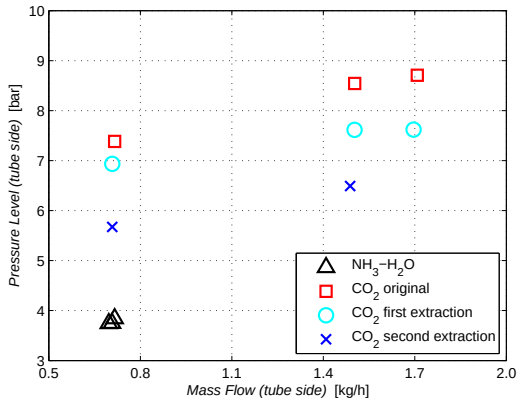

Figure 4.24: *Shell side heat load comparison when shell side mass flow is 5 kg/h*

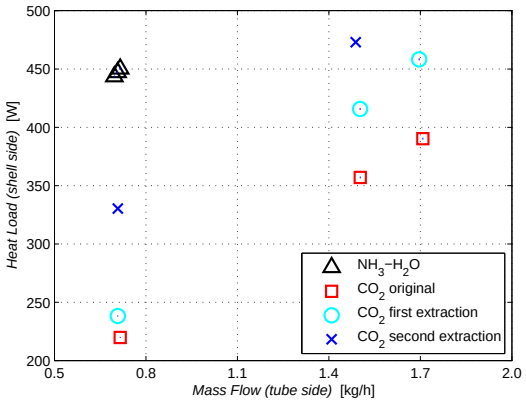

Figure 4.25: *Optimum tube side mass flow comparison when shell side mass flow is 5 kg/h*

To further test the cause of the instability, experiments with opposite flow directions are performed: the CO_2–NH_3–H_2O mixture flows upwards on the tube side, and the cooling water flows downwards on the shell side. The experimental results show that the operating conditions are quite stable and steady experimental data can be obtained. This indicates that the configuration of the heat exchanger and the flow direction can influence the operating stability. The upward flow on tube side (absorption side) leads to a stabler flow condition compared to a downward flow. However the heat flow performance on the water side becomes worse when operated in optimum condition due to the lower shell outlet temperature. This is listed in table 4.9.

Table 4.9: *Shell side heat flow performance comparison*

$\dot{m}_s$ [kg/h]	$\dot{m}_{t,opt}$ [kg/h] A/B/C[1]	$\dot{Q}_w$ [W] A/B/C
5.0	0.71/2.00/1.20	447/448/418
7.5	1.05/3.30/1.80	668/688/615
10.0	1.40/4.20/2.40	901/950/888

[1] 'A' represents the ammonia–water/water experiments; 'B' represents the CO_2–NH_3–H_2O/water experiments with downward flow on the tube side; 'C' represents the CO_2–NH_3–H_2O/water experiments with upward flow on the tube side.

4.5. DISCUSSION AND CONCLUSIONS

Three sets of experiments with different working fluids on the tube side are introduced and the experimental results are shown in this chapter. The water/water experiments include several tests which determine the optimum operating condition when the inlet temperatures are fixed. Results illustrate that when in optimum operating condition, the temperatures at the two ends of the heat exchanger are well distributed, the logarithm mean temperature difference reaches the lowest value and has the best heat transfer performance. Analysis shows that the heat exchanger is well insulated and the heat loads on both sides are comparable.

Ammonia–water/water experiments were conducted afterwards. To obtain stabilized experimental results, the tube inlet was operated in a superheated condition and the outlet was operated in a subcooled condition. Results show fluctuations on the tube side pressure data, most of the fluctuations are regular when the temperature profiles are steady. These fluctuations might be caused by hydrodynamic instability due to the configuration of the heat exchanger. The fluctuations of the pressure also lead to a dispersed distribution of pressure drops on the tube side as shown in Fig. 4.16.

Results from the CO_2–NH_3–H_2O/water experiments indicate that adding small amounts of CO_2 directly to the system will have a dramatic increase of the pressure when the system is operated at high temperatures. When operated in the optimum condition, the shell side heat flow is a bit higher than that of the ammonia–water/water experiments. Experiments show that the operating conditions are much less stable after small amount of carbon dioxide is added to the tube side. The tube side mass flow fluctuates with large amplitude when operated in higher values. Experimental results with the opposite flow direction indicate that the instability might be caused by the configuration of the heat exchanger (e.g. the design of the distributors). The operating condition becomes much more stable when the mass flows are of the opposite directions. Further investigation should be done to determine if the CO_2–NH_3–H_2O mixture is suitable for practical use in CRHP and to conclude whether it has better performance than the ammonia–water mixture.

5

Model Validation and Discussion

5.1. Validation for the Ammonia–Water Theoretical Model

5.1.1. Example Results for the 2-phase Model in Chapter 3

The numerical model described in Chapter 3 is first qualitatively validated with reasonable data. For example, the thermodynamic parameters listed in table 5.1 are given as the inputs. These data are based on the experimental results, the tube side inlet temperature is lowered down a little bit to ensure a 2-phase condition for the mixture.

Table 5.1: *Inputs for the 2-phase model example*

Parameter	Unit	Value	Description
$T_{t,in}$	[°C]	130.5	tube side inlet temperature
$P_{t,in}$	[bar]	4.32	tube side inlet pressure
w_{NH_3}	[kg/kg]	35.9%	ammonia mass concentration
$\dot{m}_t$	[kg/h]	1.84	tube side mass flow
$T_{cw,out}$	[°C]	128.6	shell side outlet temperature
$P_{cw,out}$	[bar]	5.30	shell side outlet pressure
$\dot{m}_{cw}$	[kg/h]	12.49	shell side mass flow

Together with the geometry of the mini-channel heat exchanger mentioned in table 4.1 and the grid arrangement of the control volumes, the model can be sufficiently initialized. Fig. 5.1 shows the cell grid arrangement of the heat exchanger along the axis direction from top to bottom for the current example. Instead of an even distribution (which then should be a straight line), the sinuous curve indicates that the control volumes are smaller at the two ends of the heat exchanger and larger in between, as shown in Fig. 5.2. This is due to the difficulty of determining ammonia molar flux ratio z and the interface temperature when the quality approaches 0 or 1. Inappropriate control volume size will cause larger errors for the z value and the interface temperature, and it will finally result in failure of calculation for the following control volumes. The sinuous distribution guarantees high calculating precision at the two ends and high calculating speed in between. The total number of the control volumes for this example is 4000 which is the minimum possible value, lower number will cause error due to less accurate prediction of the flux ratio z and the simulation cannot process further, while higher number will take more time to process. Tests showed that the grid arrangement with smaller control volume distribution had similar results with the current cell grid arrangement.

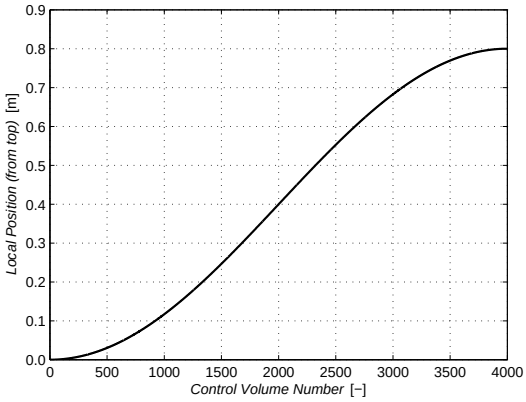

Figure 5.1: *Example result: cell grid arrangement of the heat exchanger*

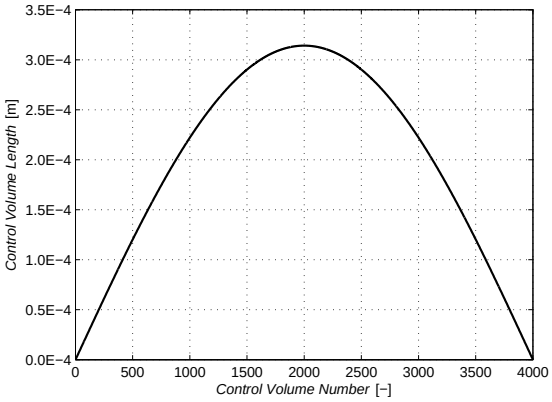

Figure 5.2: *Example result: control volume length profile*

The calculation started from the top side of the heat exchanger and finally the profiles of different parameters along the heat exchanger length were obtained. Some of the simulation results are illustrated in the following paragraphs.

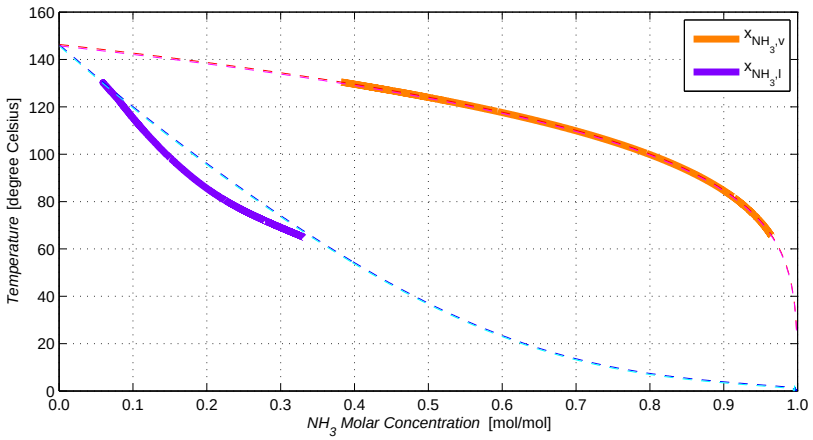

Figure 5.3: *Example result: T–x diagram*

The absorption process within the heat exchanger is illustrated in a temperature–concentration diagram in Fig. 5.3. The simulation result is similar to what has been predicted in section 3.1 (see Fig. 3.2). The absorption process starts from the 2-phase region, and the mixture temperature decreases from around 130°C to 65°C. It can be observed that the vapor always goes along the dew point curve, while the liquid goes below the bubble point curve. Due to the fact that there is no heat entering the vapor bulk flow, and the vapor keeps releasing heat and mass to the liquid bulk through the interface, the vapor can only stay in saturated condition but not superheated condition. For the liquid bulk, although receiving heat and mass from the vapor bulk, it keeps releasing heat to the cooling water side through the tube wall, therefore it is reasonable to be in the sub-cooled condition. At the tube outlet the ammonia–water mixture is still in 2-phase condition, since the liquid concentration does not reach the total concentration of the mixture.

Fig. 5.4 depicts the temperature profile along the length of the heat exchanger. The results show that at any local position, the temperatures always follow: $T_v > T_i > T_l > T_{wi} > T_{wo} > T_{cw}$, which is similar to what was expected in section 3.1 (see Fig. 3.3). The interface temperature is between

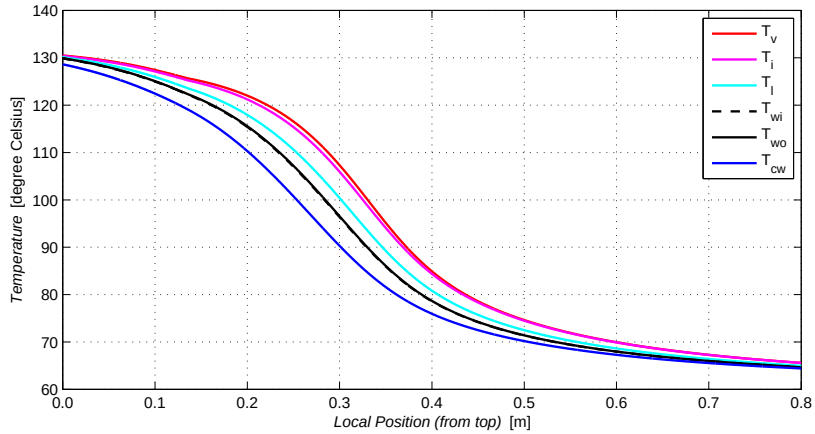

Figure 5.4: *Example result: temperature profile*

the vapor and liquid bulk temperatures, it is much closer and sometimes even identical to the vapor bulk temperature. It indicates that the thermal resistance between the interface and the vapor is much lower than that between the interface and the liquid. Thus for the simulation it is reasonable to assume that the thermal resistance on the vapor side can be neglected, as some researchers previously did. The temperature driving force among vapor, liquid, and cooling water becomes larger at the beginning and reaches maximum at around 0.3 m, then it becomes smaller till the bottom of the heat exchanger. It indicates that the heat and mass transfer are remarkable at the beginning, and attenuate gradually after the first half.

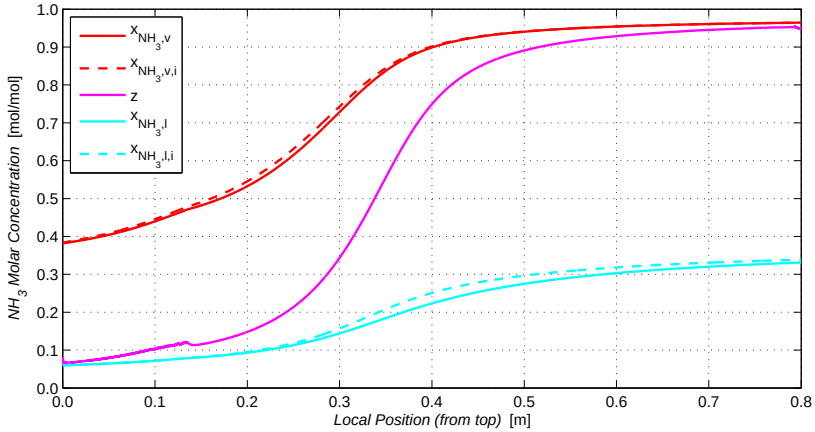

Figure 5.5: *Example result: NH_3 molar concentration profile*

The ammonia concentrations for different phases and the molar flux ratio z (defined in equation 3.2) profile along the heat exchanger is displayed in Fig. 5.5. The results show that the flux ratio z is always between the saturated liquid ammonia concentration at the interface ($x_{NH_3,l,i}$) and the vapor bulk ammonia concentration ($x_{NH_3,v}$). At the beginning it is close to the saturated liquid concentration and later moves to approach the vapor bulk concentration. This is a typical profile for condensers or absorbers, as stated in a previous study from Sieres and Fernández-Seara [33]. It can be observed that the vapor bulk ammonia concentration is lower than the saturated vapor ammonia concentration at the interface ($x_{NH_3,v,i}$). This is because both the interface and the vapor bulk are saturated, they are of the same pressure level while the vapor bulk has higher temperature, thus the ammonia concentration for the vapor bulk is higher. For the liquid phase, the liquid bulk is

sub-cooled, the results from the simulation shows that its ammonia concentration ($x_{NH_3,l}$) is always lower than that of the saturated liquid at the interface. The results are exactly the same as previously expected in section 3.5.1 (see Fig. 3.5).

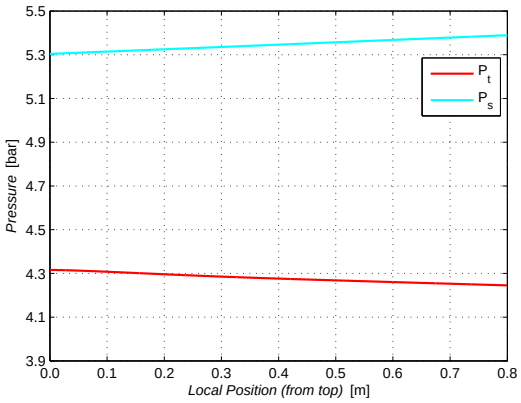

Figure 5.6: *Example result: pressure profile*

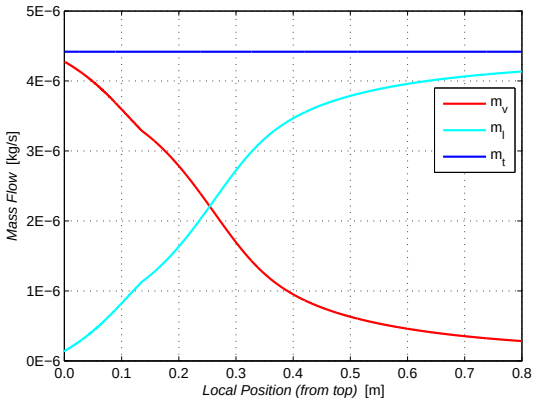

Figure 5.7: *Example result: tube side mass flow profile*

Fig. 5.6 shows the pressure level profile on both shell and tube side along the length of the heat exchanger. Pressure differences caused by friction and the height difference are taken into account within the simulation. Other causes such as contraction/expansion, and the inlet effect (e.g. distributors) are not taken into consideration. The result shows reasonable trend of the pressure: for the tube side, the fluid flows from the top to bottom, thus the pressure decreases along the heat exchanger from the top; on the other hand, the cooling water flows from the bottom to top, then the pressure has the opposite trend compared to the tube side. From the simulation results it can be figured out that the pressure difference between the in- and outlet on both sides are small, or within 0.1 bar.

Vapor and liquid mass flows in one single tube along the length of the heat exchanger is illustrated in Fig. 5.7. The blue horizontal line is the sum of the two flows, and it is always constant because there is no additional mass flow entering or leaving along the tube. The results show that the vapor is absorbed into the liquid quickly at the beginning, and then slows down after around 0.5 m. Possible reasons will be discussed in the following sections.

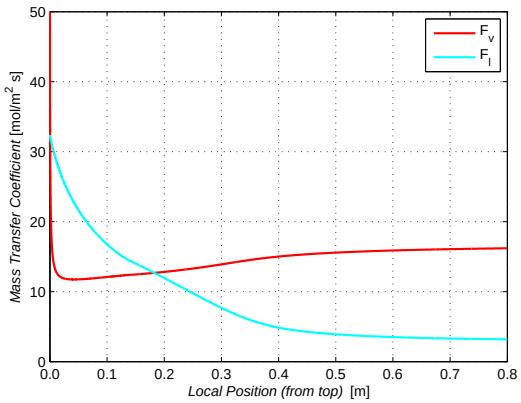

Figure 5.8: *Example result: mass transfer coefficient profile*

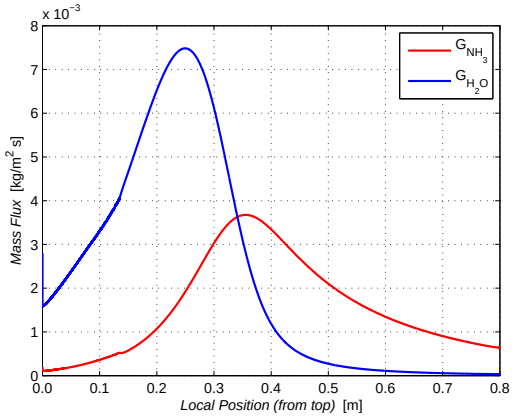

Figure 5.9: *Example result: mass flux through the interface*

Fig. 5.8 and 5.9 show the mass transfer coefficients and the mass fluxes through the interface along the heat exchanger, respectively. The mass transfer coefficients are influenced by the convective dif-

fusion rate constant which is determined based on heat and mass transfer analogy, as mentioned in section 3.5.1. The results show that the mass transfer coefficient for the vapor is around 15 mol/m^2 s and does not change much along the heat exchanger, while for the liquid it drops from 30 to around 4 mol/m^2 s. The profile for mass transfer coefficient is abstract and it is hard to verify its correctness by common sense. Therefore the mass fluxes for different components passing through the interface are depicted in Fig. 5.9. It can be observed that the water mass flux is much larger than the ammonia mass flux at the beginning, it quickly reaches the maximum and then drops since most of the water has been condensed. Compared to the water, the ammonia mass flux is small at first, it reaches maximum later and continuously is being absorbed with notable flux. The results indicate that through this condensation/absorption process, most of the water vapor is quickly condensed and ammonia vapor is gradually absorbed into the liquid solution. This is reasonable because ammonia is more volatile than water, thus at the same temperature and pressure, ammonia is more reluctant to be condensed. It is also notable from the figure that the general flux level of water is higher than that of ammonia, this is because the ammonia mass concentration is lower than that of the water, thus the average mass flux for the water should be higher.

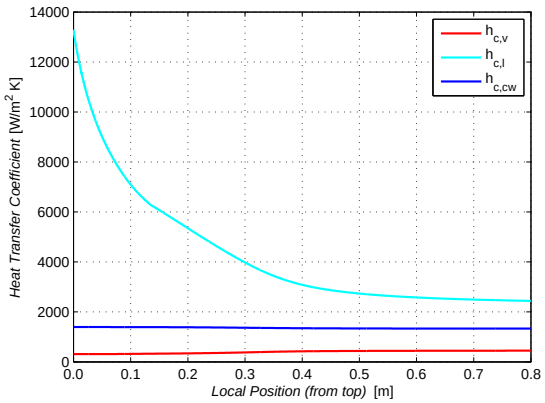

Figure 5.10: *Example result: heat transfer coefficient profile*

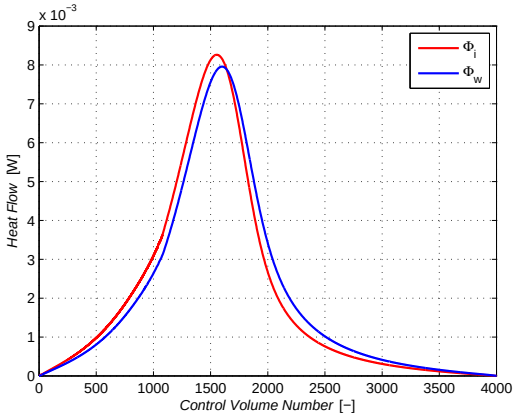

Figure 5.11: *Example result: heat flow profile*

The convective heat transfer coefficients for the vapor bulk, liquid bulk, and the cooling water along the heat exchanger are illustrated in Fig. 5.10. The convective heat transfer coefficient for a certain fluid (h_c) is determined using equation 3.30, it is influenced by the Nusselt number, the thermal conductivity and the hydraulic diameter. Simulation result shows that the thermal conductivity for single-phase fluids (vapor mixture, liquid mixture, and cooling water) vary little along the heat exchanger. Also due to the low mass flows on both sides, all the flows are laminar, thus the Nusselt numbers are small constant. The hydraulic diameter of the liquid bulk increases notably at the first half of the heat exchanger and then becomes stable (see Fig. 5.15), therefore the convective heat transfer coefficient for the liquid bulk drops dramatically at the beginning from 13000 to around 3000 W/m^2 K and then stabilizes. For the vapor bulk and the cooling water, since their hydraulic diameters do not change much, their convective heat transfer coefficients are quite stable along the heat exchanger as can be observed in Fig. 5.10.

Fig. 5.11 shows the heat flow through the interface and the tube wall for all control volumes. The heat transferred through the interface consists of the explicit heat transfer driven by the temperature difference and the mass transfer based heat. The simulation result indicates that the explicit heat transfer is so small compared to the mass transfer based heat that it can be neglected. Therefore it is reasonable to say that the heat transfer is highly influenced by mass transfer phenomena, it can be proved by comparing Fig. 5.11 with Fig. 5.9, since they have similar profiles. It can be observed

from Fig. 5.11 that the heat flows through the interface and the tube wall are analogous and the magnitudes are comparable. At the beginning the heat flow through the interface is a bit higher than that through the tube wall, at the same time large amount of water and small amount of ammonia is passing through the interface from the vapor to the liquid bulk. These phenomena make the liquid film further sub-cooled as can be observed from Fig. 5.3. While after the peak, the mass transfer becomes less intense, at the same time the heat transfer through the interface is lower than that through the tube wall. This leads to the fact that the liquid approaches the bubble point curve.

Local logarithm mean temperature difference (LMTD) can be calculated using equation 4.13 when local temperature profiles are known, the result is depicted in Fig. 5.12. The value quickly increases from the top side of the heat exchanger and reaches maximum at around 0.3 m, and then keeps decreasing till the other side of the heat exchanger. This trend can be explained with the help of the temperature profile in Fig. 5.4. The temperature difference between both sides is small at the beginning, and becomes much larger with an increasing speed till it reaches a maximum at around 0.3 m of the heat exchanger length. After that the temperature difference decreases, with a high speed at the beginning and then slows down when the temperature difference is small.

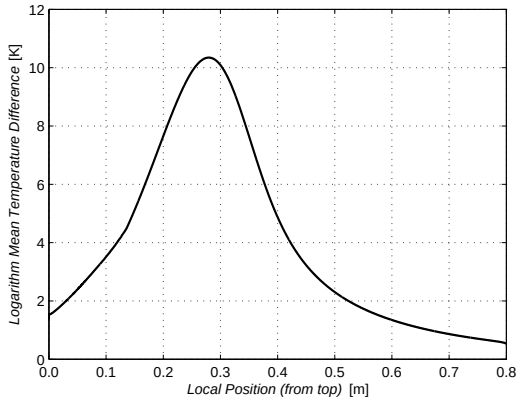

Figure 5.12: *Example result: logarithm mean temperature difference profile*

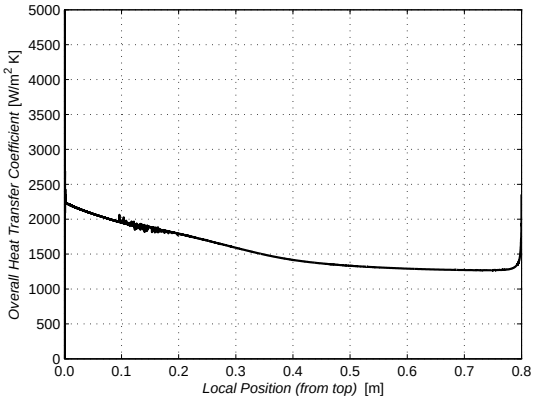

Figure 5.13: *Example result: overall heat transfer coefficient profile*

Fig. 5.13 illustrates the local overall heat transfer coefficient profile, it is determined by equation 4.19. The result shows that its value does not vary a lot through the whole heat transfer process along the heat exchanger. The mean value for the current operating condition is around 1500 W/m^2 K.

Generally the 2-phase model can give reasonable results as stated above. The model is qualitatively validated with success since most of the phenomena it predicts are explainable. But also there are some drawbacks which will be discussed in the following section, and the model should be further validated quantitatively with experimental results.

5.1.2. DISCUSSION FOR THE 2-PHASE MODEL

The inputs for the example of the model mentioned in table 5.1 are the modified ones from the experimental data. Because the model cannot start calculation with superheated conditions on the tube side. For the experiment, the tube inlet is set in superheated condition while the outlet is in sub-cooled condition. The current 2-phase model is not able to predict the performance of the heat exchanger in these two conditions. Therefore the model should be extended to cover operating

conditions when the ammonia–water mixture is in superheated and sub-cooled conditions. With these extensions the model can be sufficiently validated with the experimental data.

Another problem for the current 2-phase model is that based on the experimental data, the outlet condition for the tube side has already been sub-cooled, while based on the simulation result, it is still in the 2-phase region. One possible cause is discussed in the following paragraphs.

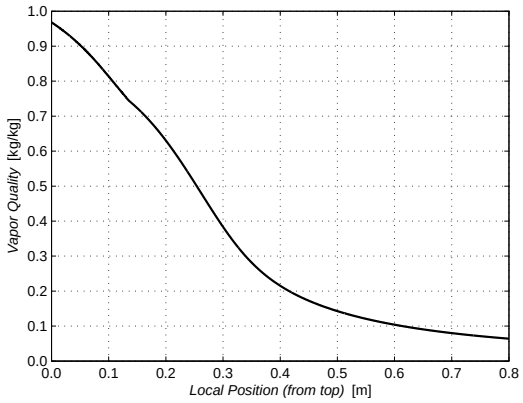

Figure 5.14: *Example result: vapor quality profile*

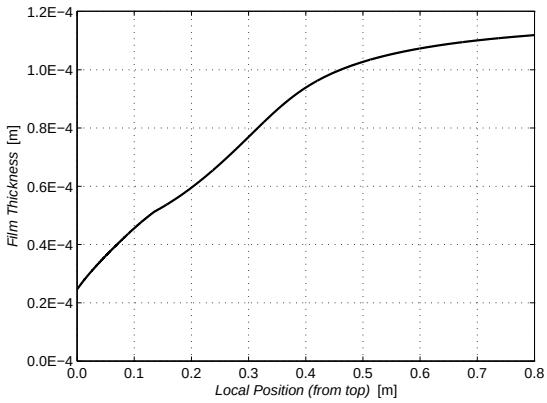

Figure 5.15: *Example result: film thickness profile*

Fig. 5.14 depicts the vapor quality on the tube side along the heat exchanger. It can be observed that the quality drops with a stable speed at the beginning. When the quality reaches around 0.2 to 0.15, the decrease becomes much slower thus the curve becomes much flatter. It indicates that the mass transfer from the vapor to the liquid becomes weaker, which can be verified by Fig. 5.9. The film thickness profile along the heat exchanger is illustrated in Fig. 5.15. The result shows that within the first 0.5 m from the top of the heat exchanger, the film thickness follows a stable increase. While after that, the increase slows down and the curve becomes much flatter. It is notable that at the tube outlet, the quality is almost zero, while the film thickness is still far smaller than half of the tube inner diameter (when fully absorbed, the film thickness should equal to half of the inner diameter which is 0.25 mm).

The discussion above indicates that the model cannot well predict the film thickness and the mass transfer phenomenon when the quality becomes low. Recall the method that determines the film thickness in section 3.5.2, the equations are derived from the Nusselt theory for falling films. Technically when the falling film is stable inside the tube, the flow pattern for this 2-phase mixture is annular flow. In reality, with the decrease of quality and the changing of superficial velocities of the vapor and liquid, the flow pattern will transit from annular to churn, slug, or bubbly flow. Such transition will enhance both the heat and mass transfer and speed up the pace of absorption and condensation. When the flow pattern changes, the current equations determining the film thickness are no longer valid, also different empirical equations and analogies should be applied to define the momentum, heat and mass transfer. Normally empirical flow pattern maps are used to determine flow patterns. Unfortunately seldom studies mentioned 2-phase downward flow in mini size tubes, especially with an ammonia–water mixture. Also various experimental studies conclude that most flow pattern maps can give reasonable predictions only with specific experimental conditions [45]. Therefore for the current study, the performance of the heat exchanger with flow patterns other than annular flow is not taken into consideration. Instead, reasonable assumption based on the former simulation results is applied. Based on the simulation results for different operating conditions, it can be concluded that the vapor quality curve becomes flatter when the quality reaches between

0.15 to 0.2. Therefore to skip the modeling of other flow patterns, it is assumed that for the current 2-phase model, when the quality decreases to 0.1, that the ammonia–water mixture is transmitted into saturated liquid condition. This assumption will be further validated with the experimental data.

5.1.3. MODEL EXTENSION AND MODIFICATION

As discussed in the previous section, the theoretical model should be extended to cover operating conditions when the ammonia–water mixture is in superheated and sub-cooled states. These extensions are developed as sub models which are parallel to the 2-phase model described in Chapter 3. The sub models for superheated and sub-cooled tube side conditions are much simpler since there is no mass transfer within the single-phase flow.

Two Sub Models: Tube Side Superheated and Sub-cooled Regions

The assumptions declared in section 3.4 are also applied to the current sub models. For single-phase flows on both sides, heat and momentum transfers are taken into account. Thermodynamic and transport properties for both shell and tube sides are determined using same models as mentioned in chapter 3. The pressure drop and the heat transfer coefficient for the shell side are calculated using the same methods as described in sections 3.5.2 and 3.5.3. For the the pressure drop on the tube side, the method from the VDI Heat Atlas is used [35]. The pressure drop for the single-phase fluid in a circular pipe flow is given by:

$$\Delta P = \zeta \frac{l}{d_{ti}} \frac{\rho u^2}{2} \tag{5.1}$$

where ζ is the drag coefficient, its value depends on the Reynolds number for the flow within the tube. For laminar flow, when the Reynolds number is lower than 2300:

$$\zeta = \frac{64}{\mathrm{Re}} \tag{5.2}$$

For fully turbulent flow when the Reynolds number is between 3000 to 100000, Blasius equation can be applied to determine the drag coefficient:

$$\zeta = \frac{0.3164}{\sqrt[4]{\mathrm{Re}}} \tag{5.3}$$

When the Reynolds number is in between these two conditions, the drag coefficient can be expressed as:

$$\zeta = \gamma \cdot \zeta_{2300} + (1-\gamma) \cdot \zeta_{3000} \tag{5.4}$$

where

$$\zeta_{2300} = \frac{64}{3000} \tag{5.5}$$

$$\zeta_{3000} = \frac{0.3164}{\sqrt[4]{3000}} \tag{5.6}$$

$$\gamma = \frac{3000 - \mathrm{Re}}{3000 - 2300} \tag{5.7}$$

For the current study the mass flux is quite low, the Reynolds number for the vapor cannot reach higher than 10000. Therefore conditions for drag coefficient with higher Reynolds number are not introduced.

The heat transfer coefficients on the tube side can be determined by applying equations 3.30 to 3.36 mentioned in section 3.5.3. With both shell and tube side heat transfer coefficients known, the heat transfered from the vapor to the shell through the tube wall can be determined using equation 3.39. Finally the output thermodynamic properties can be calculated by applying simple momentum, mass and energy balances to the control volume on both sides. The flow sheet for this certain sub model is illustrated in Fig. 5.16. When the output quality for the control volume is lower than 1, the calculation with this sub model stops and the sub model for 2-phase conditions on the tube side starts.

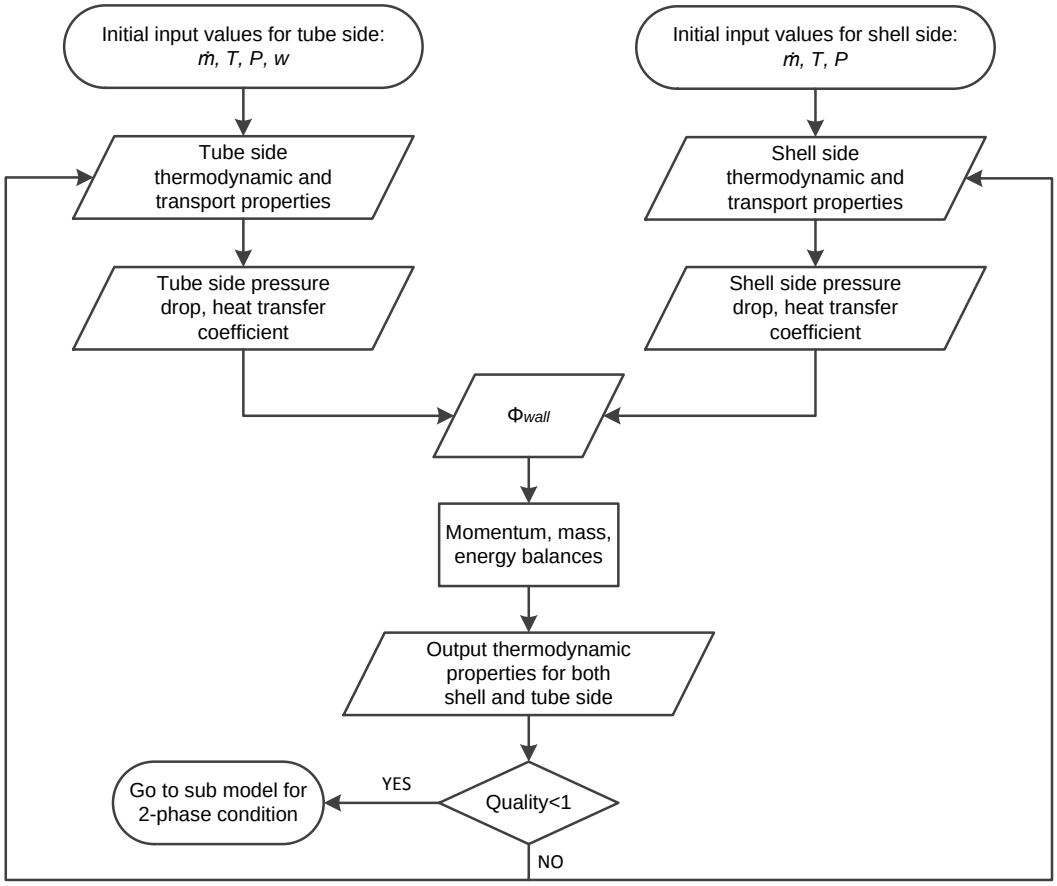

Figure 5.16: *Flow sheet of the sub model when tube side is in superheated condition*

The tube side sub-cooled model is built in the same way as the superheated condition sub model mentioned above.

Other Modifications

A relatively comprehensive model has been developed by combining the three sub models (tube side superheated, 2-phase, and sub-cooled). Input vapor quality is the key parameter to determine which sub model to use. As discussed in section 5.1.2, when the quality drops below 0.1, the tube side is considered to be in the sub-cooled region. A simplified flow diagram for the whole model is depicted in Fig. 5.17.

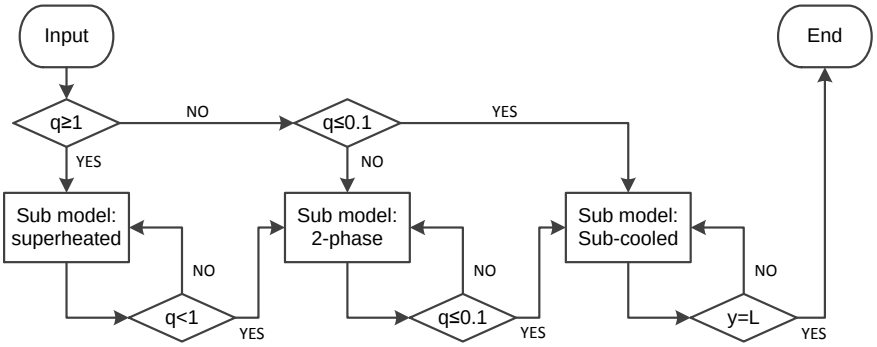

Figure 5.17: *Simple flow sheet of the modified model*

The input thermodynamic properties are first evaluated. If the quality is higher than one, the simulation starts from the superheated sub model; if the quality is between 0.1 to 1, it starts from the 2-phase sub model; otherwise it starts directly from the sub-cooled sub model. Each time when the calculation for one control volume is finished, the output quality would be evaluated to decide whether the next control volume should be calculated within the same sub model or the next one, as illustrated in Fig. 5.17. Notice that when switching from the 2-phase sub model to the sub-cooled sub model, the quality directly changes from $q = 0.1$ to saturated liquid ($q = 0$), the energy drop caused by this sudden transition should be taken into account. The pressure drop during this transition is neglected, and this amount of energy can be calculated by:

$$\Phi_{transition} = \dot{m}_v \cdot h(T,P,q=1) + \dot{m}_l \cdot h(T,P,q=0) - \dot{m}_t \cdot h(P,w,q=0) \tag{5.8}$$

This amount of energy is also added to the cooling water side in order to determine the shell side input entering the sub-cooled model. The simulation finally ends when the calculation covers the whole heat exchange area of the heat exchanger.

5.1.4. RESULTS AFTER MODIFICATION

Shell Side Temperature Profile

After the modification stated above, tests with experimental data have been done to check the validity of the model. Notable errors appear from the first several control volumes in the 2-phase sub model and the simulation cannot process further. Investigation on the results show that when the 2-phase sub model starts with saturated vapor condition or with a high vapor quality, accurate suitable mass flux ratio z cannot be obtained since the mass balance at the interface (see equation 3.6) is difficult to fulfill with iterations. Therefore the errors for the parameters z and T_i become huge and have negative influence on the following calculations. The cause of this problem might be due to the inner instability of the computation in Matlab caused by the structure of the codings, or the software cannot precisely predict the physical properties of the ammonia–water mixture when the quality is approaching unity.

Results from trial and errors indicate that the 2-phase sub model can perform well when the input quality is not higher than 0.97. To make the model work and to validate the 2-phase sub model with the experimental data, currently it is assumed that when the ammonia–water reaches saturated vapor state after processing in the superheated sub model, it enters the 2-phase sub model directly

with the quality of 0.97. The energy drop in between is calculated and added to the total transfered heat. The pressure drop in between is neglected, and this amount of energy can be determined by:

$$\Phi_{transition} = \dot{m}_t \cdot h(T, P, w) - \dot{m}_t \cdot h(P, w, q = 0.97) \tag{5.9}$$

This amount of energy is added to the cooling water side to determine the shell side input entering the 2-phase sub model. One efficient way to validate the performance of the model is to compare the cooling water temperature profile from the simulation to the experimental data obtained by the temperature sensors along the shell of the heat exchanger (see Fig. 4.1). Some of the results are shown in Fig. 5.18.

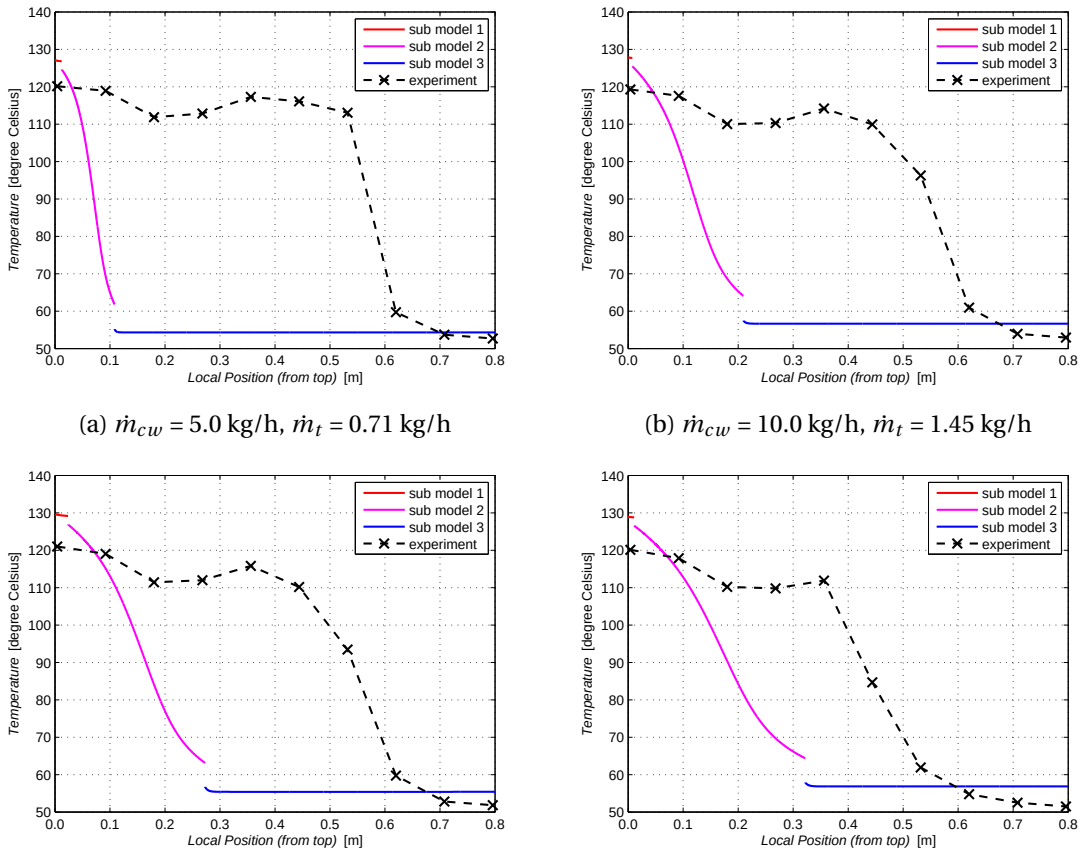

(a) $\dot{m}_{cw} = 5.0$ kg/h, $\dot{m}_t = 0.71$ kg/h

(b) $\dot{m}_{cw} = 10.0$ kg/h, $\dot{m}_t = 1.45$ kg/h

(c) $\dot{m}_{cw} = 12.5$ kg/h, $\dot{m}_t = 1.85$ kg/h

(d) $\dot{m}_{cw} = 15.0$ kg/h, $\dot{m}_t = 2.2$ kg/h

Figure 5.18: *Shell side temperature profile comparison between the experimental data and the simulation result (first modification)*

As mentioned in section 4.2.1, the accuracies of the ten temperature sensors along the shell are low and no calibration is applied. In all conditions the shell side inlet temperature is around 50°C and the outlet temperature is around 130°C. From the results in Fig. 5.18 it can be observed that the temperature sensors have lower accuracies when the testing temperature is higher. Also it is obvious that the performances of the sensors No. 3 and 4 are not satisfactory. But they can give a qualitative idea about how the profile looks like. As shown in Fig. 5.18, results for four different specific operating conditions are compared. It can be observed that the 2-phase sub model can accurately predict the heat exchange process through the 2-phase region within the heat exchanger, because the slope of the temperature curves are almost identical to each other. The gap between the superheated sub model and the 2-phase sub model is caused by the sudden transition from saturated vapor to 2-phase condition with $q = 0.97$, and the gap between the 2-phase sub model

and the sub-cooled model is due to the sudden transition between 2-phase condition with $q = 0.1$ to saturated liquid. The results show a tendency that the higher the mass flow level, the more over-predicted is the output temperature. Further modifications are needed to improve the prediction of the performance at the transition area between the first and the second sub models.

Pressure Drop

Fig. 5.19 shows the pressure drop comparison between the experiments and the simulations on both shell and tube sides. The result on the shell side shows an error of 40%. Actually within the model only friction caused pressure drop is taken into account, others like distributor caused pressure drop is not simulated in the model. Therefore the pressure drop predicted by the model should be smaller. But it can be observed that the pressure drop predicted by the model is larger than that from the experiment. This is due to the over prediction of the friction factor on the shell side. The prediction of the pressure drop on the tube side is not in good order and with high errors. This is reasonable because the transition between the first and the second sub models is not well developed, thus the proportion of the sub-cooled condition is over predicted, as can be seen in Fig. 5.18. Therefore it is not possible to give a nice prediction for the pressure drop on the tube side. But the results indicate that the pressure drops on both sides are very small compared to the operating pressure levels, therefore they can barely influence the accuracy of the heat transfer calculations.

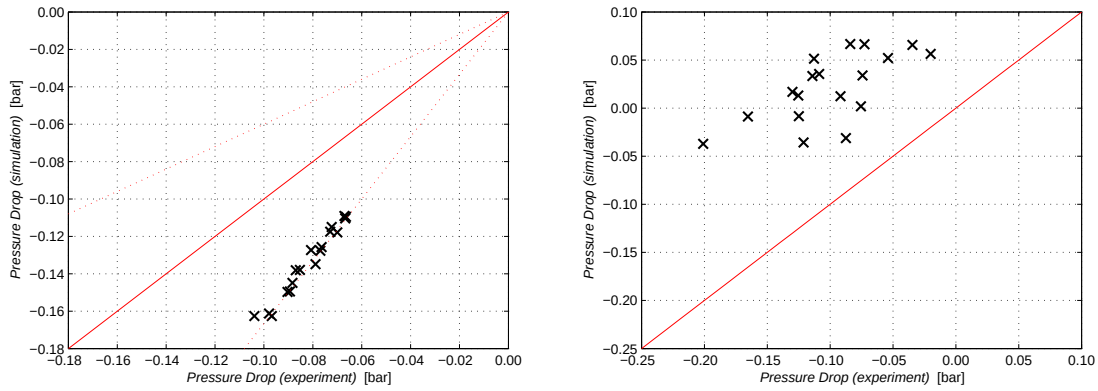

(a) shell side (error boundaries: ±40%) (b) tube side

Figure 5.19: *Pressure drop comparison between the experimental data and the simulation result (first modification)*

Heat Load

The heat load comparisons between the experimental data and the simulation results on both shell and tube sides are illustrated in Fig. 5.20. The result on the shell side shows that its relative error is within 10%. The shell side heat load predicted is always higher than that from the experiments. This is reasonable because the heat loss from the shell side to the environment is not simulated in the model, therefore the heat loads on both shell and tube sides are almost identical for the simulations, while for the experiments the heat load on the shell side is lower. Therefore to validate the heat load, it is better to compare the one on the tube side. As can be observed from the figure, the model predicts the heat load on the tube side with high accuracy, the relative error is lower than 3%. The results indicate that the model can perfectly predict the heat load of the heat exchanger.

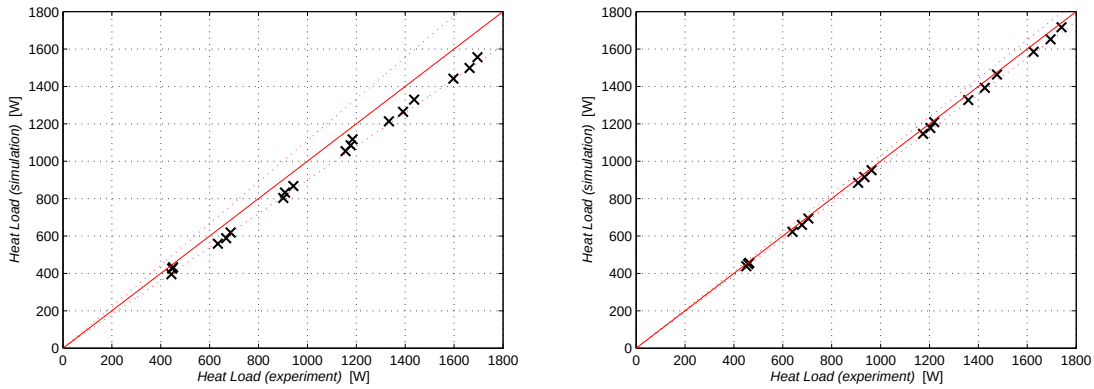

(a) shell side (error boundaries: ±10%) (b) tube side (error boundaries: ±3%)

Figure 5.20: *Heat load comparison between the experimental data and the simulation result (first modification)*

5.1.5. FURTHER STUDY OF THE TRANSITION BETWEEN THE FIRST AND THE SECOND SUB MODEL

Although the current model can perfectly predict the heat load of the mini-channel heat exchanger, the sudden transition between the first and the second sub models makes the model unable to predict the performance in between the region as can be seen in Fig. 5.18. In this section the model is further discussed and reasonable assumptions are applied to modify the simulation process.

As previously mentioned, the gap between the first and the second sub model in Fig. 5.18 is caused by the sudden transition from saturated vapor to 2-phase condition with $q = 0.97$. Since the 2-phase sub model cannot predict the performance in between the gap, the heat transfer and pressure drop along the gap is roughly estimated using the superheated sub model. It is assumed that the heat transfer is directly between the vapor and the cooling water through the tube wall without considering the liquid film when the quality is between 97% and unity.

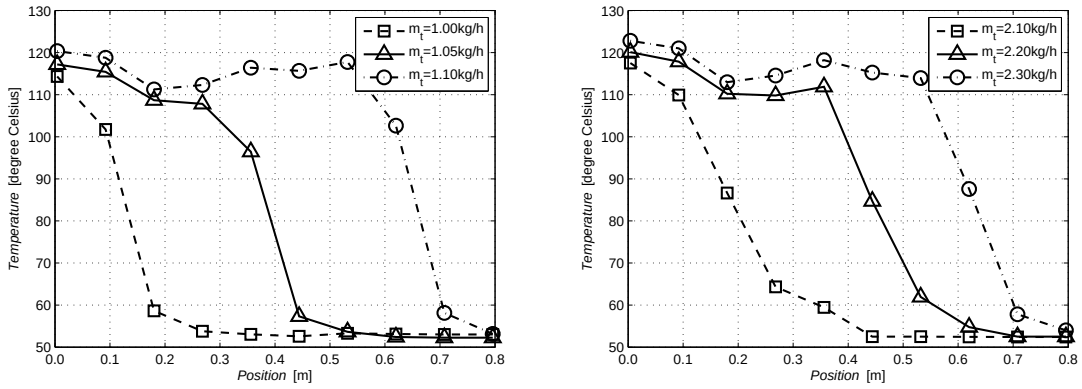

(a) $\dot{m}_{cw} = 7.5$ kg/h (b) $\dot{m}_{cw} = 15.0$ kg/h

Figure 5.21: *Shell side temperature profile (experimental data)*

Besides the gap, there is another issue within the superheated region. Fig. 5.21 shows the experimental results for the shell side temperature profile along the heat exchanger. It can be observed that when the shell side mass flow is fixed, tiny increase of the tube side mass flow will notably prolong the superheated region. The model should be tested with reasonable modification to study this

phenomenon.

The prolongation of the heat exchange area for the superheated phase is caused by weakened heat transfer. When mass flow on the shell side is fixed and the tube side mass flow is varied, to simplify the simulation, it can be assumed that the Nusselt number on the shell side is always constant (3.66 for constant temperature). While for the tube side it varies with different mass flows (3.66 multiplied by a factor). The Nusselt number on the tube side is determined by trial and error, and the experimental data for the shell side temperature profile are used to validate the model.

Fig. 5.22 shows some of the simulation results after modification of the Nusselt number on the tube side, and comparison with the experimental data. The simulations show a nice accordance with the experimental results since the trends of the curves are almost identical.

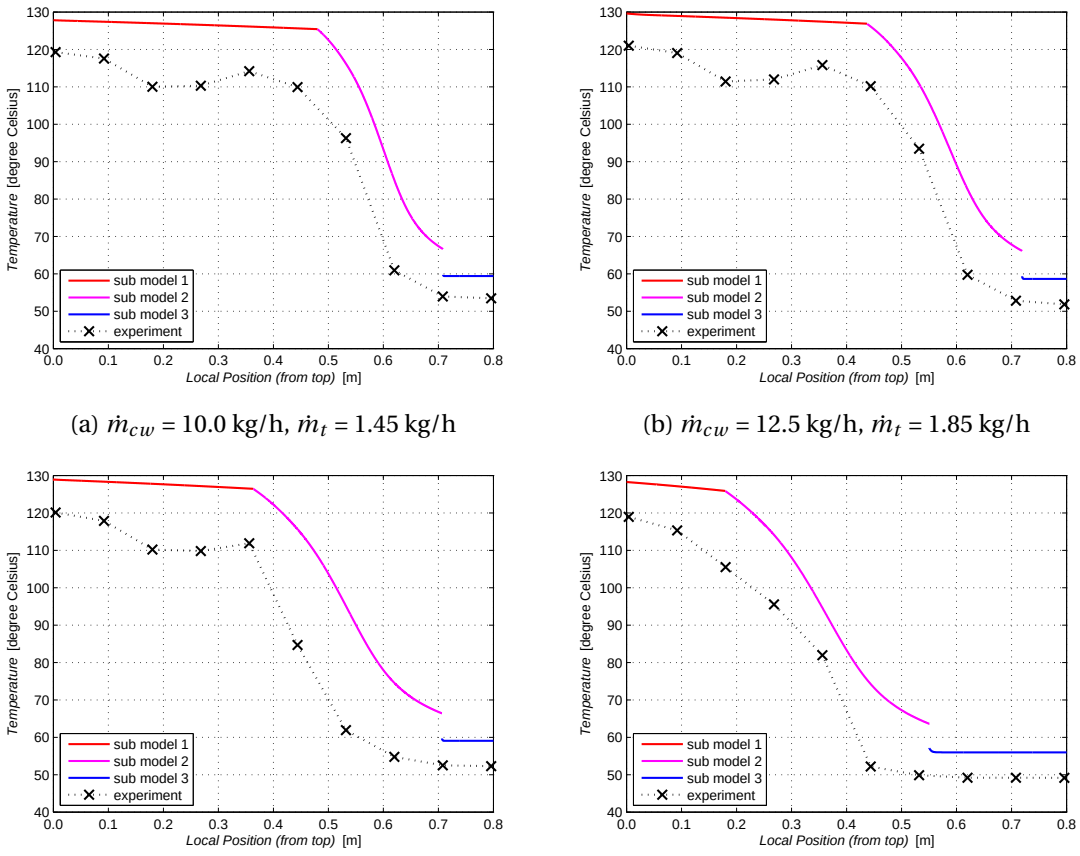

(a) $\dot{m}_{cw}$ = 10.0 kg/h, $\dot{m}_t$ = 1.45 kg/h

(b) $\dot{m}_{cw}$ = 12.5 kg/h, $\dot{m}_t$ = 1.85 kg/h

(c) $\dot{m}_{cw}$ = 15.0 kg/h, $\dot{m}_t$ = 2.2 kg/h

(d) $\dot{m}_{cw}$ = 17.5 kg/h, $\dot{m}_t$ = 2.6 kg/h

Figure 5.22: *Shell side temperature profile comparison between the experimental data and the simulation result (second modification)*

Pressure drop and heat load comparison between the experimental data and the simulation results after modification are illustrated in Fig. 5.23 and 5.24, respectively. The figures show that the shell side pressure drop prediction and the heat load predictions on both sides are similar to those results from the model after the first modification. The prediction for the pressure drop on the tube side becomes better and most of the errors are within 50%. Also it is reasonable that the pressure drop predicted by the simulation is lower than the experimental data, because only pressure drop caused by friction is taken into account in the model.

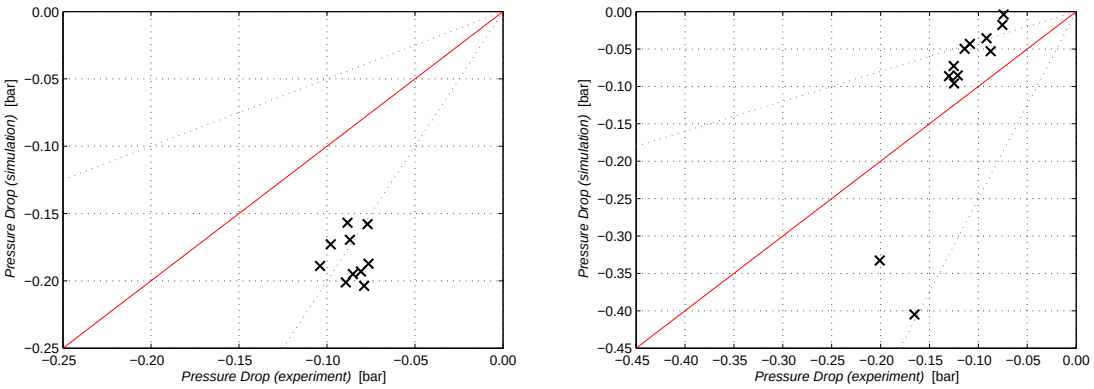

(a) shell side (error boundaries: ±40%) (b) tube side (error boundaries: ±50%)

Figure 5.23: *Pressure drop comparison between the experimental data and the simulation result (second modification)*

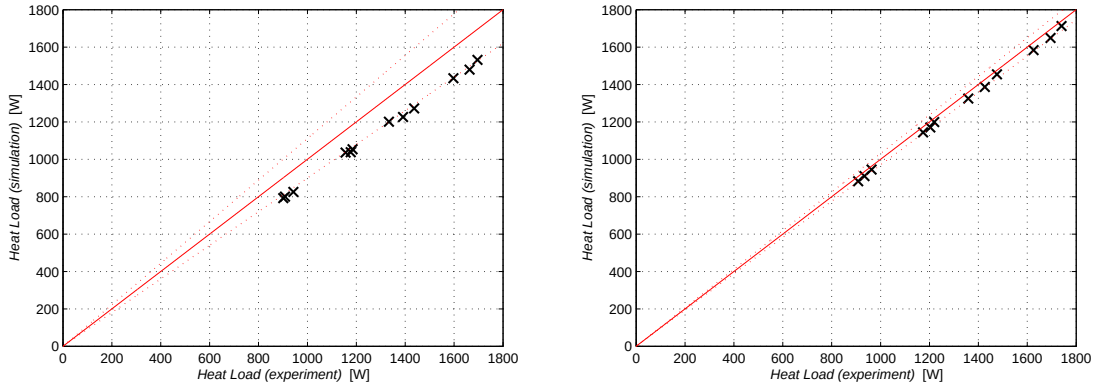

(a) shell side (error boundaries: ±10%) (b) tube side (error boundaries: ±3%)

Figure 5.24: *Heat load comparison between the experimental data and the simulation result (second modification)*

The tube side Nusselt numbers in the superheated region during the simulations are determined by trial and error. It would be good to have an idea about what is the key factor that influences the heat transfer. Nefs [9] in his study concluded that the hydrodynamic instabilities caused temperature and pressure fluctuations and would lead to a poor heat transfer performance. The pressure fluctuations are also observed in the current experiments as shown in Fig. 4.4. The pressure on the shell side is quite stable, while on the tube side it is always fluctuating with certain frequency and amplitude. Therefore the frequency and amplitude data of the tube side pressure fluctuation are collected and they are compared to the Nusselt number factor. The results are listed in table 5.2. The Nusselt number factor is defined as:

$$F_{\mathrm{Nu}} = \frac{\mathrm{Nu}_t}{3.66} \tag{5.10}$$

where 3.66 is the Nusselt number for tubular laminar flow when the wall temperature is constant.

As can be derived from the table: when the shell side mass flow is fixed, the Nusselt number on the tube side for the superheated sub model decreases with the increase of the tube side mass flow. This is caused by stronger tube side pressure fluctuation indicated by its higher amplitude and frequency; for all the optimum operating conditions, the higher the mass flows, the higher the corresponding tube side Nusselt number. However the tube side pressure fluctuation does not show clear regularities.

Table 5.2: *Effect of the pressure fluctuations*

$\dot{m}_{cw}$ [kg/h]	$\dot{m}_t$ [kg/h]	Nu	F_{Nu}	amp. [bar]	freq.
17.5	2.70	1.85	0.51	0.17	0.056
	2.60 (opt.)	3.77	1.03	0.11	0.032
	2.50	7.32	2.00	0.06	0.028
15.0	2.30	1.57	0.43	0.16	0.043
	2.20 (opt.)	1.94	0.53	0.08	0.036
	2.10	5.49	1.50	0.07	0.010
12.5	1.90	1.31	0.36	0.23	0.039
	1.85 (opt.)	1.61	0.44	0.13	0.032
	1.80	2.53	0.69	0.07	0.023
10.0	1.50	1.32	0.36	0.22	0.037
	1.45 (opt.)	1.35	0.37	0.27	0.022
	1.40	2.23	0.61	0.12	0.020

The tube side Nusselt numbers for superheated conditions for different operating conditions can be qualitatively explained using the experimental data, however it is difficult to quantitatively predict it by applying the amplitude and frequency of the pressure fluctuations. This is due to the fact that the amplitude and frequency are roughly estimated since sometimes the experimental results does not show very good regularity or it is not stable enough. Therefore the accuracies of the amplitude and the frequency are not good enough. The second reason is that the tube side Nusselt numbers shown in table 5.2 are determined by comparison with the experimental result for the temperature profile along the shell, which is of low accuracy. The third reason is that the sample size of the experiments is small, there are not enough data to get quantitatively analyzed.

5.2. VALIDATION FOR CO_2–NH_3–H_2O THERMODYNAMIC MODELS

Experimental data from the CO_2–NH_3–H_2O/water experiment can be applied to validate the thermodynamic models for the CO_2–NH_3–H_2O mixture mentioned in section 2.2. Currently two parameters of the mixture can be roughly validated: the enthalpy and the density.

The enthalpy can be indirectly validated by comparing the heat loads on both sides of the heat exchanger. The shell side heat load can be calculated by:

$$\dot{Q}_{cw} = \dot{m}_{cw} \cdot (h_{cw,out} - h_{cw,in}) \tag{5.11}$$

The value of the cooling water mass flow is directly attained from the experimental data; the enthalpy of the cooling water is calculated using RefProp. It is determined by the local temperature and pressure, which can be obtained from the experimental data. Similarly, the tube side heat load can be determined by:

$$\dot{Q}_t = \dot{m}_t \cdot (h_{t,in} - h_{t,out}) \tag{5.12}$$

The enthalpy of the mixture can be calculated using the thermodynamic models from Darde [11], Que and Chen [14], or the new fit from Gudjonsdottir and Infante Ferreira [7]. These models are available in the commercial software Aspen Plus. The enthalpy is determined by the local temperature, pressure and the composition of the mixture. The temperature and pressure can be obtained from the experimental data, and the composition follows the data listed in table 4.6. The result of the heat load comparison between these three models are depicted in Fig. 5.25. The heat load on the tube side should be large since there is heat loss from the shell side to the environment. The amount

of the heat loss is difficult to determine, here refer to the ammonia–water/water experiment results (Fig. 4.15), where it is concluded that the tube side heat load is higher and that the relative error between the two heat flows is within 5%. The result in Fig. 5.25 shows that the tube side heat load is higher and the error is around 10% (red dashed lines are ±5%, red dotted lines are ±10%), the result is satisfactory. The enthalpy difference values predicted by the three models are almost identical.

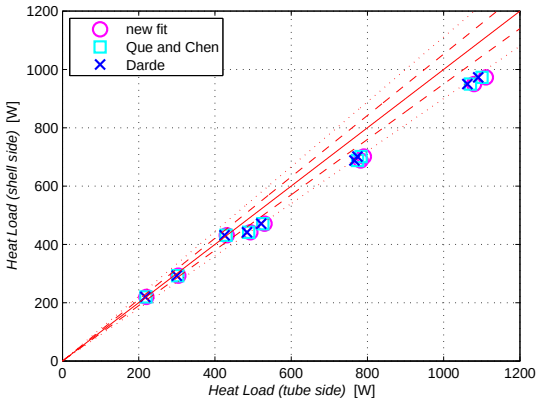

Figure 5.25: *Heat load comparison between different models*

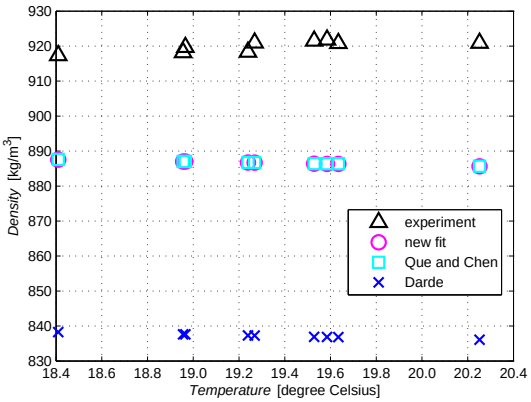

Figure 5.26: *Density comparison between different models*

The flow meter installed after the pump can give back its local temperature and density values. They can be applied to validate the density calculated from the thermodynamic models. Similar to the determination of enthalpy stated above, the density can also be calculated in Aspen Plus with the 3 models by providing local temperature, pressure and composition. The results are illustrated in Fig. 5.26. It can be observed that the prediction from Darde's model is much lower than the experimental data, while the prediction by the models from Gudjonsdottir and Infante Ferreira, Que and Chen are almost identical and they are closer to the experimental data. The gap between the experimental data and the model prediction can be caused by various reasons, besides the inaccuracy of the thermodynamic model, the accuracy of the mixture composition is hard to determine. The composition data mentioned in table 4.6 is tested using scales, and it is quite difficult to accurately control the mass going into the system. Therefore it is not possible to quantitatively estimate the accuracy of the thermodynamic models' predictions, but at least it can be concluded that the model from Darde predicts density with lower accuracy. One other aspect can be obtained from the result is that the models predicted that the density decreases with the increasing temperature, while the experimental data do not show such trend. This is because the pressure also influences the density. The results from the experiments indicate that the pressure influence on the density is notable, while the result from the models show that the influence of the pressure is negligible.

6

CONCLUSIONS AND RECOMMENDATIONS

6.1. CONCLUSIONS

One main objectives of this study is to develop a theoretical model to predict the performance of the ammonia–water absorption process within a certain multi-tube mini-channel heat exchanger, and to perform experiments to validate the model. The results obtained from the theoretical model and the corresponding experiments lead to the following conclusions:

- Annular flow pattern is dominant on the tube side through the absorption process. Falling film theory is applied in the model. It is assumed that a smooth film is formed along the inner tube wall of the heat exchanger, and its local thickness can be calculated based on the analytical solution of the Nusselt theory. Therefore the flow pattern on the tube side is assumed to be annular flow. The simulation and experimental results indicate that annular flow pattern dominates along this absorption process. However when the vapor quality is low, the film thickness prediction is not accurate and the heat/mass transfer intensity becomes weak. Therefore it can be concluded that when the vapor quality is low, the flow pattern may transit from annular flow to other flow patterns thus to enhance the transfer phenomena.

- The 2-phase model can predict the absorption process well. The two-phase model gives local values along the heat exchanger for various thermodynamic and transport parameters. The results show that during the absorption process, most of the water vapor is first quickly condensed into liquid phase, while the ammonia vapor is comparatively slowly absorbed into the solution with a delay. Between the vapor and the liquid phase of the mixture, heat transfer due to condensation (mass transfer from vapor to liquid) dominates. Explicit heat transfer caused by temperature driving force can be neglected.

- The completed model after first modification can perfectly predict the heat load of the heat exchanger and the absorption process in the 2-phase region. To make the experimental data available for validation, the theoretical model is extended to include two sub models to predict the performance of the heat exchanger when the mixture is under superheated or sub-cooled conditions. The extended model shows perfect agreement with the experimental results for the temperature profile in the 2-phase region and for the heat load. While the pressure difference on the shell side is over predicted, this can be caused by overestimation of the friction factor on the shell side. The pressure difference on the tube side cannot be reasonably predicted due to the fact that the gaps between the superheated and 2-phase, and between the 2-phase and sub-cooled regions are not well defined.

- The heat transfer performance for the superheated region of the ammonia–water mixture at the inlet of the tube is further studied. Result shows that instead of being a constant (3.66), the tube side Nusselt number is sensitive to the tube side mass flow. This can be related to the hydrodynamic instabilities on the tube side. By investigating the relation between the tube side Nusselt number and the corresponding pressure fluctuation, it can be concluded that they have some kind of inner relations with each other. But due to lack of abundant experimental data and the high uncertainty of the current data, the relation is remained to be discovered.

Another main objective of the current study is to experimentally compare the performances of the absorption process between using ammonia–water and CO_2–NH_3–H_2O mixture as a working fluid. The experimental results lead to the following conclusions:

- Adding CO_2 to the ammonia–water mixture dramatically increases the operating pressure level on the tube side. Small amount of CO_2 (2.1% percent by mass) is directly added to the system after the ammonia–water/water experiments. The results show that when operated at the same temperature level, this small amount of CO_2 added causes huge increase for the tube side pressure. This high pressure leads to a low vapor quality at the tube inlet and a higher tube side mass flow, which indicates a lower COP for the heat pump cycle.

- Adding CO_2 directly will lead to higher (though limited) heat load on the shell side on sacrifice of a better temperature distribution. When operated in optimum condition, higher outlet temperature for the cooling water can be obtained for the CO_2–NH_3–H_2O/water experiment than for the ammonia–water/water experiments. But the logarithm mean temperature difference is higher since the temperature distributions become worse.

- Attempts have been tried to lower down the operating pressure level in order to make the experiments more comparable. It shows prospective results when the pressure level is lower. However the operating condition becomes unstable after the third time draining. Experimental results with the opposite flow direction indicate that the instability might be caused by the configuration of the heat exchanger. Upward flow on the absorption side is more stable, while the heat flow on the shell side becomes worse.

- The operating status for the CO_2–NH_3–H_2O/water experiment is less stable than the ammonia–water/water experiment. The pump works with difficulty to perform constant mass flow, especially for higher mass flows. This indicates that the CO_2–NH_3–H_2O solution is not very stable, and it is very possible to have CO_2 desorbed at the pump even at very low temperatures and pressures. Therefore compared to ammonia–water, the CO_2–NH_3–H_2O mixture is much less stable and it might be a problem in practical systems.

The last main objective is to validate the CO_2–NH_3–H_2O thermodynamic models with the obtained experimental data. The conclusions are as follows:

- The enthalpy is indirectly validated by the heat load calculated based on the experimental data. The results show acceptable agreement with all three different thermodynamic models.

- The density is directly validated from the experimental data. The result indicates that the models from Gudjonsdottir and Infante Ferreira, Que and Chen predict the density with better accuracy than the model from Darde.

6.2. RECOMMENDATIONS

According to the results and conclusions from the current work, a number of recommendations can be derived for further study:

- Other flow patterns should be modeled to predict the performance of the 2-phase flow when the vapor quality is low. The current study shows that annular flow is dominant but it fails at lower vapor qualities. Other flow patterns such as plug flow, slug flow, and bubbly flow may occur for the 2-phase flow before it is fully condensed. These flow patterns and their transition conditions should be further studied and simulated.
- A better model to predict the pressure drop on both sides is needed. Causes other than friction should be taken into account. Computational fluid dynamic methods may be applied to simulate the flow field within the mini-channel.
- Experiments with visual observations should be developed to better understand the flow patterns within the mini-size tubes. Currently there are no appropriate flow pattern maps which can predict the 2-phase downward flow for ammonia–water mixture in mini-size channels. Relative experimental studies should be done to develop a flow pattern map for practical use. Also visual results can be used to validate the film thickness predicted by the simulation.
- Experimental results covering more operating conditions are needed to further study the weakening of heat transfer caused by hydrodynamic instabilities and to further validate the thermodynamic models of the CO_2–NH_3–H_2O mixture.
- Pressure control facilities (e.g. compressors) should be installed in the system to fix the pressure level on the mixture side. These results between the CO_2–NH_3–H_2O/water experiment and ammonia–water/water experiments can be made comparable. If possible, a setup with a complete CRHP cycle should be established to better study the influence of adding CO_2 to the ammonia–water mixture on the performance of the CRHP cycle.

A

APPENDIX A

A.1. EXPERIMENTAL DATA FOR WATER/WATER EXPERIMENTS

Both shell and tube sides are filled in with water, the experimental data are listed below.

Table A.1: *Experimental data for water/water experiments*

#	Side	$\dot{m}$ [kg/h]	T_{in} [°C]	T_{out} [°C]	P_{in} [bar]	P_{out} [bar]	$\dot{Q}$ [W]
01	Shell	2.50	60.82	111.41	6.25	6.19	147.6
	Tube	10.00	111.61	96.76	8.42	8.43	174.0
02	Shell	5.00	64.32	111.56	6.49	6.42	275.7
	Tube	10.00	111.96	86.76	8.85	8.86	294.9
03	Shell	7.50	65.68	111.24	6.62	6.54	398.9
	Tube	10.00	111.94	76.91	9.24	9.25	409.4
04	Shell	9.99	65.30	110.43	6.97	6.89	526.7
	Tube	9.99	111.68	68.90	10.34	10.35	499.3
05	Shell	12.49	63.32	103.50	8.95	8.87	585.4
	Tube	9.99	110.91	64.79	13.99	14.00	537.8
06	Shell	14.99	61.68	97.50	9.12	9.03	625.9
	Tube	9.99	111.56	62.51	13.36	13.37	572.0
07	Shell	17.49	59.64	91.93	8.76	8.66	657.6
	Tube	9.99	111.55	60.24	12.35	12.36	598.3
08	Shell	19.99	57.50	86.96	6.51	6.40	685.6
	Tube	9.99	111.42	58.02	10.95	10.95	622.5

A.2. EXPERIMENTAL DATA FOR AMMONIA–WATER/WATER EXPERIMENTS

Ammonia–water mixture flows on the tube side, water flows on the shell side.

Table A.2: *Experimental data for ammonia–water/water experiments*

#	Side	$\dot{m}$ [kg/h]	T_{in} [°C]	T_{out} [°C]	P_{in} [bar]	P_{out} [bar]	$\dot{Q}$ [W]
01	Shell	5.00	50.88	126.78	4.15	4.09	443.5
	Tube	0.70	129.59	50.76	3.78	3.74	450.6
02	Shell	5.00	50.63	127.11	4.24	4.17	447.1
	Tube	0.71	132.00	50.69	3.82	3.75	458.4
03	Shell	5.00	50.87	127.88	4.30	4.24	450.1
	Tube	0.72	132.00	52.00	3.92	3.84	462.7
04	Shell	7.50	50.05	122.44	4.22	4.15	633.8
	Tube	0.99	131.32	50.11	3.73	3.71	639.4
05	Shell	7.50	49.72	125.91	4.73	4.66	667.5
	Tube	1.05	130.99	49.91	3.84	3.79	678.3
06	Shell	7.50	50.01	128.26	4.79	4.72	685.7
	Tube	1.09	134.02	55.02	4.06	3.95	704.6
07	Shell	9.99	50.11	127.24	4.86	4.78	901.0
	Tube	1.40	135.35	50.24	4.00	3.93	908.3
08	Shell	9.99	50.09	127.82	5.05	4.98	908.1
	Tube	1.44	131.91	51.63	4.10	3.99	934.2
09	Shell	9.99	49.73	130.37	5.35	5.27	942.5
	Tube	1.50	136.90	55.72	4.33	4.22	963.1
10	Shell	12.49	48.41	127.57	5.34	5.26	1155.9
	Tube	1.80	137.71	48.77	4.09	4.00	1174.0
11	Shell	12.49	49.02	129.62	5.39	5.30	1177.1
	Tube	1.84	137.84	49.87	4.31	4.19	1203.2
12	Shell	12.49	49.11	130.21	5.51	5.43	1184.5
	Tube	1.90	134.04	55.09	4.45	4.32	1219.1
13	Shell	14.99	49.64	125.76	5.21	5.13	1333.4
	Tube	2.10	131.26	49.82	4.16	4.09	1358.5
14	Shell	14.99	49.57	128.93	5.62	5.53	1390.8
	Tube	2.20	134.09	50.04	4.33	4.20	1426.2
15	Shell	14.99	49.57	131.51	5.86	5.77	1436.6
	Tube	2.30	137.99	56.80	4.64	4.47	1476.2
16	Shell	17.49	47.77	125.91	5.33	5.24	1596.9
	Tube	2.50	132.37	47.95	4.15	4.06	1625.8
17	Shell	17.49	46.91	128.28	5.57	5.47	1663.2
	Tube	2.60	133.95	47.26	4.35	4.23	1694.9
18	Shell	17.49	47.90	130.81	5.89	5.80	1695.4
	Tube	2.70	134.57	53.24	4.60	4.40	1740.3

A.3. EXPERIMENTAL DATA FOR CO_2–NH_3–H_2O/WATER EXPERIMENTS

CO_2–NH_3–H_2O mixture flows on the tube side, water flows on the shell side.

Table A.3: *Experimental data for CO_2–NH_3–H_2O/water experiments*

#	Side	$\dot{m}$ [kg/h]	T_{in} [°C]	T_{out} [°C]	P_{in} [bar]	P_{out} [bar]	$\dot{Q}$ [W]
01	Shell	5.00	50.59	88.37	2.91	2.84	219.81
	Tube	0.72	132.46	51.88	7.42	7.38	–
02	Shell	5.00	50.95	126.46	4.27	4.20	441.35
	Tube	2.00	131.81	58.91	8.88	8.83	–
03	Shell	5.00	50.82	131.31	4.39	4.32	470.77
	Tube	2.10	132.46	58.51	8.89	8.83	–
04	Shell	7.50	50.04	83.60	2.95	2.89	292.75
	Tube	1.06	130.73	52.93	7.50	7.45	–
05	Shell	7.50	50.33	128.79	4.96	4.89	687.62
	Tube	3.31	131.50	58.14	9.26	9.21	–
06	Shell	7.50	50.10	130.08	4.98	4.91	701.10
	Tube	3.37	131.36	58.43	9.30	9.23	–
07	Shell	9.99	50.54	87.61	3.31	3.23	431.25
	Tube	1.46	134.26	54.45	8.06	8.03	–
08	Shell	9.99	50.13	131.41	5.53	5.47	949.90
	Tube	4.20	134.51	53.76	9.48	9.53	–
09	Shell	9.99	50.21	133.41	5.64	5.56	972.81
	Tube	4.51	134.30	54.75	9.84	9.76	–
10	Shell	5.00	50.90	112.10	3.62	3.55	356.95
	Tube	1.50	132.36	55.60	8.58	8.54	–
11	Shell	5.00	51.00	117.86	3.83	3.76	390.23
	Tube	1.71	132.31	55.74	8.75	8.71	–
12	Shell	5.00	51.05	123.03	4.01	3.95	420.38
	Tube	1.91	132.25	57.21	8.87	8.82	–
13	Shell	5.00	50.93	129.66	4.35	4.28	460.27
	Tube	2.09	132.52	58.45	9.12	9.08	–
14	Shell	5.00	50.66	130.29	4.69	4.63	465.65
	Tube	2.30	132.69	63.49	9.20	9.15	–
15	Shell	5.00	50.97	130.41	4.91	4.85	464.42
	Tube	2.48	132.41	73.30	9.24	9.18	–
16	Shell	5.00	51.19	130.69	4.82	4.75	464.87
	Tube	2.70	132.49	80.28	9.33	9.27	–
17	Shell	5.00	51.17	92.09	3.11	3.05	238.16
	Tube	0.71	132.57	52.61	6.96	6.94	–
18	Shell	5.00	51.02	122.21	4.14	4.07	415.74
	Tube	1.50	132.91	56.09	7.65	7.62	–
19	Shell	5.00	51.13	129.50	4.47	4.41	458.22
	Tube	1.70	132.77	55.91	7.66	7.62	–
20	Shell	5.00	51.21	107.86	3.56	3.50	330.31
	Tube	0.71	132.83	53.24	5.72	5.67	–
21	Shell	5.00	51.06	131.92	4.95	4.88	472.93
	Tube	1.49	132.72	66.38	6.55	6.49	–

BIBLIOGRAPHY

[1] IEA, *Energy and climate change–world energy outlook special report* (2011).

[2] CBS, *Energy balance sheet* (2016).

[3] D. M. van de Bor, C. A. Infante Ferreira, and A. A. Kiss, *Low grade waste heat recovery using heat pumps and power cycles,* Energy **89**, 864 (2015).

[4] I. Dinçer and M. Kanoğlu, *Refrigeration systems and applications*, 2nd ed. (John Wiley & Sons, 2011).

[5] L. C. M. Itard, *Wet compression–resorption heat pump cycles: thermodynamic analysis and design*, Ph.D. thesis, Delft University of Technology (1998).

[6] J. J. Rijpkema, *Experimental validation of a new ammonia/water absorption model in a minichannel annulus*, Master's thesis, Delft University of Technology (2012).

[7] V. Gudjonsdottir and C. A. Infante Ferreira, *Comparison of models for calculation of the thermodynamic properties of NH_3-CO_2-H_2O mixture,* (2016).

[8] J. van Leeuwen, *Absorption and desorption of ammonia-water mixtures in mini-channel heat exchangers*, Master's thesis, Delft University of Technology (2011).

[9] C. W. M. Nefs, *Experimental validation of a mini-channel multi-tube ammonia-water absorption/desorption model*, Master's thesis, Delft University of Technology (2013).

[10] K. Thomsen and P. Rasmussen, *Modeling of vapor–liquid–solid equilibrium in gas–aqueous electrolyte systems,* Chemical Engineering Science **54**, 1787 (1999).

[11] V. Darde, K. Thomsen, W. J. M. van Well, D. Bonalumi, G. Valenti, and E. Macchi, *Comparison of two electrolyte models for the carbon capture with aqueous ammonia,* International Journal of Greenhouse Gas Control **8**, 61 (2012).

[12] V. Darde, W. J. M. van Well, E. H. Stenby, and K. Thomsen, *Modeling of carbon dioxide absorption by aqueous ammonia solutions using the extended uniquac model,* Industrial & Engineering Chemistry Research **49**, 12663 (2010).

[13] C. Chen, H. I. Britt, J. F. Boston, and L. B. Evans, *Local composition model for excess Gibbs energy of electrolyte systems. part I: single solvent, single completely dissociated electrolyte systems,* AIChE Journal **28**, 588 (1982).

[14] H. Que and C. Chen, *Thermodynamic modeling of the NH_3–CO_2–H_2O system with electrolyte nrtl model,* Industrial & Engineering Chemistry Research **50**, 11406 (2011).

[15] Z. Niu, Y. Guo, Q. Zeng, and W. Lin, *A novel process for capturing carbon dioxide using aqueous ammonia,* Fuel Processing Technology **108**, 154 (2013).

[16] I. P. Koronaki, L. Prentza, and V. Papaefthimiou, *Modeling of CO_2 capture via chemical absorption processes–an extensive literature review,* Renewable and Sustainable Energy Reviews **50**, 547 (2015).

[17] M. Caplow, *Kinetics of carbamate formation and breakdown,* Journal of the American Chemical Society **90**, 6795 (1968).

[18] P. V. Danckwerts, *The reaction of CO_2 with ethanolamines,* Chemical Engineering Science **34**, 443 (1979).

[19] P. D. Vaidya and E. Y. Kenig, *CO_2-alkanolamine reaction kinetics: a review of recent studies,* Chemical Engineering & Technology **30**, 1467 (2007).

[20] V. Darde, W. J. M. van Well, P. L. Fosboel, E. H. Stenby, and K. Thomsen, *Experimental measurement and modeling of the rate of absorption of carbon dioxide by aqueous ammonia,* International Journal of Greenhouse Gas Control **5**, 1149 (2011).

[21] J. E. Crooks and J. P. Donnellan, *Kinetics and mechanism of the reaction between carbon dioxide and amines in aqueous solution,* Journal of the Chemical Society, Perkin Transactions 2 , 331 (1989).

[22] E. F. da Silva and H. F. Svendsen, *Ab initio study of the reaction of carbamate formation from CO_2 and alkanolamines,* Industrial & Engineering Chemistry Research **43**, 3413 (2004).

[23] F. Qin, S. Wang, A. Hartono, H. F. Svendsen, and C. Chen, *Kinetics of CO_2 absorption in aqueous ammonia solution,* International Journal of Greenhouse Gas Control **4**, 729 (2010).

[24] P. W. J. Derks and G. F. Versteeg, *Kinetics of absorption of carbon dioxide in aqueous ammonia solutions,* Energy Procedia **1**, 1139 (2009).

[25] G. Puxty, R. Rowland, and M. Attalla, *Comparison of the rate of CO_2 absorption into aqueous ammonia and monoethanolamine,* Chemical Engineering Science **65**, 915 (2010).

[26] J. Liu, S. Wang, G. Qi, B. Zhao, and C. Chen, *Kinetics and mass transfer of carbon dioxide absorption into aqueous ammonia,* Energy Procedia **4**, 525 (2011).

[27] D. M. van de Bor, *Mini-channel heat exchangers for industrial distillation processes*, Ph.D. thesis, Delft University of Technology (2014).

[28] S. P. Aarts, *Entropy production minimisation of a compression-resorption heat pump*, Master's thesis, Delft University of Technology (2016).

[29] E. W. Lemmon, M. L. Huber, and M. O. McLinden, *Reference fluid thermodynamic and transport properties (REFPROP), version 9.0; NIST standard reference database 23,* (2010).

[30] R. Tillner-Roth and D. G. Friend, *A Helmholtz free energy formulation of the thermodynamic properties of the mixture {water+ ammonia}*, Journal of Physical and Chemical Reference Data **27**, 63 (1998).

[31] A. S. Rattner and S. Garimella, *Fast, stable computation of thermodynamic properties of ammonia-water mixtures,* International Journal of Refrigeration **62**, 39 (2016).

[32] *Thermophysical properties of ammonia-water mixtures for the industrial design of absorption refrigeration equipment* (M. Conde Engineering, 2006).

[33] J. Sieres and J. Fernández-Seara, *Modeling of simultaneous heat and mass transfer processes in ammonia–water absorption systems from general correlations,* Heat and Mass Transfer **44**, 113 (2007).

[34] J. D. Seader, E. J. Henley, and D. K. Roper, *Separation process principles*, 3rd ed. (JohnWiley & Sons, 2011).

[35] P. Stephan, S. Kabelac, M. Kind, H. Martin, D. Mewes, and K. Schaber, *VDI Heat Atlas*, 2nd ed. (Springer, Berlin, 2010).

[36] L. Friedel, *Improved friction pressure drop correlations for horizontal and vertical two-phase pipe flow,* in *European Two-Phase Flow Group Meeting, Paper E*, Vol. 2 (1979).

[37] R. W. Lockhart and R. C. Martinelli, *Proposed correlation of data for isothermal two-phase, two-component flow in pipes,* Chem. Eng. Prog **45**, 39 (1949).

[38] R. Grönnerud, *Investigation of liquid hold-up, flow-resistance and heat transfer in circulation type evaporators, part IV: two-phase flow resistance in boiling refrigerants,* Bull. from the Inst. of Refrigeration, Annex .

[39] H. Müller-Steinhagen and K. Heck, *A simple friction pressure drop correlation for two-phase flow in pipes,* Chemical Engineering and Processing: Process Intensification **20**, 297 (1986).

[40] M. B. O. Didi, N. Kattan, and J. R. Thome, *Prediction of two-phase pressure gradients of refrigerants in horizontal tubes,* International Journal of Refrigeration **25**, 935 (2002).

[41] S. P. Mahulikar and H. Herwig, *Fluid friction in incompressible laminar convection: Reynolds' analogy revisited for variable fluid properties,* The European Physical Journal B **62**, 77 (2008).

[42] J. M. Smith, H. C. van Ness, and M. M. Abbott, *Introduction to chemical engineering thermodynamics*, 7th ed. (McGraw-Hill, 2005).

[43] J. P. Holman, *Heat transfer*, 10th ed. (McGraw-Hill, 2010).

[44] J. Taylor, *Introduction to error analysis, the study of uncertainties in physical measurements*, 2nd ed. (University Science Books, 1997).

[45] M. M. Mahmoud and T. G. Karayiannis, *Flow pattern transition models and correlations for flow boiling in mini-tubes,* Experimental Thermal and Fluid Science **70**, 270 (2016).